Dissertation zur Erlangung des Doktorgrades
der Fakultät für Chemie und Pharmazie
der Ludwig-Maximilians-Universität München

RAMAN MEASUREMENTS ON PLASMON-PHONON COUPLED SYSTEMS

Dynamical back-action between a localized plasmon-polariton and phonons in carbon materials and plasmon-phonon coupling in beryllium doped gallium arsenide nanowires

Tobia Mancabelli

aus

Zevio (Italien)

2016

Erklärung

Diese Dissertation wurde im Sinne von §7 der Promotionsordnung vom 28. November 2011 vom Herrn Prof. Dr. Achim Hartschuh betreut.

Eidesstattliche Versicherung

Diese Dissertation wurde eigenständig und ohne unerlaubte Hilfe erarbeitet.

München, 06.10.2016

Tobia Mancabelli

Dissertation eingereicht am 06. Oktober 2016

1. Gutachter: **Prof. Dr. Achim Hartschuh**

2. Gutachterin: **Prof. Dr. Regina de Vivie-Riedle**

Mündliche Prüfung am 17. November 2016

ABSTRACT

In this thesis, Raman spectroscopy is used to characterize the interaction between a plasmon and the lattice vibration of a solid state material. Two systems have been analyzed: the first is composed of a metallic nanostrucure and a carbon material (carbon nanotubes and graphene), the second consists of beryllium-doped gallium arsenide nanowires. In the first system, additionally to the electromagnetic enhancement, a cooperative process (*dynamical back-action*) between the localized surface plasmon-polariton and the lattice vibration can occur. This process leads to a non-linear response of the Raman signal in dependence on the laser power. In this work the occurrence of this non-linearity is experimentally observed and compared with the theoretical prediction. In the second system, the charge-carriers provided by the dopant act as a plasma, interacting with the electric field related to the longitudinal phonon mode of the crystal lattice. This interaction causes a change in the position and width of the Raman peak, which can consequently been used to extrapolate the change carriers concentration and mobility. The appearance of surface phonons, typical of nanostructures, is also observed and discussed.

Contents

INTRODUCTION

Spontaneous Raman scattering was first experimentally observed in 1928 [1]. Since then, Raman spectroscopy has progressively developed and consists nowadays of a large variety of techniques [2, 3, 4, 5, 6]. The main and most interesting characteristic of Raman scattering is that it provides a so called "molecular fingerprint": the difference between the incident and scattered light frequencies corresponds to the frequency of a vibrational mode characteristic of the specific material under observation. Differently from fluorescence, only one vibronic level is involved in the scattering (at least for first order Raman scattering, which is commonly obseved). The spectral peak related to Raman scattering has consequently a lorentzian lineshape, with a width of typically few cm^{-1}. In the case of composite materials for instance, consisting of several Raman scatterers, the spectrum of each individual component can often be distinguished because the Raman lines are sufficiently narrow not to overlap. Also in the presence of a broad background, the Raman peaks are in general easily recognizable on top of it, having a different and characteristic lineshape with respect to the background itself. Besides the spectral characterization, the Raman scattering can be sensitive to changes in energy and damping of the vibrational mode, being strictly related to the vibronic levels of the scatterer.

In this thesis, the Raman scattering is used to characterize the change in the vibrational properties of the material under observation, related either to the environmental conditions or to some other properties of the material itself. In particular, the interaction between a density of charge and the lattice vibration is investigated. The first system experimentally analyzed and discussed, is formed by a metallic nanostructure (in the specific case, gold nanorods and a gold nanotip) in close proximity to a Raman emitter (in the specific case carbon nanotubes and graphene). Such metallic nanostructures are able to generate a very strong local electromagnetic field, related to the electron density oscillation on the surface of the nanostrucure itself. The collective electron oscillation is called *"surface plasmon-polariton"* [47]. In the case of quasi zero-dimensional nanostructures, this collective oscillation is called *"localized surface plasmon-polariton"*. The strong local electromagnetic field can lead to a high enhancement of the Raman scattering. This phenomenon has been widely explored and exploited in the last decades in the framework of Surface Enhanced Raman Spectroscopy (SERS) and Tip Enhanced Raman Spectroscopy (TERS) [22, 23]. Recently another enhancement mechanism, named *dynamical back-action* has been proposed [44, 45], based on an optomechanical coupling between the surface plasmon-polariton and the Raman emitter. In the presence of this coupling, the total energy of the system is not given by the sum of the energies of the two individual systems only, but an additional term due to the coupling appears. Within a quantum-electrodynamic description, the *dynamical back-action* can formally be taken into account, including an interaction term in the Hamiltonian. The key signature of this optomechanical

coupling is a non-linear dependence of the Raman intensity on the incident laser power. Although a non-linear Raman response has been observed for a porphyrin molecule at the nanogap between a silver nanotip and a silver film [30], no comparison between the theoretical prediction and the experimental observation of this non-linear response is given in literature. It is also an open question, how this optomechanical coupling can contribute to the well known SERS/TERS signal enhancement [33]. In this first system, the vibrational properties of the Raman scatterer are changed by the environment, because of the interaction between a localized surface plasmon-polariton and the vibrational mode of the scatterer itself.

The second system under observation in this thesis are beryllium-doped gallium arsenide nanowires. Here, the typical width and position of the Raman peak change because of the interaction between the local electric field related to the lattice vibration and the charge carriers provided by the doping. Based on this change, the charge carrier concentration and mobility can be extracted from the Raman peak. Also, the appearance of a surface phonon mode, that is related to the surface morphology of the nanowires, is observed, in addition to the typical bulk modes. In this second system, the vibrational properties are changed by the density of charges given by the dopant inside the material itself.

This thesis is organized as follows: in the first part Raman scattering in solids is introduced, in order to explain the basic features of the Raman spectrum of the materials analyzed within this work (graphene, carbon nanotubes and gallium arsenide). In the second part, the experimental techniques and the utilized setups are presented. The third part is focused on plasmon enhanced spectrocopy and *dynamical back-action*, in relation to the experiments on carbon nanotubes and graphene. The basic concept of plasmonic enhanced spectroscopy are here introduced. For completeness, a classical formulation of stimulated Raman scattering is given and adapted in order to include the presence of the electromagnetic field related to the plasmon-polariton. Then the quantum-electrodynamic description of the coupled system formed by Raman emitter and plasmon-polariton is presented, where both a solution in the classical limit and a pure quantum solution are given. In the last chapter of the third part the experiment is described and the relative results are presented and discussed. The fourth part is focused on doped gallium arsenide nanowires. The specific features of a typical Raman spectrum of these nanowires are first introduced from a theoretical point of view. The results are then presented and interpreted according to the theoretical description given before.

Part I

Introduction to Raman Scattering in Solids

Chapter 1

Raman Scattering in Solids

In a spontaneous Raman scattering event, one incident electric field oscillating at a given frequency, illuminates a sample. With a certain probability, the incident field can be inelasticly scattered because of a polarizability change of the sample itself. This change of the polarizability is related to a vibrational mode. In a "Stokes" process a vibrational mode is excited. Consequently, the frequency of the scattered field decreases with respect to the frequency of the incident one. In an "Anti-Stokes" process a vibrational mode relaxes, and the frequency of the scattered field increases. In solids, the vibrational modes are described as phonons: a phonon is a quantum of lattice vibration. In general, different vibrational modes can exist in a solid depending on the crystal symmetry. In a phonon creation or annihilation process both energy and linear momentum must be conserved. In a Raman scattering experiment the excitation wavelength is usually in the visible or near infrared region. The wavevector is then in the order of 10^7 m^{-1}. Following from the lattice constant in solids, at the edge of the Brillouin Zone (BZ) the phonon wavevector is in the order of 10^9 m^{-1}. For this reason, in a Raman process driven by visible or infrared light, only phonons in the center of the BZ can be excited, where the phonon wavevector goes to zero (in some exceptional cases, large wavevector scattering can be given in the case the linear momentum is not conserved). In general, some phonon modes have zero frequency for zero wavevector and cannot therefore be excited if visible light is used (*acoustic phonons*). Other phonon modes have a finite frequency for zero wavevector and can therefore be observed in a Raman process driven by visible light (*optical phonons*). Throughout this thesis, it will be dealt with optical phonons.

The Raman Scattering in solids is described as a three-steps process [7, 8, 9]. The first step consists of an electron-photon interaction in which the electron goes from an initial state to a second electronic state α, usually from the valence to the conduction band. In the second step, the electron looses (or gains) energy creating (or absorbing) a phonon and reaches so the electronic state β from the state α. In the third step, the electron relaxes and a photon is emitted. The transitions involved in this process need to be summed over all the electronic states within the conduction and valence band. The transition matrix element of the overall process is the product

between the transition matrix elements of the single processes [10]:

$$W = \sum_{\alpha,\beta} \frac{2\pi}{\hbar} \frac{\left\langle \alpha \left| \hat{H}^{electron}_{radiation} \right| \psi_i \right\rangle}{\left[\hbar\omega_L - (E_\alpha - E_i) - i\gamma_\alpha\right]} \frac{\left\langle \beta \left| \hat{H}^{electron}_{lattice} \right| \alpha \right\rangle}{\left[\hbar\omega_m - (E_\beta - E_\alpha) - i\gamma_m\right]} \frac{\left\langle \psi_f \left| \hat{H}^{electron}_{radiation} \right| \beta \right\rangle}{\left[\hbar\omega_S - (E_\beta - E_f) - i\gamma_\beta\right]} \tag{1.1}$$

In eq. (1.1) ω_L, ω_S and ω_m are the laser, Stokes (the Anti-Stokes process can be analogously considered) and phonon frequency respectively; $\hat{H}^{electron}_{radiation}$ and $\hat{H}^{electron}_{lattice}$ are the electron-photon and the electron-phonon interaction Hamiltonians respectively. E_i is the energy of the initial state, $E_\alpha = E_i + \hbar\omega_L$, $E_\beta = E_\alpha + \hbar\omega_m$ and $E_f = E_\beta - \hbar\omega_S$. In the case of a double process as it is for the graphene 2D band, another term containing the electron-phonon scattering needs to be included in eq. (1.1) [11], as it is further discussed in the section about the phonon modes in graphene. The intensity of the Raman peak is proportional to the square of the transition matrix elements, $I \sim |W|^2$ [12, 13] .

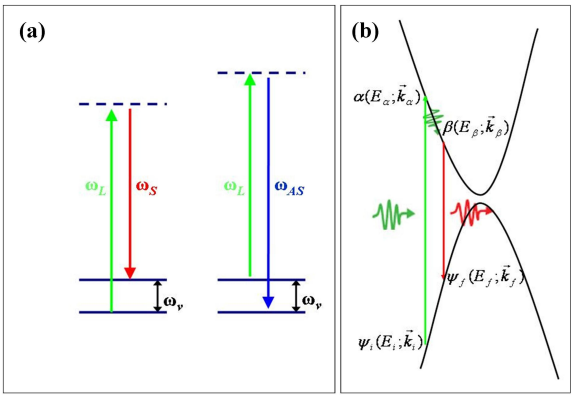

Figure 1.1: (a) general scheme for Stokes (left) and Anti-Stokes (right) scattering mechanisms. The laser frequency is labeled in green. The scattered light corresponding to the Stokes and Anti-Stokes process are labeled in red and blue respectively. (b) Raman scattering in the conduction and valence band of a solid, refer to eq. (1.1). The green and red arrows represent the incoming and outgoing light respectively.

In order to consider the symmetry of the molecular vibration the Raman cross section can also be expressed though the Raman tensor. To do so the polarization of the medium can be considered as the sum of the polarization of the units cells, $\vec{P} = N\vec{p}$. The polarization can be expressed though the polarizability (α) as:

$$\vec{p} = \bar{\bar{\alpha}}\vec{E} \tag{1.2}$$

$\vec{E}$ is the local electric field. Being both $\vec{p}$ and $\vec{E}$ vectorial quantities, $\bar{\bar{\alpha}}$ must be a second rank tensor. In presence of a lattice vibration, every element of the tensor $\bar{\bar{\alpha}}$ can be expanded as a function of the vibrational coordinate $\vec{x_v}$, as:

$$\alpha_i = \alpha_i(0) + \frac{\partial \alpha_i}{\partial \vec{x_v}} \vec{x_v} \tag{1.3}$$

The first terms in eq. (1.3) does not contribute to the Raman scattering, because such a process requires a change in the polarizability. The second ones are use to build up the *Raman tensor* $\bar{\bar{R}}$,

where every element of the tensor is given by:

$$R_i = \frac{\partial \alpha_i}{\partial \vec{x_v}} \frac{\vec{x_v}}{|\vec{x_v}|} \tag{1.4}$$

The scattered intensity is then proportional to:

$$I_S \sim \left| \hat{e_S} \bar{\bar{R}} \hat{e_L} \right|^2 \tag{1.5}$$

where $\hat{e_L}$ and $\hat{e_S}$ are the unit vectors giving the polarization of the laser and scattered light respectively. The Raman tensor reflects the symmetry of the phonon vibration. Thank to this, the selection rules can be taken into consideration. Indeed according to eq. (1.5), the Raman scattering intensity depends on the polarization of the incident and scattered fields [14, 15]. Once it has been established which Raman modes are active, eq. (1.2) is usually expressed in the scalar form. The scalar formulation is used in the following of this thesis.

In the next sections, the discussion is focused on graphene and gallium arsenide, being these two the materials analysed in the experimental work.

Phonon Modes in Gallium Arsenide

The phonon band structure of gallium arsenide (GaAs) is presented in Figure 1.2. The phonon

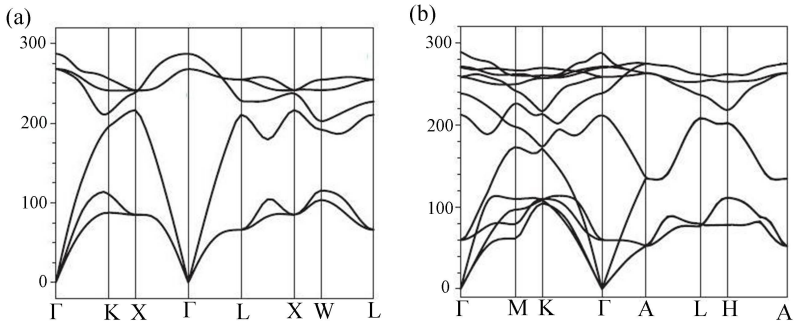

Figure 1.2: (a) Phonon dispersion for GaAs in the Zinc Blende phase: there are two optically active phonon modes at the Γ-point at the center of the Brillouin Zone corresponding to the TO and LO mode, their energy is $266\,\mathrm{cm}^{-1}$ and $291\,\mathrm{cm}^{-1}$ respectively. (b) phonon dispersion for GaAs in the Wurzite phase; in this case additional optically active mode are present. Adapted from [16].

dispersion is different for different crystal structures, namely Zinc Blende (ZB) and Wurzite (WZ) in the case of GaAs. As already explained, acoustic and optical phonons are present. Concerning the ZB structure, two optical phonon modes are present: transversal (TO) and longitudinal (LO). They have different energies in the center of the BZ and can therefore be observed as two separated peaks in a Raman spectrum. The phonon dispersion is more complicated for the WZ structure and additional modes can be observed in a Raman spectrum [15, 16]. In the TO vibrational mode

the atomic planes move perpendicularly to the propagation direction, while in the LO vibrational mode the atomic planes move parallel to the direction of propagation. Consequently, the center of mass of the unit cell is conserved within a TO mode vibration, while it is not within the LO one. GaAs is a polar crystal, meaning that the lattice sites are not occupied by neutral atoms but by ions. The non-conservation of the center of mass within the unit cell, leads to the presence of a non-zero local field, associated to the LO phonon. In Chapter 8 this aspect is described in more detail, in terms of the field curl and divergence. As will be discussed in Chapter 8 and 9, in the case of doped polar semiconductors, the interaction between this local field and the charge carriers changes the characteristics of the Raman peak.

Phonon Modes in Graphene

The phonon band structure of Graphene is presented in Figure 1.3. In this case, TO and LO phonons have the same energy at the centre of the BZ (Γ-point). Both of them appear then in the same Raman peak. For graphene the peak formed by the sum of TO and LO modes is named G band. A particular property of graphene is that additional Raman active modes are present, deriving

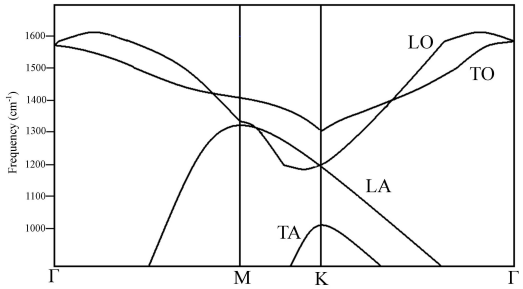

Figure 1.3: Graphene Phonon Dispersion. Adapted from [17, 18].

from scattering away from the center of the BZ. This kind of scattering is generally speaking defect assisted and the related Raman bands are named D, D', D + D', and the 2D. The appearance of the D, D' and D + D' bands depends on the defects concentration [18]. Although it is an overtone of the D band, the 2D band does not require the presence of defects and appears also in defect-free graphene. In the following the discussion is focused on the 2D band, being this relevant to the experimental results presented in the next chapters of this thesis. The 2D band stems from a double resonant process, in which two phonons are created with opposite momentum, so that the overall linear momentum in conserved. In the phonon band structure, the accessible energies are not in this case restricted to the Γ-point but also large momentum energy states are allowed. In particular, the typical energy of the 2D band ($\sim 2700\,\mathrm{cm}^{-1}$) is twice the energy of the phonon at the K-point of the BZ. In the prospective of the electronic band structure, the electron is scattered from a state the conduction band, reached after the absorption of a photon, to another state of the Dirac cone around the K-point. In this first scattering event, the first phonon is created. The electron is then scattered back, with the creation of the second phonon having opposite linear momentum to the first one, and allowing so for the overall linear momentum conservation (Figure 1.4). Although a two-phonon process typically has lower probability, the 2D band scattering in graphene becomes very strong because of multiple resonances. Although it consist of TO phonons [11], the symmetry

of the 2D band is different than that of the G band. This is because, given the large momentum involved in the 2D process, the vibration happens at the K-point of the BZ and not at the Γ-point. The resulting vibration is a breathing-like mode of the carbon rings on the graphene plane (see Figure 1.5) [17]. Another particularly interesting an useful property of the 2D band is the fact that intensity and shape of the related peak changes drastically from single-layer to double layer graphene. To take into account the change in intensity, the ratio between the G band and the 2D band is evaluated: for single layer graphene this ratio is between 3 and 4 [18], while is around 1 for double layer graphene (and graphite in general). Also, the shape of the 2D band changes: while it is given a single lorentzian curve in single-layer graphene [20], for double-layer graphene the peak is composed by four lorenztian curves and is then considerably broader [11]. These two characteristics have been used during the experimental work to verify the presence of graphene at the positions where the measurement was done.

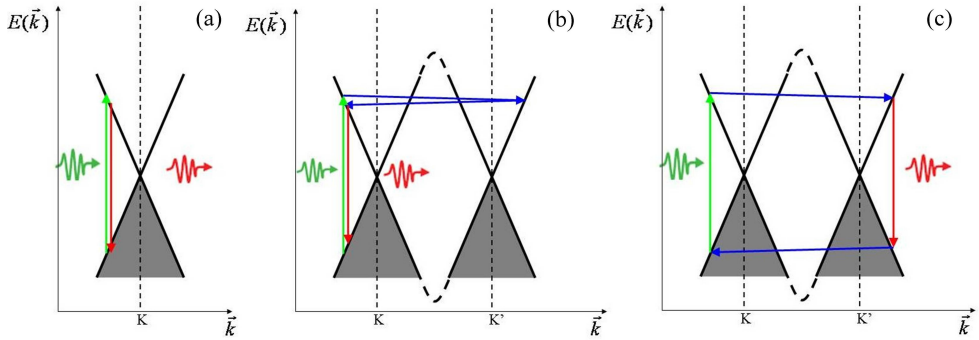

Figure 1.4: (a) phonon scattering at the Γ-point corresponding to the G band and (b, c) double scattering, corresponding to the 2D band. The scattering is pictured within the electronic bands, the characteristic cone band structure of graphene is represented. The green and red arrow represent the incoming and outgoing light, respectively. Adapted from [17, 18].

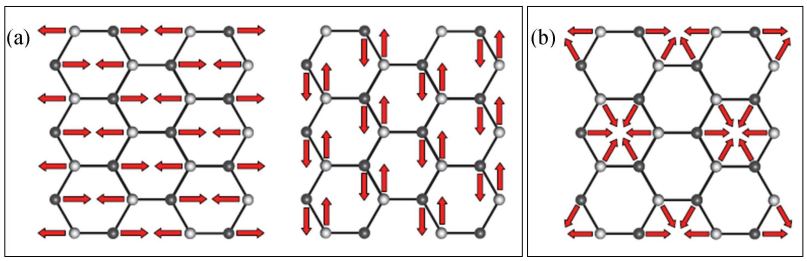

Figure 1.5: (a) representation of the lattice vibration for the TO (left) and LO phonons (right) at the center of the Brilluoin Zone (b) representation of the lattice vibration for the TO phonons at the K-point of the Brilluoin Zone. Adapted from [17].

Although some differences between the Raman spectrum of graphene and carbon nanotubes are present, as for exampled the appearance of the radial breathing mode [21], the just described G and 2D band scattering occurs also for carbon nanotubes with the same characteristic as for single-layer graphene.

Part II

Experimental Techniques

Chapter 2

Experimental Setups

In this chapter the experimental techniques are presented. The basic concepts of confocal microscopy are introduced, referring to the specific experiment performed in this work. Confocal Raman measurements have been done on gallium arsenide nanowires and gold nanorods deposited on single-layer graphene. Additionally, Raman experiments on graphene and carbon nanotubes have been performed using a gold nanotip, which needs to be brought in close proximity of the sample. This has been realized adding an atomic force microscopy head on the confocal setup. This experiment is described in an independent section. The white-light scattering and the dark field microscopy setup used for the characterization of the gold nanorods are also presented in this chapter.

Confocal and Tip Enhanced Near-Field Optical Microscopy Setup

Confocal Microscopy

The principle of confocal microscopy is to use a microscope objective to focus a laser beam on a sample in order to analyze a volume which is not bigger than the dimensions of the focus itself. The laser used in this experiment produces a Gaussian beam. So the spatial intensity distribution $I(r)$ can be described by:

$$I(r) = I_0 e^{-\frac{2r^2}{w^2}} \tag{2.1}$$

with I_0 being the intensity in the center of the beam and w being the radius of the transversal section of the beam. This quantity is defined as the distance from the center at which the intensity is diminished by a factor $\frac{1}{e^2}$. The intensity is maximal in the middle of the beam ($r = 0$) and decays with increasing distance. The minimal dimensions of the beam that can be reached are determined by the diffraction limit. The diffraction limit corresponds to the beam waist, which within the paraxial approximation is given by:

$$w_0 = \frac{\lambda f}{\pi w} \tag{2.2}$$

where λ is the wavelength, w is defined as before and f is the focal length, that is the ratio between the diameter of the input iris and the numerical aperture (NA), which is given by the refractive

index n and the angle of incidence θ according to $NA = n \sin\theta$. After having reached the minimum dimensions the beam diverges according to the formula:

$$w(z) = w_0 \sqrt{\frac{(\lambda z)^2}{(w_0 \pi)^2} + 1} \tag{2.3}$$

The beam is considered to be focused within a spatial region named *"Rayleigh Range"*, defined as the distance from the beam waist at which the area of the transversal section of the beam is twice larger than in the focal point, that is:

$$w(z_r) = w_0 \sqrt{2} \tag{2.4}$$

The focal volume is generally approximated to be cylindrical, the extension of the *Rayleigh Range* can be found according to eq. (2.3) and is calculated to be:

$$z_r = \frac{\pi w_0^2}{\lambda} \tag{2.5}$$

The larger the beam waist, the larger the focal volume. This means that the defocusing is inversely proportional to the beam waist: for a small section of the beam, the beam itself will be sooner defocused. This treatment holds for the first oscillation mode of the electric field in the laser cavity. To improve the spatial distribution of the incident field, a pinhole is usually installed. A fundamental condition for the confocal microscopy is the light not originating from the focal area is not detected. This is achieved either through the use of a pinhole or of a detector having detection area that is on the order of the dimension of the focus.

An image of the sample is formed by raster-scanning the focal volume though the sample while recording the optical response point-by-point. Raster-scanning is typically implemented using piezoelectric elements. The motion in the xy-plane is achieved through a piezo-scanner shifting the sample holder in two directions. In this way, the sample can be moved with respect to the laser focus so that a well determined area much bigger than the beam focus can be analyzed. The signal following from the laser excitation can be detected in relation with the position on the surface. The result are two dimensional maps where the signal intensity is detected as a function on the xy-position on the sample. The z-position of the focus is determined manually adjusting the position of the objective.

For the measurements on the gallium arsenide nanowires (GaAs NWs) on glass, the NWs are located scanning the laser focus across the sample and detecting the strong photoluminescence (PL) signal at 874 nm, corresponding to the band-gap of the Zinc Blend crystal structure (1.43 eV). The light is then directed to the spectrometer, where the spectra are measured. This procedure is repeated at different positions on the sample. A typical two-dimensional image obtained detecting the NWs PL, is presented in Figure 2.1.

The Raman signal is typically linear with the laser intensity (see Chapter 4). As it will be explained in Chapter 5, the key feature of the *dynamical back-action* is the deviation from the linearity of the Raman response in dependence on the laser power. To investigate this phenomenon, the Raman spectra of graphene and carbon nanotubes (CNT) in presence of plasmonic nanostructures are measured for different laser powers (in the following, it is referred to this procedure as "power

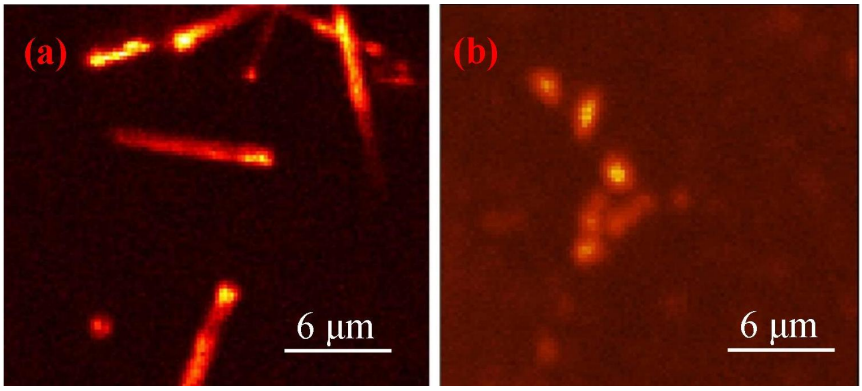

Figure 2.1: (a) confocal image of GaAs NWs deposited on glass, recored by detecting the PL signal at 874 nm. (b) confocal scan of gold nanorods on graphene. See text for further details.

series"). A fundamental part of the setup for this experiment consists of the combination of a lambda half plate and a Glens-Thompson polarizer. These components, when combined, allow for the modulation of the intensity of the laser. With the lambda-half plate the polarization of the laser can be turned. When the laser polarization is aligned parallel to the axis of the polarizer, the transmitted intensity is maximum. When the polarization is changed, the polarizer effectively reduces the transmitted intensity, because only a specific field component aligned to the polarizer axis is transmitted. During the power series, the lambda-half plate can be rotated by hand. The laser power is measured with a power-meter (THORLABS) after the pinhole in the excitation path (see below), after having rotated the lambda-half plate. This power, scaled by the reflectivity of the beam-splitter, is used to calculate the intensity incident on the sample. The beam waist is estimated tough eq. (2.2) to be around 350 nm. The dimensions of the nanorods are typically smaller than the beam waist (see Chapter 6). This means, that it is impossible with this diffraction limited resolution to distinguish how many nanorods are present inside the confocal spot.

In a "power series", a series of spectra is measured for every set laser power, typically 10 spectra for each power. On the spectrometer, the signal is measured as counts on the CCD camera (see below). The Raman intensity is obtained as the integral under the peak after background subtraction. For the graphene sample, the background cannot be taken on the sample substrate directly, being all the sample substrate covered with graphene. It then has to be subtracted computationally after the measurement. A power series consists typically of 10 points. To obtain one as those presented in Chapter 7, around 100 spectra have been measured and evaluated. For the measurements on the sample where gold nanorods are deposited on graphene, the nanorods are located on the sample through confocal scans similarly as for the NWs. The gold nanorods appear as "hot-spots" on the graphene Raman background. The signal increase is due partially to the field enhancement and partially to the gold inelastic scattering (see Chapter 3 and 6 for further details). The confocal set up utilized in this work contains the following elements (refer to Figure 2.2):

- Helium-Neon laser with emission centered at 633 nm (A). Alternatively a Helium-Neon laser centered at 594 nm has been used.
- Lambda-half plate WPH05M-633 THORLABS (B), used to rotate the laser polarization. For

the measurements with the nanotip a Liquid Crystal Retarder (LCR) is used in spite of the lambda-half plate (see next section).

- Glens-Thompson Polarizer (C), used to select the laser field component having the desired polarization and modulate the intensity. Doing so, it is made sure that the polarization does not change during the power series and that consequently the laser power is the only changing parameter.
- Mirror (D).
- Lenses having focal length of 30 mm (E), 80 mm (F), 50 mm (G), 150 mm (H) mounted in order to expand the beam.
- A 25 μm diameter pinhole (I).
- The microscope equipped with an objective having NA equal to 1.49 and 100x magnification (J). Alternatively, for the measurements on nanowires a 1.4 NA objective with 60x magnification has been used (both objectives are from NIKON). In the microscope a CHROMA ZT633rdc beam splitter is mounted (K). Alternatively, also a Melles-Griot 03BTL005 beam splitter (50:50 at 633 nm)has been used. A lens is mounted in the microscope delivering a collimated beam at the output of the microscope itself. The sample holder of the microscope is mounted on a piezo-stage (Physik Instrumente PI P517, 3).
- Filter to exclude the laser wavelength (L), 633 Semrock LP02-633RE.
- Flip-mirror (M) to direct the emitted radiation on a spectrometer.
- Spectrometer (O), Andor Solis Sharmrock 303i, equipped with CCD Camera, Andor iDUS 420-BR-DD, which is used to measure emission spectra.
- A dicroic mirror (P), ChromaR NC113866 590 dcxr, reflecting light at wavelength shorter than 760 nm, can be used to separate Raman scattering and photolominescence signal of CNT.
- Mirror (R).
- Lens 75 mm (Q,S) to focus the beam on the active area of the Avalenche Photodiods (APD).
- Avalanche Photodiodes (APD), (V, W), Perkin ElmerR SPCM. Depending on which signal is detected, appropriate filters are put in front of the APDs. For the G and 2D band, bandpass filters centered at 700 and 760 nm respectively are used (THROLABS). They both have a bandwidth of 10 nm. For the detection of the NWs PL, a 810 nm long-pass filter (CHROMA) is used.

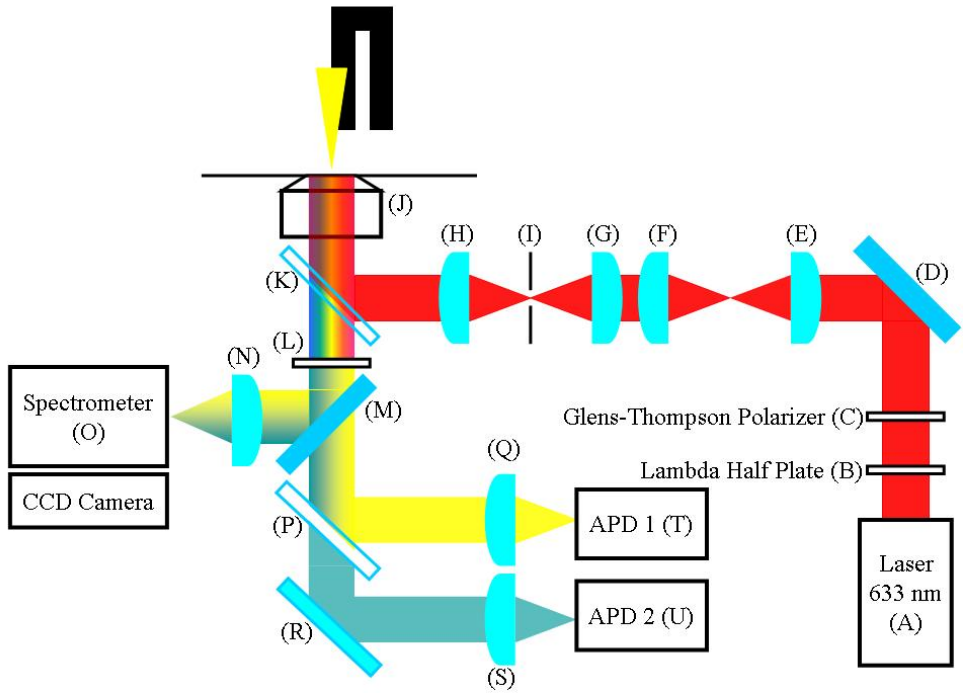

Figure 2.2: schematic of the confocal setup. The laser is in real color, while the transmitted light is in false color (the detected wavelengths are in the near-infrared.) On top also the gold nanotip in a shear force configuration is shown (see next section).

When detecting the signal using the spectrometer, the detection efficiency in dependence of the wavelength needs to be considered. The wavelength dependent detection efficiency is plotted in Figure 2.3. Throughout this work, the G band 2D band of graphene and CNT appear at 703 and 760 nm respectively, when a 633 nm excitation laser is used. The ratio between the efficiency at these two wavelengths is 0.81.

Tip Enhanced Near-Field Optical Microscopy (TENOM)

In the last decades, several experimental configurations have been presented, allowing to bring a metallic nanotip in close proximity of the sample surface. This kind of technique is known as Tip Enhanced Near-Field Optical Microscopy (TENOM)[6, 22, 23]. In this thesis, a shear-force atomic force microscopy (AFM) head is used to land the nanotip on the sample surface. The nanotip is mounted on the AFM-head, which is equipped with a z-piezo for nanotip-sample distance control. Additionally, two xy-piezo are included in the AFM-head, to position the tip in the laser focus [24]. Specifically, the nanotip is attached to a quartz tuning-fork, which oscillated in the parallel direction to the sample surface. For this reason, this configuration is called "shear-force" [25, 26]. The tuning-fork oscillation is driven by a voltage-controlled dither-piezo. When close to the sample surface, the interaction between the nanotip and the surface causes a shift of the effective resonance frequency of the tuning-fork. The shear-force mode is based on a phase-locked-loop

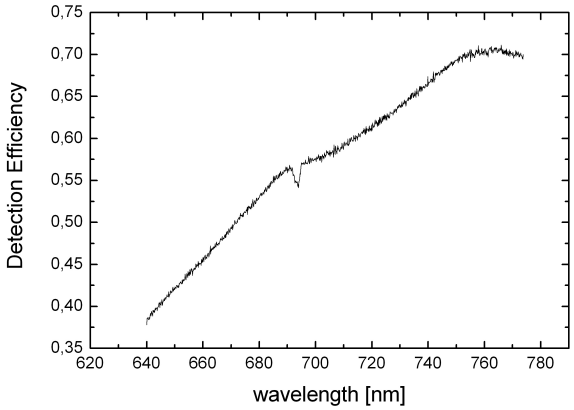

Figure 2.3: Detection efficiency of the setup, when the signal is detecting using the spectrometer.

system (easy-PLL plus NanoSurf), which allows for the detection of the change in the resonance frequency. During the scan, when a change in the resonance frequency is detected, a feedback controller changes the voltage applied to the z-piezo until the initial frequency corresponding to the user-defined set-point is retained. In this way, the nanotip-sample distance is kept constant. The morphology of the sample is recorded from the voltage applied to the z-piezo to restore the resonance frequency.

When recording the power series, the sample is not scanned, so that the nanotip stays, ideally, at the same sample position during all the measurement. A problem here is the drift of the xy-piezo in the head, which makes it difficult to keep the nanotip position constant on the sample. During this kind of measurement, the table cannot be touched when the nanotip is landed. Because of this reason, the lambda-half plate is substituted with a Liquid Crystal Retarder LCR-1-VIS (THORLABS), which can be driven through an external voltage (for the generation of the voltage, a Wavegenerator 2400 Keithley Instruments is used). The polarization of the incident field can be rotated by different angles changing the amplitude of the voltage applied to the LCR. The laser power corresponding to the different voltages is known from a previous calibration with power-meter.

White Light Scattering Setup

The plasmon resonance frequency related to a metallic nanostructure depends on the medium surrounding the nanostructure itself (see Chapter 3). For these reason, it is important to record the plasmonic resonance directly on the sample, in order to have a reliable estimation of the plasmonic properties. This is done measuring the elastic scattering spectrum of the utilized metallic nanostructures directly on the sample surface. To this aim, a white light source is needed. In this work, white light generated from a photonic crystal fiber has been used as a first approach. The principle at the base of photonic fibers is that of broadening a short laser pulse, by a combination of several non-linear effects. These effect can find place in nonlinear media and designed hollow structures such as photonic crystals. In this thesis, a Femto WHITE 800 crystal fiber has been used [19]. As input a Ti:Sapphire (Mira, COHERENT) pulsed laser has been used, centered for this experi-

ment at 800 nm, corresponding to the optimum working wavelength of the photonic fiber. For this measurement a 800 nm Long-Pass filter (CHROMA) must be used to block the laser radiation.

Dark-Field Setup

Alternatively, the elastic scattering of has been measured with a dark field microscope. The principle of dark field microscopy, is that the light used for the excitation is not collected in the detection. This allows to improve the optical contrast. Typical optical dark field images show bright spots on top an almost dark background (from which the name "dark field"). See Figure 6.7 for an example. This is standardly achieved by blocking the central part of the excitation beam before focusing it on the sample. After focusing, both the excitation beam and the signal coming from the sample diverge. When diverging, the excitation beam misses the collection lens while the signal, which is emitted on a solid angle is collected. The dark field microscope used in this work is a home-built microscope (Olympus BX51 microscope, Princeton Instruments SP2300i Acton Standard Spectrograph, Princeton Instruments PIXIS 256E CCD detector), belonging to the group of Prof. Tim Liedl in the Faculty of Physics of the LMU Munich and was operated by **Francesca Nicoli**. All measurements were taken using a 100W halogen lamp with an oil condenser (Olympus U-DCW NA1:4), a MPLFLN-BD 100x/NA 0:9 Olympus objective, and a grating of 300 g/mm 500-nm blaze. Unfortunately, it was impossible to find the same position analyzed on the dark-field microscope, when measuring on the confocal microscope.

Additionally, Transmission Electron Microscopy (TEM) measurement on gold nanorods have been performed at the Chemistry Department of the LMU Munich by **Dr. Andreas Wisnet** and **Dr. Sophia Betzler**. The statistical analysis on the gold nanorods aspect ratio and diameter distribution was done by **Dr. Richard Ciesielsky** and **Harald Budde** at the Chemistry Department of the of LMU Munich. TEM measuremenst on beryllium doped gallium arsenide nanowires by **Dr. Sriram Venkatesan** at the Max-Planck-Institut für Ei senforschung Düsseldorf.

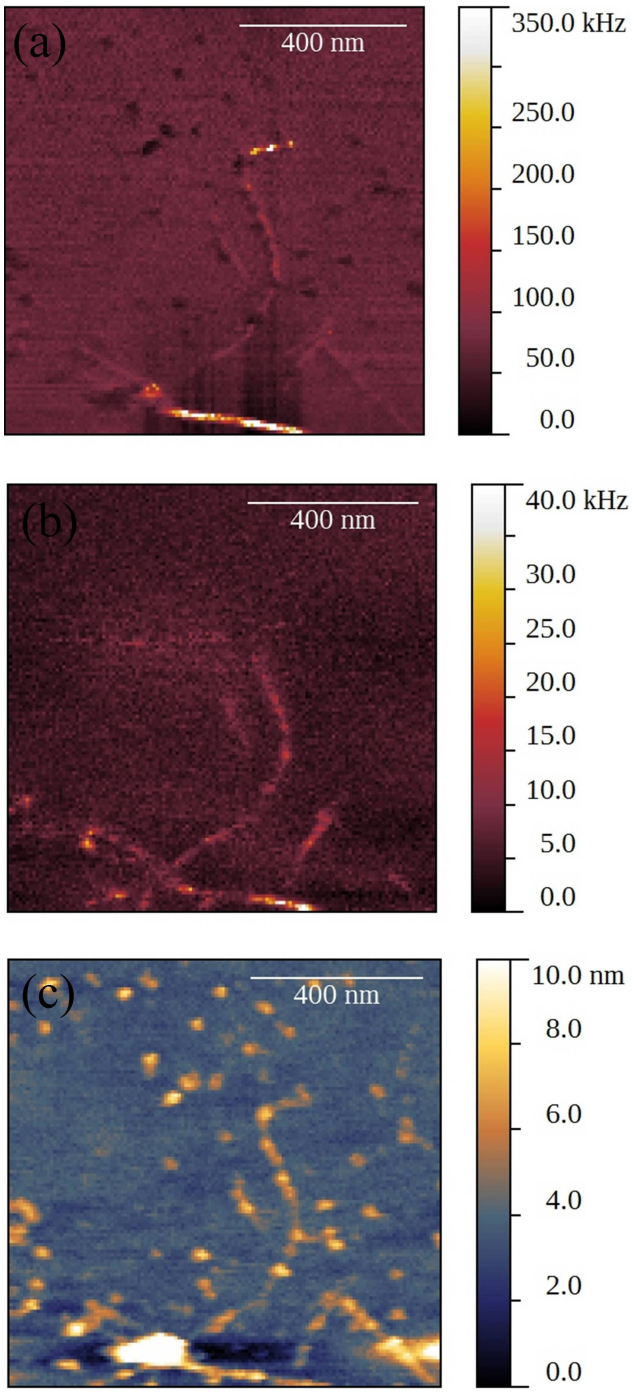

Figure 2.4: TENOM measurement where CNT photoluminescence (a), Raman Scattering (b) and topography (c) are recorded at the same time. On this lengthscale the here observed CNT would be indistinguishable.

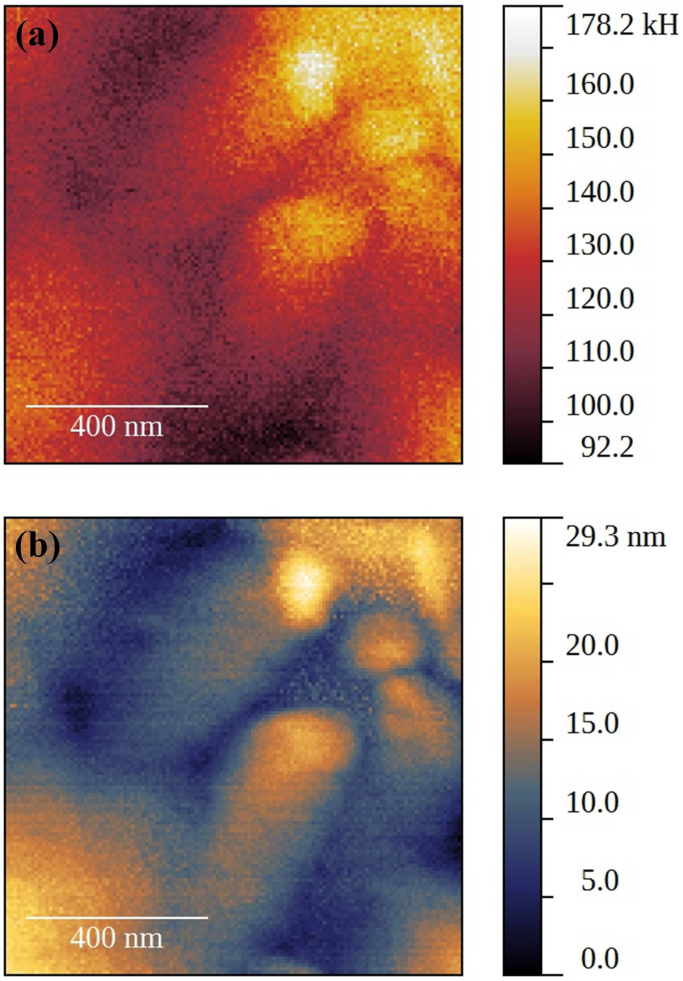

Figure 2.5: TENOM measurement of a pentacene thin film. The optical signal (a), composed in this case by bot Pl and Raman, and the topography (b) show the same spatial resolution about 20 nm. The Pentacene film was prepared at the Faculty of Physics of the LMU Munich by **Clemens Liewald** in the group of **Prof. Bert Nickel**.

Part III

Plasmon Assisted Raman Scattering of Carbon Nanotubes and Graphene

Introduction

In the last few decades, a variety of plasmon enhanced spectroscopy techniques have been developed, such as Tip Enhanced Near-Field Optical Microscopy (TENOM), Tip Enhanced Raman Spectroscopy (TERS), Surface Enhanced Raman Spectroscopy (SERS) and others [6, 22, 23]. These are all powerful techniques, allowing for a strong signal enhancement and to overcome of the diffraction limit. In addition, TENOM and TERS always provide the topographic information, deriving from the scanning of the tip on the sample. Measurements similar to that shown in Figure 2.4 can provide information, for instance, about the exciton localization in carbon nanotubes (CNT) [27]. This information would be totally hidden in a diffraction limited measurement. Besides purely optical signals, also the photocurrent [28] and electroluminescence [29] of CNTs have been successfully measured, giving a more detailed characterization of the observed system. Furthermore, recent advances in combining optical detection with Scanning Tunnel Microscopy (STM) have led to achieve subnanometer resolution at the nanogap between a silver nanotip and a silver film [30, 31, 32].

In addition to the improvement of the spatial resolution, the Raman signal of a porphyrine molecule inside the nanogap has been shown to increase non-linearly with the laser power [30]. This last experimental observation is of high interest [33], because this plasmon-mediated non-linear Raman response is potentially an important contribution to the TERS/SERS scenario that has not been explored up to now. Complementary to these developments, new progresses in lithographic techniques have allowed for the successful fabrication of dimers having extremely small distance, down to few Å [34]. The so achieved experimental accessibility to these extreme electromagnetic field confinement conditions, have been combined with the development of quantum plasmonic models, with the aim to describe non-classical phenomena such as quantum size effects [35, 36], quantum electron screening [37, 38] electron "spill-out" [39], atomic description of the field distribution[40, 41]and quantum electron charge transfer [42, 43]. In this context, two models have been proposed, predicting a non-linear response in dependence on the laser power for a Raman emitter coupled to a localized plasmon. The first relays on an optomechanical description of the process [44], while the second is based on a quantum-electrodynamic description (QED) [45]. The overall framework proposed in both works consists of a harmonic oscillator (the Raman emitter) coupled to a photonic cavity (the localized plasmon). Both models predict that the best condition for observing a non-linear Raman response is achieved when the laser frequency is higher than the frequency of the plasmonic resonance (this condition is described in the literature as *blue-detuning* [44, 45]). Also from experimental works [30, 34, 46] the *blue-detuning* seems to be the best condition to achieve the maximum Raman response. On the other hand structures having different plasmonic resonances have shown the same behavior at the same laser excitation wavelength (therefore in totally different *detuning* conditions) [34]. Moreover, the estimation of the rate of the Raman response is usually done estimating the enhancement factor in dependence on the excitation wavelength [34, 46]. The best efficiency obtained when exciting at the blue side of the plasmonic resonance, could then be attributed to the best compromise between enhancement of the exciting and scattered field [46]. For these reasons, a further understanding of the experimentally observed non-linearity of the Raman scattering is needed [33].

In the experimental work described in this thesis, the Raman response of the G and 2D band of graphene coupled to a localized plasmon is systematically measured in dependence on the laser power. Graphene is chosen as Raman emitter, as the sufficient spectral distance between its two

main Raman lines (G and 2D band) allows to investigate different regions of the plasmonic resonance. Different excitation wavelength and different plasmonic nanostructures are used with the aim of testing different *detuning* conditions. In contrast to previous work [30, 34, 46], a moderate field enhancement regime is chosen. Correspondingly, isolated metallic nanostructures are taken as plasmonic systems, instead of a nanogap. With this experimental configuration it can be answered, if a localized plasmon alone, seen as a resonant system coupled to a Raman emitter, can give rise to the theoretically predicted non-linear effect, or if other phenomena related to a subwavelength plasmonic nanocavity need to be invoked. In this sense, the generality of the occurrence of this non-linear phenomenon can be tested.

Chapter 3

Plasmon Enhanced Spectroscopy

The different plasmon enhanced spectroscopy techniques mentioned in the introduction are all based on a local field enhancement given by a metallic nanostructure (generally of gold or silver) having dimensions much smaller than the wavelength used for the analysis. The nanostructure is put in the focus of a laser beam and is used to provide a local near-field excitation source to record a local spectroscopic response of the sample. In addition, the spontaneous rate emission can be locally enhanced. The enhancement is given from the fact that the incident light drives the free electrons in the metal along the direction of polarization of the field, giving rise to an accumulation of charges on the surface of the metal. This surface charge forms oscillations which locally strongly amplify the field. In this chapter, the concepts of surface plasmon polaritons and localized surface plasmon polaritons are introduced, as basis for understanding Plasmon Enhanced Spectroscopy, with particular attention to Plasmon Enhanced Raman Spectroscopy.

Localized Surface Plasmon-Polaritons

By definition, surface plasmons are quanta of surface-charge-density oscillation [47]. The same terminology can be used also for collective oscillation in the electron density at the surface of a metal. The surface charge oscillations are coupled to electromagnetic waves. This explains the definition as *"polariton"*. Nonetheless, the term plasmon is also often used alone, without specifying the presence of electromagnetic waves. Surface plasmons have been first observed and discussed for plane interfaces. In the case of propagation along the interface between a metal and a dielectric, the electromagnetic field is localized in one dimension, normally to the interface. In the context of nano-optics, a number of alternative configuration have been proposed, in order to further confine the electromagnetic field in two or three dimensions [48]. Because of this confinement, it is usually referred to plasmons in nanostructures as *"localized surface plasmon-polariton"*. For the purpose of this thesis, the three dimensional confinement is of interest, since it will be dealt with metallic nanotips and nanorods.

In the following, the response to an external electromagnetic field from a metallic nanostructure in a dielectric medium is considered. The typical dimension of the nanostrucures taken under consideration (few tens of nanometers) is much smaller then the wavelength of light in the visible range. This allows to look for a solution within the quasi-static approximation [49]: retardation effects

can be neglected and it can be assumed that all points of the object respond simultaneously to the incoming field. In this approximation the electric field can be represented by a potential: $\vec{E} = -\nabla\phi$ where the potential has to satisfy the Laplace equation $\nabla^2\phi = 0$. Also, the boundary conditions between the two different media need to be considered. The Laplace equation can be solved analytically for spheres. This solution can be used for studying the local plasmon in a nanoparticle, which is taken in the following as a model. The electromagnetic field outside the nanosphere corresponds to that generated by a dipole induced by the external field, having polarizability:

$$\alpha = 4\pi a^3 \frac{\epsilon_m - \epsilon_d}{\epsilon_m + 2\epsilon_d} \tag{3.1}$$

where ϵ_m and ϵ_d are the metal and the surrounding medium dielectric functions respectively. a is the radius of the nanosphere. The metal dielectric function can be expressed as:

$$\epsilon_m = 1 - \frac{\tilde{\omega}_P^2}{\omega\left(\omega + i\tilde{\kappa}\right)} \tag{3.2}$$

where $\tilde{\omega_P}$ and $\tilde{\kappa}$ are respectively the intrinsic metallic plasma frequency and damping. Inserting eq. (3.2) in (3.1), the spectral response of the localized plasmon field shows a resonant behavior. The spectral position of the resonant frequency is given by the condition $\epsilon_m + 2\epsilon_d = 0$. Provided that the incident field has the appropriate frequency, the field around the particle can be much higher than the incident one. This property of the metallic nanoparticle to increase the incident field, is what is referred to as *local field enhancement*. The field enhancement factor, in dependence on the position around the particle, is defined as:

$$f(\vec{r}) = \frac{|\vec{E}_{loc}(\vec{r})|}{|\vec{E}_L(\vec{r})|} \tag{3.3}$$

$\vec{E}_{loc}$ is the local electric field, and $\vec{E}_L$ is the laser electric field. Following from the field distribution around the nanoparticle, the enhancement factor can be very high in the close proximity of the metallic surface (≈ 10 nm). It decays quickly for increasing distance.

The plasmon modes of a metallic nanotip are similar to those of a semi-infinity surface plasmon-polariton for very large tip radii and become more and more similar to those of a nanoparticle for smaller radius [47]. These are characterized by a much stronger field localization. In the electrostatic approach, considering the metallic nanotip as a perfect conductor, the main effect of field enhancement at the tip is derived from the lighting rod effect, that gives stronger variations of the potential for smaller radii. In the optical range, the field is further enhanced by the response of the localized surface plasmon. These two effects together give what is defined as *electromagnetic field enhancement*. The localized plasmon resonance is typically $\approx 10^{13}$ Hz broad in the visible range for a nanoparticle and can be even broader for a nanotip. In a typical Raman experiment, the excitation wavelength and the frequency of the scattered light lay close enough to be both within the plasmon resonance spectral range. The scattered field will then be enhanced with a similar enhancement factor as the incident one. The resulting scattered field will then be enhanced by the square of the enhancement factor, and correspondingly measured intensity will be enhanced by the fourth power of the enhancement factor. This exceptional property of plasmon enhanced Raman scattering is usually referred to in literature as the *"f^4-law"*[51, 52].

Beside metallic nanotips, also metallic nanorods are used in this thesis as plasmonic probes. Compared to a nanosphere the nanorod is anisotropic, consisting of a long and a short axis. The polarizability is going to be different from one axis to the other and depend on the aspect ratio between the two. Correspondingly there will be two plasmon resonances, characterized by two different resonance frequencies, each of which corresponds to the electron density oscillation in the direction of either one axis or the other. To get the full picture, the full vector wave equation need to be considered [50]. In the easiest picture, a rod can be considered as ellipsoid. In this case, the two polarizabilities are[49]:

$$\alpha_{long(short)} = \frac{4\pi}{3} L_{long} L_{short}^2 \frac{\epsilon_m - \epsilon_d}{\epsilon_d + P_{long(short)} (\epsilon_m - \epsilon_d)} \tag{3.4}$$

$$P_{long} = \frac{1-e^2}{e^2} \left[\frac{1}{2e} ln \left(\frac{1+e}{1-e} \right) - 1 \right] \tag{3.5}$$

$$P_{short} = \frac{1 - P_{long}}{2} \tag{3.6}$$

where L_{long} and L_{short} are the long and short axis direction respectively and $e = \frac{L_{long}}{L_{short}}$ is the aspect ratio.

When the plasmonic resonance of a nanostructure is measured optically, the quantities which play a role are the absorption and the scattering cross-sections. The sum of the two gives the extinction cross-section. Mathematically, they are related to the polarizability of the nanostructure. For a nanosphere they are given by:

$$\sigma^{scattering} = \frac{k_0^4}{6\pi} |\alpha|^2 \tag{3.7}$$

$$\sigma_{absorption} = k_0 \alpha \tag{3.8}$$

where k_0 is the wavenumber of the incident electric field.

Chapter 4

Stimulated Raman Scattering

In this chapter the stimulated Raman process and its physical and mathematical description are introduced. This is useful for the purpose of this thesis, because it allows to illustrate the Raman emitter as a harmonic oscillator. Indeed, in the case of spontaneous Raman scattering, the Raman emitter can be described as a damped harmonic oscillator, while in the case of stimulated Raman scattering it can be described as a driven damped harmonic oscillator. Furthermore, the first experimental observation of a non-linear Raman process at the nanogap between a silver tip and a silver film [30] has been explained as process stimulated by the plasmonic field related to the nanogap itself. In the second section of this chapter, this interpretation is discussed, in the frame of a more general description of a stimulated process driven by a plasmonic field.

Stimulated Raman Spectroscopy

In a spontaneous Raman process, the change of the polarizability of the Raman scatterer, which depends on the vibrational coordinate, changes the frequency of the scattered field. This can be seen expanding the polarizability as (compare with Chapter 1):

$$\alpha = \alpha_0 + \frac{\partial \alpha}{\partial x_v} x_v \tag{4.1}$$

where α is the polarizability itself and x_v is the vibrational coordinate. If an harmonic time dependence is assumed for both the laser electric field E_L and the vibrational coordinate x_v, the scattered field related to a Stokes scattering process can be expressed as [3] [1] :

$$E_S(t) = \frac{\omega_S^2}{4\pi\epsilon_0 c^2} x_v(t) \frac{\partial \alpha}{\partial x_v} E_L(t) = \frac{\omega_S^2}{4\pi\epsilon_0 c^2} x_0 \frac{\partial \alpha}{\partial x_v} E_L e^{-i(\omega_L - \omega_v)t} \tag{4.2}$$

where x_0 is the amplitude of the vibration, E_L is the amplitude of the laser electric field, ω_L and ω_v are the laser and vibrational frequency respectively. $\omega_S = \omega_L - \omega_v$ is the the frequency of the scattered field for the Stokes process. For the Anti-Stokes process the frequency of the scattered field is $\omega_{AS} = \omega_L + \omega_v$. In a spontaneous Raman scattering process the vibrational amplitude is

[1] In eq. (4.2) the spatial and angular dependence of the electric field is ignored for simplicity. The complete formula can be found in [3].

independent on the laser field intensity (see below). Correspondingly, the amplitude of the scattered field increases linearly with the laser field amplitude.

In stimulated Raman scattering (SRS) two laser beams oscillating at different frequencies coincide on the sample [53]. For reasons that are explained in detail below, the difference between these two frequencies must be equal to the frequency of the vibrational mode. In this condition the scattered Raman signal is increased, (*Stimulated Raman Gain*) while the intensity of the pump is decreased (*Stimulated Raman Loss*). In a conventional SRS experiment the gain or the loss are measured [54]. SRS has been used for biological and biomedical imaging having the advantage, compared to Coherent Anti-Stokes Raman Scattering (CARS), of not exhibiting a non-resonant background [55]. The vibration related to the vibrational mode can in general be described as that of a harmonic oscillator, being characterized by a resonance frequency and a damping. An external electric field, like that associated to a laser for instance, can be thought to apply a force to a Raman emitter [3, 4]. It is usually referred to this force as the *radiation force*, or the *radiation pressure* [47, 56]. This force is related to the energy of the system, according to:

$$F = -\frac{\partial U}{\partial x_v} \tag{4.3}$$

as before x_v is the vibrational coordinate. The system composed by a Raman emitter and an electric field is described as a dipole interacting with an external electric field. The dipole is for a Raman emitter associated to its polarizability. The equation relating the dipole and the polarizability is usually expressed as the scalar analogous of eq. (1.2) [2]:

$$p = \alpha E \tag{4.4}$$

The energy U of the system is then:

$$U = -\alpha |E|^2 \tag{4.5}$$

The polarizability can be expanded as a function of vibrational coordinate, as in eq. (4.1). Following from eq. (4.3), the force applied on the Raman emitter is then equal to:

$$F = \frac{\partial \alpha}{\partial x_v} |E|^2 \tag{4.6}$$

This force can be inserted in the equation of an harmonic oscillator:

$$\frac{\partial^2 x_v}{\partial t^2} = -\omega_v^2 x_v - \gamma_v \frac{\partial x_v}{\partial t} + \frac{\partial \alpha}{\partial x_v} \frac{|E|^2}{m} \tag{4.7}$$

m is the effective mass of the harmonic oscillator. From eq. (4.7) it is clear why the Raman process is spontaneous in presence of a monocromatic exciting field. In such a case, the radiation force is a constant and there is no quantity oscillating in time which could drive the oscillation. The situation is different in the case of SRS. Here, two laser sources are present, which electric field amplitude and frequencies are labeled as $E_{1,2}$ and $\omega_{1,2}$, respectively. The total field is now given by the sum of the two fields and its modulus square has two components oscillating in time, namely:

$$|E|^2 = E_1^* E_2 e^{-i(\omega_1 - \omega_2)t} + E_1 E_2^* e^{-i(\omega_2 - \omega_1)t} \tag{4.8}$$

[2] remember that the polarizability depends on the vibrational coordinate x_v and consequently on the vibrational frequency ω_v (see eq. 4.1 and 4.2)

The constant terms of the modulus square of the total field are neglected in eq. (4.8), because they cannot drive the harmonic oscillator. On the other hand, the components oscillating in time can in principle efficiently drive a harmonic oscillator. One can set $\tilde{\omega} = \omega_1 - \omega_2$, and describe the time dependence of the amplitude of the harmonic oscillator as $x_v(t) = x_0 e^{-i\tilde{\omega}t}$ (compare with eq. 4.2). If for instance the first component in eq. (4.8) is inserted in the equation for the harmonic oscillator, it turns out that the amplitude of the harmonic oscillator depends on the field frequencies and amplitudes according to:

$$x_0(\omega) = \frac{\frac{\partial\alpha}{\partial x_v} E_1^* E_2}{\tilde{\omega}^2 - \omega_v^2 - i\gamma_v\omega} \tag{4.9}$$

The oscillation is then in this case not spontaneous, but it is rather driven by the total electric field. If the Raman shift is measured with respect to E_1, the amplitude of the scattered field is (compare again with eq. 4.2) [3]:

$$E_S \sim x_0 \frac{\partial\alpha}{\partial x_v} E_1 \sim \frac{(\frac{\partial\alpha}{\partial x_v})^2 |E_1|^2 E_2}{\tilde{\omega}^2 - \omega_v^2 - i\gamma_v\omega} \tag{4.10}$$

From eq. (4.10) follows that the scattered field has a quadratic dependence on the field E_1 with respect to which the Raman signal is measured. It is worth to point out, in relation to the discussion of the experimental results, that while the spontaneous Raman scattering depends linearly on the polarizability change $\frac{\partial\alpha}{\partial x_v}$, the stimulated Raman scattering depends on its square. Therefore, for a larger $\frac{\partial\alpha}{\partial x_v}$ (as it is the case for the 2D band with respect to the G band, see Chapter 7), both spontaneous and stimulated Raman scattering should become stronger. It should also be notices that, the vibrational damping, γ_v, is in the real case much smaller than the optical frequencies. It then turns out, that the stimulated field is non-zero for the condition:

$$\tilde{\omega} = \omega_1 - \omega_2 = \omega_v \Rightarrow \omega_2 = \omega_1 - \omega_v \tag{4.11}$$

When this condition is satisfied, the Stokes Raman process is stimulated. The useful condition for the Anti-Stokes stimulated process $\omega_2 = \omega_1 + \omega_v$ can be obtained inserting the other field component of eq. (4.8) in eq. (4.7). Importantly, this process is wavelength selective, in the sense that if ω_2 does not satisfies the afore mentioned condition, the stimulated process is not taking place. Indeed, if the difference between the two laser frequencies does not match the vibrational frequency, the stimulated amplitude goes to zero. This wavelength selectivity makes it possible to use as second beam a broad-band laser pulse, allowing to stimulate the whole Raman spectrum at the same time without changing the spectral position and the width of the Raman lines. This concept is at the basis of Femtosecond Stimulated Raman Spectroscopy (Fs-SRS) [57].

Stimulated Raman scattering in the presence of a Plasmonic Field

In first approximation a plasmonic field can be described as a harmonic electric field oscillating as its resonance frequency ω_P and decaying in time with a damping factor κ. The sum of such a field with the field of the laser is given by:

$$E = E_L e^{i\omega_L t} + E_P e^{i\omega_P t - \kappa t} \tag{4.12}$$

This electric field can be taken as the total electric field and its squared amplitude can be inserted in eq. (4.6). This yields:

$$F = \frac{\partial \alpha}{\partial x_v} E_L^* E_P e^{+i(\omega_L - \omega_P) - \kappa t} \tag{4.13}$$

This force can be inserted in eq. (4.7). The so formulated harmonic oscillation equation can be still solved using Fourier Transformation. Writing $x_v(t) = \int_{-\infty}^{+\infty} d\omega e^{-i\omega t}$ and taking the partial derivatives inside the integral, eq. (4.7) becomes:

$$x_0(\omega) = \frac{1}{\omega_v^2 - \omega^2 - i\gamma_v \omega} \frac{\partial \alpha}{\partial x_v} E_L^* E_P \int_{-\infty}^{+\infty} d\omega e^{-i\omega t} e^{+i(\omega_L - \omega_P) - \kappa t} \tag{4.14}$$

Considering the Fourier Transformation:

$$\int_{-\infty}^{+\infty} d\omega e^{-i\omega t} e^{+i(\omega_L - \omega_P) - \kappa t} = \frac{\frac{\kappa^2}{4}}{\left[(\omega - \omega_L - \omega_P)^2 + \frac{\kappa^2}{4} \right]} \tag{4.15}$$

the amplitude of the oscillation finally becomes:

$$x_0(\omega) = \frac{\frac{\partial \alpha}{\partial x_v} \frac{\kappa^2}{4} E_L^* E_P}{[\omega_v^2 - \omega^2 - i\gamma_v \omega] \left[(\omega - \omega_L - \omega_P)^2 + \frac{\kappa^2}{4} \right]} \tag{4.16}$$

The amplitude of the oscillation is driven by the sum of the two fields as before. The plasmonic damping factor is typically much larger than the vibrational one ($\kappa >> \gamma_v$). Therefore, as in a two-beams stimulated Raman scattering process, the width and the position of the Raman peak remain those characteristic of the vibrational mode. The driven amplitude on the other hand depends on the frequency match between laser and plasmon. In particular the amplitude is maximum when the difference between the laser and plasmonic frequency matches the vibrational frequency. Consequently, the scattered field amplitude will also scale with the same dependence on laser, plasmon and vibrational frequency. It is important to point out that no difference between the *blue* and *red detuning* is predicted according to this model: the difference between laser and plasmon frequency is squared and the total response is consequently independent on its sign. This is a fundamental difference with the model presented in Chapter 5. Again consistently with a two-beams stimulated Raman process, the scattered field increases quadratically with the laser field and linearly with the plasmonic field. On the other hand, the plasmonic field is linearly dependent on the laser field. In this picture then, the scattered Raman field has a cubic dependence on the laser field. In Chapter 7 the experimental results are compared with this model. In relation to that, it is discussed if the deviation from linearity of the Raman signal in dependence on the laser power can be described with a quadratic or a cubic function. Also, it is discussed how the experimental occurrence of the non-linearity depends on the match between the vibrational frequency and the difference between plasmonic and resonance frequency and how this compares to the theoretical prediction just presented here.

In this last description the plasmonic field has been taken to oscillate at a single frequency corresponding to its resonant one. An alternative description [30] is based on the analogy with Fs-SRS. In the presence of a plasmon, the plasmonic field is thought to act as the second beam needed in a SRS as before, but it would not be monochromatic. The plasmonic field is rather imagined to be a

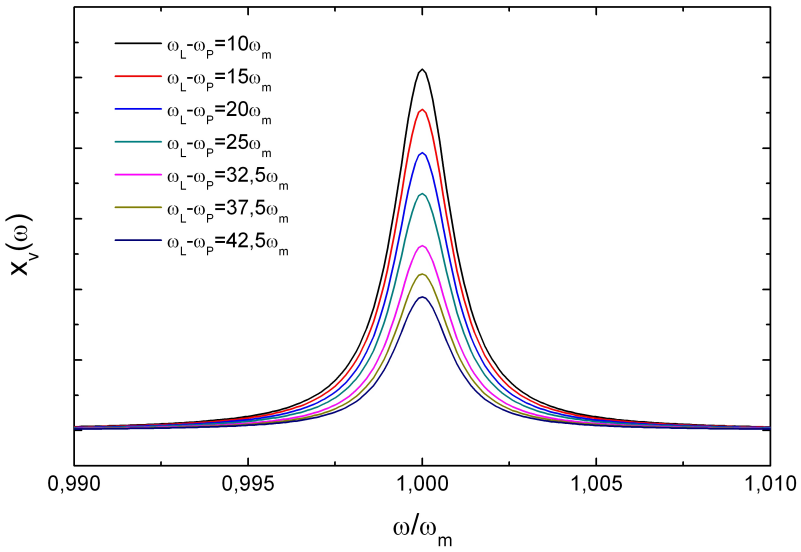

Figure 4.1: Amplitude of the Raman peak in the plasmon stimulated Raman picture. The amplitude is plotted in dependence on the frequency for different mismatch between the laser and plasmon frequency and the vibrational frequency. Both the frequency and the mismatch are given in unit of the vibrational frequency. The peak position and width do not change for different mismatching and are always those characteristic of the spontaneous vibration. Only the amplitude depends on the mismatching and is maximum for the condition $\omega_L - \omega_P = \omega_m$.

broad-band field, similarly to a fs-pulse. In this picture then, the scattered field should correspond to that given in eq. (4.10), where the frequency ω_2 satisfying the resonance condition is selected from the broad-band spectrum. It remains an open question anyhow, whether the plasmon can really act as a broad-band source. It is true that a broad-band background is always associated to a plasmon enhanced measurement, coming from inelastic electron scattering inside the metallic nanostructure [58, 59]. On the other hand, as it appears from eq. (4.10) , the second incident field must be sensibly different from zero. In the afore mentioned work [30] and in the experiments presented in the following, when the Raman shifted frequency is measured, the field at ω_2 is detected as well together with the whole plasmonic background. The intensity of this field is very far from being comparable with the intensity of a laser source. The optically detected plasmon background can then hardly be imagined to be sufficiently strong to give rise to a stimulated Raman scattering process.

Chapter 5

Description of the Coupled System

In this section, the system composed by the Raman emitter and the plasmonic nanostructure is described as a coupled system. In this sense, the vibrational mode and the plasmonic field are allowed to exchange energy. The total energy is then given by the sum of the vibrational energy, the electromagnetic energy of the plasmonic field and the interaction energy. This interaction energy is defined though a coupling factor. The presented description is analogous to that of an optomechanical system in which, for instance, one of the mirrors of a Fabry-Perot cavity is mechanically coupled to a spring [61]. In such a system, the radiation pressure acting on the mirror excites the mechanical oscillation of the spring. This oscillation changes the distance between the two mirrors, and consequently the resonance frequency of the cavity. In the system considered here, the vibrational mode and the plasmon, which is described as a resonant system, correspond to the mechanical oscillator and to the Fabry-Perot cavity respectively. Analogously to the optomechanical system, the electric field excites the vibrational mode, which in return can modify the electric field. Under certain conditions, defined throughout this chapter, this leads to a cooperative process between plasmonic field and Raman emitter which can enhance the Raman response. This process is generally defined as *"dynamical back-action"* [44, 45].

Definition of the Coupling Factor

The coupling factor describes the entity of the interaction between the plasmon electromagnetic field and the vibrational mode. This interaction happens through the change in the polarizability of the Raman emitter itself, characteristic of a Raman process. The coupling factor has been derived either from the quantum-mechanical description of electric field and molecular vibration [45] or from the resonance frequency shift related to the medium polarizability inside the cavity [44]. For sake of generality, in this thesis a derivation from the energy conservation is given. The result perfectly coincides with that derived following the afore mentioned alternative treatments. The polarization of a Raman emitter in the presence of a local field is [7]: [1]

$$p = \frac{\alpha \cdot E}{V} \tag{5.1}$$

[1] differently from eq. (4.4), it is here needed to considered the local electric field, and therefore insert the volume on which the field is extended.

Correspondingly, the electromagnetic energy of the interaction between the electromagnetic field and the Raman emitter itself is:

$$U = -p \cdot E = -\alpha \frac{|E|^2}{V} \tag{5.2}$$

The polarizability is expressed in dependence on the vibrational coordinate as in eq. (4.1). As explained in Chapter 4, if the electromagnetic field oscillates at a frequency ω_0, in an inelastic scattering event this frequency can be changed in a Raman process by the change of the polarizability of the Raman emitter. As a very general consideration, the frequency can then be taken as a function of the vibrational coordinate, just as the polarizabity. [2] The energy can then be written as:

$$U = n_P \hbar \left[\omega_0 + x_v \frac{\partial \omega_0}{\partial x_v} \right] = - \left[\alpha + x_v \frac{\partial \alpha}{\partial x_v} \right] \frac{|E|^2}{V} \tag{5.3}$$

As in eq. (5.1), V is the volume on which the electric field is extended. Taken into consideration that the number of photons at a frequency ω_0 is equal to $n_P = \frac{\epsilon_0 V |E|^2}{\hbar \omega_0}$, one obtains the relation:

$$\frac{\partial \omega_0}{\partial x_v} = \frac{\omega_0}{\epsilon_0 V} \frac{\partial \alpha}{\partial x_v} \tag{5.4}$$

Based on this result, the analogy with a typical optomechanical system becomes clear (compare with Figure 5.1). In such a system a mirror coupled to a spring is subjected to a radiation force that mechanically shifts the mirror. The mechanical oscillation of the spring connected to the mirror is consequently excited. This oscillation is going to change the distance between the two mirrors, which will cause a change in the resonance frequency of the cavity. The vibrational coordinate x_v is the analogous of the degree of freedom of the spring. The resonance frequency can be expressed as a function of this degree of freedom, namely [60, 61]:

$$\omega_0(x_v) = \omega_{(x_v=0)} + x_v \frac{\partial \omega_0}{\partial x_v} \tag{5.5}$$

This expression for the frequency is exactly the same that has been used in eq. (5.3). The first partial derivative of the frequency after the mechanical degree of freedom is in optomechanics expressed as a parameter G_v. From eq. (5.5) follows then the definition:

$$G_v = -\frac{\partial \alpha}{\partial x_v} \frac{\omega_0}{\epsilon_0 V} \tag{5.6}$$

G_v is nothing but the coupling factor between the electromagnetic field and the vibrational mode. The interaction between them is mediated by the change in polarizability of the Raman emitter. The radiation force defined in eq. (4.3), can be expressed though the coupling factor G_v, as:

$$F = n_P \hbar G_v \tag{5.7}$$

The formulation that has been presented in this section has general validity for an electric field, which more precisely has been described up to now as an electric field inside a cavity, which looses or gains energy in favor of a vibrational mode. In the following sections, the electric field related to the plasmon is treated as the field inside a cavity, in the general description of a plasmon as a resonant system.

[2] This is equivalent to state, in a very general way, that besides the field oscillating at its characteristic frequency ω_0 (corresponding to the Rayleigh scattering field), another component exists, which oscillation frequency is modified by the molecular vibration (corresponding either to the Stokes or Anti-Stokes scattering).

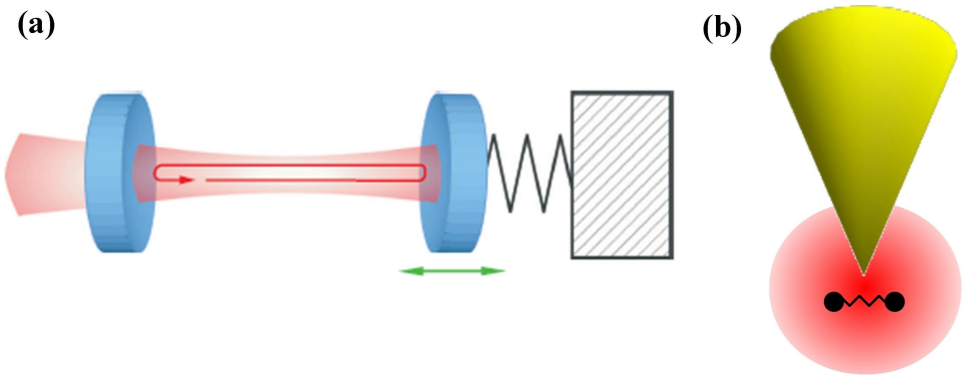

Figure 5.1: (a) schematic representation of an optomechanical system composed by a two-mirrors Fabry-Perot cavity where one mirror is mechanically coupled to a spring. (b) in analogy with the optomichanical system, the near-field related to a local plasmon can be pictured as a resonant system coupled to a vibrational mode characteristic, for instance, of a molecule. Compare with [61] and [45].

Hamiltonian for the coupled System and Derivation of the Quantum Langevin Equations

To considered the temporal dynamic of the system, it is necessary to formulate its corresponding Hamiltonian. The Hamiltonian as presented in this thesis, was first formulated in [62]. In the following, the local electric field oscillating in time is considered to be the one related to the plasmon. Its resonance frequency is then labeled correspondingly. In comparison with the notation used in the previous section, it holds: $\omega_0 \equiv \omega_P$. Considering the definition of the coupling factor and including the energy of the molecular vibration, the total energy of the system can be written as:

$$U = n_P \hbar \omega_P + n_v \hbar \omega_v + n_P \hbar x_v G_v \tag{5.8}$$

Where n_P and n_v are the photon and phonon population respectively. In a quantum-mechanical notation, this corresponds to the Hamiltonian:

$$\hat{H} = \hbar \omega_P \hat{a}^\dagger \hat{a} + \hbar \omega_v \hat{b}^\dagger \hat{b} + \hbar G_v \hat{x}_v \hat{a}^\dagger \hat{a} \tag{5.9}$$

$\hat{a}^\dagger$ and $\hat{a}$ represent the photon annihilation and creation operators respectively. Similarly $\hat{b}^\dagger$ and $\hat{b}$ represent the phonon operators. The Hamiltonian in eq. (5.9) describes two coupled harmonic oscillators. The last term is defined as the interaction Hamiltonian $\hat{H}_{int} = \hbar G_v \hat{x_v} \hat{a}^\dagger \hat{a}$. In the treated system one harmonic oscillator corresponds to the plasmon while the second corresponds to the Raman emitter. The operator for the vibrational coordinate $\hat{x_v}$ can be written for a harmonic oscillator through the creation and annihilation operators, according to $\hat{x_v} = x_{zpm}\left(\hat{b}^\dagger + \hat{b}\right)$. x_{zpm} is the amplitude of the zero point motion for a harmonic oscillator of effective mass m, oscillating at the frequency ω_v given by $x_{zpm} = \sqrt{\frac{\hbar}{2m\omega_v}}$. For sake of simplicity in the mathematical treatment, the coupling is usually expressed through:

$$g_v = x_{zpm} G_v \tag{5.10}$$

The factor g_v is generally named the *vacuum optomechanical coupling factor* [44]. From the above definitions, the total Hamiltonian is then written as:

$$\hat{H} = \hbar\omega_P \hat{a}^\dagger \hat{a} + \hbar\omega_v \hat{b}^\dagger \hat{b} + \hbar g_v \left(\hat{b}^\dagger + \hat{b}\right) \hat{a}^\dagger \hat{a} \tag{5.11}$$

It needs now to be considered that the system is overall driven by a laser source. In the total Hamiltonian we then need to include a term describing the laser, namely:

$$\hat{H}_L = i\hbar\sqrt{\kappa_{ex}} s \left(e^{-i\omega_L t}\hat{a}^\dagger - e^{i\omega_L t}\hat{a}\right) \tag{5.12}$$

The quantity $\kappa_{ex} s^2$ correspond to the photon flux. The total Hamiltonian is the sum of eq. (5.11) and (5.12). It is now convenient to change the reference system. By making use of the Backer-Campbell-Hausdorf formula, the total Hamiltonian can be written as:

$$\hat{H} = \hbar\left(\omega_P - \omega_L\right)\hat{a}^\dagger \hat{a} + \hbar\omega_v \hat{b}^\dagger \hat{b} - \hbar g_v \hat{a}^\dagger \hat{a}\left(\hat{b}^\dagger + \hat{b}\right) + i\hbar\sqrt{\kappa_{ex}} s \left(\hat{a}^\dagger + \hat{a}\right) \tag{5.13}$$

The difference between the laser and the plasmon frequency is expressed through: $\Delta = \omega_P - \omega_L$. Δ indicates the spectral displacement of the laser frequency from the plasmonic one and therefore it is referred to as the *detuning factor*. In the following the Hamiltonian as expressed in eq. (5.13) is used to describe the dynamics of the system. The time-dynamics of the operators is described through the Heisenberg equation motion. Taking into account the decay in time, the time derivatives of the photon and the phonon operators are:

$$\frac{\partial \hat{a}}{\partial t} = i\Delta\hat{a} + ig_v\hat{a}\left(\hat{b}^\dagger + \hat{b}\right) - \frac{\kappa}{2}\hat{a} + \sqrt{\kappa_{ex}} s \tag{5.14}$$

$$\frac{\partial \hat{b}}{\partial t} = -i\omega_v\hat{b} + ig_v\hat{a}^\dagger\hat{a} - \frac{\gamma_v}{2}\hat{b} \tag{5.15}$$

These are the Quantum Langevin Equation of the system. They are going to be used in the following sections to investigate the system dynamics. Before proceeding we note that eq. (5.15) can be written as the sum of two equations, one for the linear momentum $\hat{p_v}$ and one for the position operator $\hat{x_v}$. This follows from the definition for the phonon operator as: $\hat{b} = \sqrt{\frac{m\omega_v}{2\hbar}}\left[\hat{x_v} + i\frac{\hat{p_v}}{m\omega_v}\right]$. The two equations of the system corresponding to eq. (5.15) are then:

$$\frac{\partial \hat{p_v}}{\partial t} = -m\omega_v^2 - \frac{\gamma_v}{2}\hat{p_v}\hat{x_v} + \hbar G v \hat{a}^\dagger\hat{a} \tag{5.16}$$

$$\frac{\partial^2 \hat{x_v}}{\partial t^2} = -\omega_v^2\hat{x_v} - \frac{\gamma_v}{2}\frac{\partial \hat{x_v}}{\partial t} + \frac{\hbar G_v}{m}\hat{a}^\dagger\hat{a} \tag{5.17}$$

Solution in the Classical Limit

As a first approach one can look for a solution in the classical limit. The treatment is summarized in this section, further details can be found in [44]. The classical solution is derived by taking the expectation values for the operators. Eq. (5.17) becomes:

$$\frac{\partial^2 x_v}{\partial t^2} = -\omega_v^2 x_v - \frac{\gamma_v}{2}\frac{\partial x_v}{\partial t} + \frac{\hbar G_v}{m}|E|^2 \tag{5.18}$$

The last term in (5.18) is the equivalent of the radiation force as defined in eq. (4.3) and (5.7). The amplitude of the total field E appearing in the last term of eq. (5.18) is governed by the equation:

$$\frac{\partial E}{\partial t} = i\Delta E + i x_v G_v E - \frac{\kappa}{2}E + \sqrt{\kappa_{ex}}s \tag{5.19}$$

which corresponds to eq. (5.14) in the classical limit. In the following a solution for eq. (5.19) is sought. The vibrational amplitude can be supposed to be harmonic and correspondingly is considered to have to form $x_v(t) = x_0 cos(\omega_v t)$. It is further assumed that the amplitude of the vibration is much smaller that the length L on which the field is extended. The dimensionless parameter $\epsilon = \frac{x_0}{L}$ is then used to expand the field as: $E(\epsilon) = \sum_0^\infty E_n \epsilon^n$. The relevant solutions are those for the zero and first order, corresponding to:

$$E_0 = \frac{\sqrt{\kappa_{ex}}s}{\left[-i\Delta + \frac{\kappa}{2}\right]} \tag{5.20}$$

$$E_1(t) = E_{AS}e^{i\omega_v t} + E_S e^{-i\omega_v t} \tag{5.21}$$

The the amplitudes of the Anti-Stoked E_{AS} and Stokes E_S fields are given by:

$$E_{AS} = \frac{G_v L}{2}\frac{E_0}{\left[\omega_v - \Delta - i\frac{\kappa}{2}\right]} \tag{5.22}$$

$$E_S = -\frac{G_v L}{2}\frac{E_0}{\left[\omega_v + \Delta + i\frac{\kappa}{2}\right]} \tag{5.23}$$

The total field is then:

$$E(t) = E_0 + E_1(t) \tag{5.24}$$

This field can be inserted in eq. (5.18) to find a solution for the amplitude of the vibration. It is worth to note that, after the substitution of the expression for the electric field, eq. (5.18) becomes the classical equation for a harmonic oscillator driven by a radiation force, perfectly corresponding to the system described in Chapter 4. If the radiation force applied to the vibrational mode is set to be constant (compare with Chapter 4), this force should have in this case the form $F_P = \hbar G_v |E_0|^2$. Eq. (5.18) can be then rewritten as:

$$\frac{\partial^2 x_v}{\partial t^2} = -\tilde{\omega_v}^2 x_v - \frac{\tilde{\gamma_v}}{2}\frac{\partial x_v}{\partial t} + \frac{\hbar G_v}{m}|E_0|^2 \tag{5.25}$$

where $\tilde{\omega_v}$ and $\tilde{\gamma_v}$ are the effective resonance frequency and damping factor respectively, given by:

$$\tilde{\omega_v} = \sqrt{\omega_v^2 - \frac{\hbar G_v^2}{m}\frac{\kappa_{ex}s^2}{\left[\Delta^2 + \frac{\kappa^2}{4}\right]}\left\{\frac{\omega_v + \Delta}{\left[\Delta + \omega_v\right]^2 + \frac{\kappa^2}{4}} - \frac{\omega_v - \Delta}{\left[\Delta - \omega_v\right]^2 + \frac{\kappa^2}{4}}\right\}} \tag{5.26}$$

$$\tilde{\gamma_v} = \gamma_v + \frac{\hbar G_v^2}{m\omega_v} \frac{\kappa_{ex} s^2}{\left[\Delta^2 + \frac{\kappa^2}{4}\right]} \left\{ \frac{\frac{\kappa}{2}}{\left[\Delta - \omega_v\right]^2 + \frac{\kappa^2}{4}} - \frac{\frac{\kappa}{2}}{\left[\Delta + \omega_v\right]^2 + \frac{\kappa^2}{4}} \right\} \tag{5.27}$$

In the following the discussion focuses on the effective damping factor $\tilde{\gamma_v}$ and its behavior in dependence on the *detuning factor*. For *red-detuning* ($\omega_L < \omega_P$), the *detuning factor* is positive, which leads to an increase of the effective damping factor. This increase can be interpreted as a loss of energy for the vibrational mode in favor of the plasmonic field. The most interesting situation happens for the opposite case, that is the *blue-detuning* ($\omega_L > \omega_P$). In this case the *detuning factor* is negative, which leads to a decrease of the effective damping factor. Opposite to the previous case, the energy is now transferred from the plasmon to the vibrational mode. Consequently, the Raman signal can be strongly enhanced. According to the definition of this process as *dynamical back-action*, the effective damping factor is usually written as:

$$\tilde{\gamma_v} = \gamma_v + \gamma_v^{DBA} \tag{5.28}$$

The definition of γ^{DBA} follows from eq. 5.27. The best enhancement condition is present for $\Delta = \omega_v$, for which the effective damping factor is minimum. Interestingly, this condition is the same as that obtained in the previous chapter when considering a stimulated Raman process given by the sum of the laser and the plasmon field. The enhancement of the Raman signal can be considered through the out-of-equilibrium vibrational occupancy following from the *blue-detuning* [63]. In presence of *dynamical back-action* the phonon population is given by:

$$n_v^{DBA} = \frac{n_v}{1 - \frac{|\gamma_v^{DBA}|}{\gamma_v}} \tag{5.29}$$

n_v is the phonon population in absence of *dynamical back-action*. It is of interest for the discussion of the experimental results presented in the following chapters to focus on the Stokes-process. For this, the cross-section in presence of *dynamical back-action* is given by:

$$\sigma_S^{DBA} = \frac{n_v^{DBA} + 1}{n_v + 1} \sigma_S \tag{5.30}$$

σ_S is the Raman cross-section in the absence of *dynamical back-action*. The scattered Raman power in a Stokes process can be taken as: $P_S = \sigma_S^{DBA} P_L$. From eq. (5.30) follows that the Stokes power is given by the sum of a linear component, which corresponds to the Raman power in absence of *dynamical back-action*, and another component having though n_v^{DBA} a stronger dependence on the laser power. From eq. (5.30) and (5.29) it appears that the Raman power diverges for the condition:

$$\frac{|\gamma_v^{DBA}|}{\gamma_v} = 1 \tag{5.31}$$

If the photon flux is written as $\kappa_{ex} s^2 = \frac{P_L}{\hbar\omega_L}$, the asymptotic power can be found from eq. (5.31) to be:

$$P_{L,threshold} = \frac{\hbar\omega_L m \gamma_v \omega_v \left[\Delta^2 + \frac{\kappa^2}{4}\right]}{\hbar G_v^2} \frac{\left[(\Delta + \omega_v)^2 + \frac{\kappa^2}{4}\right] + \left[(\Delta - \omega_v)^2 + \frac{\kappa^2}{4}\right]}{2\kappa\Delta\omega_v} \tag{5.32}$$

As follows from eq. (5.32), the asymptotic power is diminished for a larger coupling factor. Also, it increases rapidly for higher plasmonic damping. It then not trivial to reach this regime, because the damping of common plasmonic nanostructure is very high ($\sim 10^{13}$Hz).

Quantum-Electrodynamic Solution of the Langevin Equation

In the following, the Quantum Langevin Equations presented in eq. (5.15) and (5.14) are solved without mapping them to their classical equivalent [45], as it was done in the previous section. Before doing so, it is helpful to define the plasmonic electric field as a quantized field with resonance frequency ω_P and an effective volume V expressed through the photon creation and annihilation operators:

$$E_P = i\sqrt{\frac{\hbar\omega_P}{2\epsilon V}}\left(\hat{a} - \hat{a^\dagger}\right) \tag{5.33}$$

The interaction Hamiltonian and the coupling factor can be found also from this quantum-mechanical definition of the field. [3] Again, it needs to be considered that the system is driven by a laser. In this treatment, this is done defining a *driving parameter* Ω, as:

$$\Omega = \frac{\kappa}{2}\sqrt{\frac{\epsilon_0 V}{2\hbar\omega_L}}|E| \tag{5.34}$$

In the presence of plasmonic enhancement, the amplitude of the field $|E|$ is that of the laser field multiplied by the field enhancement factor, $|E| = f|E_L|$. Correspondingly to (5.34), the driving term in the Hamiltonian is:

$$\hat{H}_L = i\hbar\Omega\left(\hat{a}^\dagger e^{-i\omega_L t} - \hat{a}e^{i\omega_L t}\right) \tag{5.35}$$

For consistency with eq. (5.12) this Hamiltonian has been labeled as $\hat{H_L}$. Nonetheless, there is a substantial difference between the two formulations. In eq. (5.12) the prefactor contains the photon flux and the excitation rate. It consists then purely of the laser excitation, not including any term relative to the plasmon or the associated near-field. The *driving paramenter* as defined in eq. (5.34) is related on the contrary to the plasmon electromagnetic field. Indeed it contains the plasmon decay rate, the effective volume and the field enhancement factor. The system is then considered in this last formulation to be excited not directly by an external electric field, such as that of the laser, but by the local plasmonic field.

According to the definition of the driving paramenter, the total Hamiltonian in eq. (5.13) becomes:

$$\hat{H} = \hbar\Delta\hat{a}^\dagger\hat{a} + \hbar\omega_v\hat{b}^\dagger\hat{b} - \hbar g_v\hat{a}\left(\hat{b}^\dagger + \hat{b}\right) + i\hbar\Omega\left(\hat{a}^\dagger - \hat{a}\right) \tag{5.36}$$

Correspondingly, the Quantum Langevin Equations are formulated like:

$$\frac{\partial\hat{a}}{\partial t} = i\Delta\hat{a} + ig_v\hat{a}\left(\hat{b}^\dagger + \hat{b}\right) - \frac{\kappa}{2}\hat{a} + \Omega \tag{5.37}$$

$$\frac{\partial\hat{b}}{\partial t} = -i\omega_v\hat{b} + ig_v\hat{a}^\dagger\hat{a} - \frac{\gamma_v}{2}\hat{b} \tag{5.38}$$

[3] The coupling factor g_v as defined in eq. (5.10) can be derived from this definition for the quantized electromagnetic field. The induced Raman dipole operator can be written as $\hat{p}_R = \hat{\alpha}\hat{E}$. The interaction Hamiltonian is correspondingly: $\hat{H}_{int} = -\hat{p}_R\hat{E} = -\hat{\alpha}\left|\hat{E}\right|^2$. The Raman polarizability is given by $\hat{\alpha} = \alpha + \frac{\partial\alpha}{\partial x_v}\hat{x_v}$, where $\hat{x_v} = x_{zpm}(\hat{b} + \hat{b^\dagger})$. Expressing the field as in eq 5.33, one finds $\hat{H}_{int} = -\left(\frac{\partial\alpha}{\partial x_v}\right)\frac{\hbar\omega_P}{\epsilon V}\hat{a^\dagger}\hat{a}x_{zpm}\left(\hat{b^\dagger} + \hat{b}\right)$. This Hamiltonian corresponds to eq. (5.11) after the definition $g_v = x_{zpm}\left(\frac{\partial\alpha}{\partial x_v}\right)\frac{\hbar\omega_P}{\epsilon V}$, equivalent to eq. (5.10).

These equations can be solved if it is assumed that the coupling between the two oscillators is weak enough to consider their interaction as a perturbation from the steady state. The steady state amplitude is: $\alpha_S = \frac{\Omega}{\left(\frac{\kappa}{2}+i\Delta\right)}$. By the substitution $\hat{a} = \alpha_S + \hat{a}$, the Quantum Langevin Equations become:

$$\frac{\partial \hat{a}}{\partial t} = i\Delta\hat{a} - \frac{\kappa}{2}\hat{a} + ig_v\alpha_S\left(\hat{b}^\dagger + \hat{b}\right) \tag{5.39}$$

$$\frac{\partial \hat{b}}{\partial t} = -i\omega_v\hat{b} - \frac{\gamma_v}{2}\hat{b} + ig_v\left(\hat{a}^\dagger\alpha_S + \alpha_S^*\hat{a} + |\alpha_S|^2\right) \tag{5.40}$$

The same equations can be correspondingly written also for $\hat{a}^\dagger$ and $\hat{b}^\dagger$. It is possible to find an analytical solution for the system of these four equation setting the detuning to zero and neglecting the thermal population of the vibrational mode. The system of equations can be written in matrix form as:

$$\frac{\partial}{\partial t}\vec{A} = \bar{\bar{M}}\vec{A} + \vec{D} \tag{5.41}$$

where

$$\vec{A} = \begin{bmatrix} \hat{a}^\dagger \\ \hat{a} \\ \hat{b}^\dagger \\ \hat{b} \end{bmatrix} \tag{5.42}$$

$$\bar{\bar{M}} = \begin{bmatrix} -\frac{\kappa}{2} & 0 & -ig_v\alpha_S^* & -ig_v\alpha_S^* \\ 0 & -\frac{\kappa}{2} & +ig_v\alpha_S & +ig_v\alpha_S \\ +ig_v\alpha_S & +ig_v\alpha_S^* & -\left[\frac{\gamma_v}{2} + i\omega_v\right] & 0 \\ -ig_v\alpha_S & -ig_v\alpha_S^* & 0 & -\left[\frac{\gamma_v}{2} - i\omega_v\right] \end{bmatrix} \tag{5.43}$$

$$\vec{D} = \begin{bmatrix} 0 \\ 0 \\ -ig_v|\alpha_S|^2 \\ +ig_v|\alpha_S|^2 \end{bmatrix} \tag{5.44}$$

The emission spectrum of the cavity can be calculated as:

$$S(\omega) = \omega^4 \int_{-\infty}^{+\infty} dt e^{-i\omega t}\langle\hat{a^\dagger}\rangle_{ss} \tag{5.45}$$

The suffix *ss* indicates the steady-state. From the Quantum Regression Theorem, the equation of motion for the quantity $\langle x(t)\rangle$ is the same as that for $\langle x(t)x(0)\rangle$. It is therefore useful to multiply eq. (5.41) with the vector:

$$\vec{A_0} = \begin{bmatrix} \hat{a_0} & \hat{a_0}^\dagger & \hat{b_0} & \hat{b_0}^\dagger \end{bmatrix} \tag{5.46}$$

Doing so, one finds that the two-time correlator $\langle\hat{a^\dagger}\hat{a_0}\rangle_{ss}$ needed to calculate the emission spectrum according to eq. (5.45) can be found from the product:

$$e^{t\bar{\bar{M}}}\langle \begin{bmatrix} \hat{a}^\dagger \\ \hat{a} \\ \hat{b}^\dagger \\ \hat{b} \end{bmatrix} \hat{a_0}\rangle_{ss} \tag{5.47}$$

This product can be expressed as a series of expressions with exponential factors given by the eigenvalues of $\bar{\bar{M}}$. Among those, the terms oscillating at frequencies $\pm\omega_v$ are taken, in order to describe the Stokes and Anti-Stokes scattering. In the experiments described in the following, the Stokes scattering is measured. For sake of simplicity the further discussion focuses on the results for the Stokes scattering. The emission spectrum at the Stokes frequency is then found to be:

$$S(\omega_S) = \frac{2\omega_S^4}{\gamma_v}\left(s_2\Omega^2 + s_4\Omega^4\right) \tag{5.48}$$

In the limit $\gamma_v << \kappa, \omega_v$, corresponding to the real condition, the factors s_2 and s_4 can be written as:

$$s_2 = \left(\frac{4g_v}{\kappa|\kappa - i2\omega_v|}\right)^2 \tag{5.49}$$

$$s_4 = s_2^2\frac{\kappa}{\gamma_v} \tag{5.50}$$

In this result the contribution of thermally excited vibrations is neglected, on the other hand it can be considered changing eq. (5.48) in:

$$S(\omega_S) = \frac{2\omega_S^4}{\gamma_v}\left[s_2\left(1+n_v\right)\Omega^2 + s_4\Omega^4\right] \tag{5.51}$$

where n_v corresponds to the Boltzmann occupation for the vibrational level. In analogy with the previous discussion, it is worth to evaluate the threshold for the incident power from which the non-linearity should appear. In this case we can take as threshold the power for which the quadratic term is larger than the linear one. For an estimation of the threshold it is convenient to use the *driving parameter*. One finds:

$$\Omega^2_{threshold} = \frac{\gamma_v}{\kappa}\left[\frac{\kappa^2\left[\kappa^2 + 4\omega^2\right]}{16g_v^2}\right] \tag{5.52}$$

corresponding to the electric field [4] :

$$|E|^2_{threshold} = \frac{\hbar\omega_P\gamma_v}{\kappa\epsilon_0 V}\left[\frac{\kappa^2 + 4\omega^2}{16g_v^2}\right] \tag{5.53}$$

As before, the threshold for the non-linear process decreases for a higher coupling factor and is increased for a higher plasmonic damping. The increase of the threshold power with the plasmon damping factor makes generally speaking the experimental observation of the non-linearity challenging. Indeed, for real plasmonic system, the plasmon damping is usually very high, between 10^{13} and 10^{14} Hz. In this sense, the plasmon is a "bad cavity" characterized by high losses. The high losses can on the other hand be compensated by the very small volume (on the nanometer scale) on which the local field is extended.

Unfortunately, no analytical solution exists for the general case in which the detuning is different

[4] remember $|E| = f\,|E_L|$ where f is the enhancement factor of the electric field.

for zero. Nonetheless it is fundamental to analyze the dynamic of the system also in dependence on the *detuning*. This can be done looking for a numerical solution of the equation:

$$\frac{\partial \rho}{\partial t} = i[\rho, \hat{H}] + \frac{\kappa}{2} D_{\hat{a}}[\rho] + \frac{\gamma_v (n_v + 1)}{2} D_{\hat{b}} + \frac{\gamma_v n_v}{2} D_{\hat{b}^\dagger} \tag{5.54}$$

where ρ is the density matrix of the system and, for a generic operator $\hat{o}$:

$$D_{\hat{o}}[\rho] = 2\hat{o}\rho\hat{o^\dagger} - \hat{o^\dagger}\hat{o}\rho - \rho\hat{o^\dagger}\hat{o} \tag{5.55}$$

It is beyond the aim of this thesis to explain the computational method needed to solve eq. (5.55). A detailed description of this can be found elsewhere [45]. For a comparison with the experimental work, the results related to the Stokes process are discussed. It turns out, that the emission intensity due to *dynamical back-action* changes in relation to the *detuning*. In particular the emission intensity is maximum when the laser frequency is higher than the plasmonic resonance frequency (*blue-detuning*). It is also interesting to compare the analytical results with the numerical ones. For a weaker coupling the results obtained with the two different methods are in good agreement. When the coupling becomes stronger, the analytical results slightly overestimate the intensity of the scattered field. The strength of the couping is considered through the ratio between the coupling factor and the plasmon damping factor, named the *"granularity parameter"* $\frac{g_v}{\kappa}$ [131].

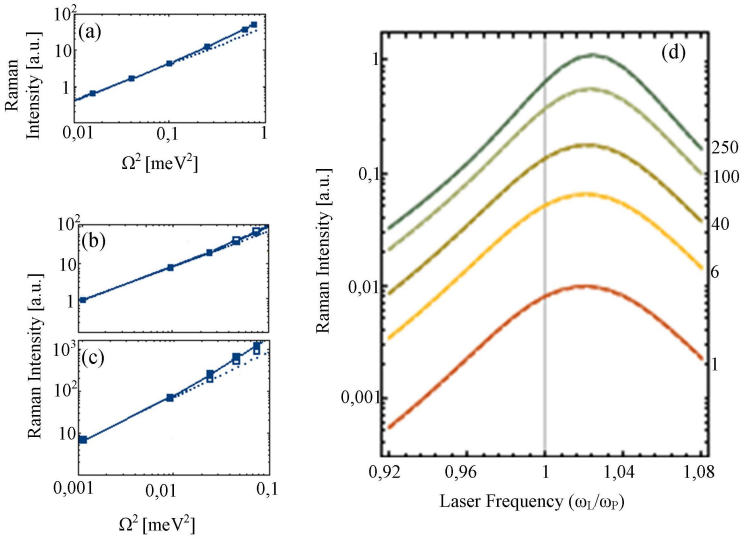

Figure 5.2: intensity of the Raman peak as a function of the square of the driving parameter for (a)$g_v = g_0$ (b) $g_v = 10g_0$ (c) $g_v = 30g_0$ (g_0 is set equal to $6 \cdot 10^{13}$Hz, the plasmon damping is taken to be 250 larger than g_0). The full squares are the results obtain though the linearised Hamiltonian, the empty ones are those obtained though the full numerical solution. The dashed line shows the linear trend. (d) intensity of the Raman peak as a function of the laser frequency (given in units of the plasmon resonance frequency). On the right axis the driving parameter corresponding to the shown curves is given in meV. The grey line correspond to the plasmon resonance frequency. Adapted from [45].

Solution within the Quantum Noise Approach

Besides the treatment which has just been described, based on the solution of the master equation, an alternative analysis is possible. This analysis is based on the *Quantum Noise Approach* [64, 65]. Within this approach, the rates of relaxation and excitation of the vibration are considered to be proportional to the noise spectrum of the cavity. In the coupled system under analysis, the photon population fluctuation is the analogous of the power spectrum of the cavity noise. Since the noise fluctuations are considered, it si convenient to formulate the Hamiltonian such that no driving term appears. This is possible defining the displacements:

$$\alpha'_S = \frac{\Omega}{\frac{\kappa}{2} + i\Delta'} \tag{5.56}$$

$$\beta'_S = \frac{g_v \left|\alpha'_S\right|^2}{\omega_m - i\frac{\gamma_m}{2}} \tag{5.57}$$

$$\Delta' = \Delta - 2g_v Re\left\{\beta'_S\right\} \tag{5.58}$$

The fluctuation of the plasmon population is estimated around its equilibrium value, defining $\hat{F}(t) = \hat{a^\dagger}\hat{a} - \left\langle \hat{a^\dagger}\hat{a} \right\rangle$. The cavity fluctuation can be simplified as $\hat{F} \approx \alpha'_S(\hat{a} + \hat{a^\dagger})$. In this way, the fluctuation around the steady-state value is obtained. The fluctuation in the time domain is then given by: [66]:

$$S(t) = \left\langle \hat{F}(t)\hat{F(0)} \right\rangle = \left|\alpha'_S\right|^2 e^{i\Delta' t - \frac{\kappa}{2}t} \tag{5.59}$$

From the fluctuations in the time domain, the noise spectrum follows as:

$$S(\omega) = \int_{-\infty}^{+\infty} e^{i\omega t} \left\langle \hat{F}(t)\hat{F}(0) \right\rangle dt = \left|\alpha'_S\right|^2 \frac{\kappa}{\left[\Delta' - \omega\right]^2 + \frac{\kappa^2}{4}} \tag{5.60}$$

The noise of the radiation pressure force is found from the power spectrum of the noise as:

$$S_{\hat{F}\hat{F}} = \hbar G_v S(\omega) \tag{5.61}$$

The optomechanical damping is defined from Fermi golden rule as:

$$\gamma_{opt} = \frac{x_{zpm}^2}{\hbar^2} \left[S_{\hat{F}\hat{F}}(\omega_m) - S_{\hat{F}\hat{F}}(-\omega_m)\right] \tag{5.62}$$

which finally gives:

$$\gamma_{opt} = g_v^2 \left|\alpha'_S\right|^2 \kappa \left\{ \frac{1}{(\Delta' - \omega_m)^2 + \frac{\kappa^4}{4}} - \frac{1}{(\Delta' + \omega_m)^2 + \frac{\kappa^2}{4}} \right\} \tag{5.63}$$

This formulation requires $\gamma_{opt}, \gamma_m << \kappa$ [66], these conditions are satisfied for the experimental system described in the following. In analogy with the photon population, also the phonon population fluctuation can be found through the power spectrum noise. The molecular vibration is in

a displaced thermal state, where the displacement is given by β'_S and the incoherent population of the thermal state is given by:

$$n_b^{incoherent} = \frac{\gamma_m}{\gamma_m + \gamma_{opt}} n^{thermal} + \frac{(\Delta' - \omega_m)^2 + \frac{\kappa^2}{4}}{4\Delta'\omega_m} \frac{\gamma_{opt}}{\gamma_m + \gamma_{opt}} \tag{5.64}$$

As a result, the intensity of the Stokes emission for an arbitrary detuning is given by [45]:

$$S(\omega_S) = \omega_S^4 \frac{g_v^2 \kappa \left|\alpha\right|^2}{(\Delta' + \omega_m)^2 + \frac{\kappa^2}{4}} \frac{n_b^{incoherent} + 1}{\gamma_{opt} + \gamma_m} \tag{5.65}$$

In Chapter 7, the experimental results will be interpreted using eq. (5.65).To estimate the scattered power spectrum the parameter Δ' needs to be calculated. It is then necessary to find an expression for the real part of β'_S. This can be done substituting eq. (5.56) into (5.57). This leads to the third order equation:

$$4g^2 \left[Re\left\{\beta'_S\right\}\right]^3 - 4\Delta g_v \left[Re\left\{\beta'_S\right\}\right]^2 + \left[\frac{\kappa^2}{4} + \Delta^4\right] \left[Re\left\{\beta'_S\right\}\right] - \frac{g_v \omega_m \Omega^2}{\omega_m^2 + \frac{\gamma_m^2}{4}} = 0 \tag{5.66}$$

For the realistic parameters of the system under analysis in this work, the real part of β'_S is however negligible compared to Δ. It can then be generally considered in the following $\Delta' = \Delta$.

The optomechanical damping γ_{opt} defined in eq. (5.63) is the analogous of the *dynamical back-action* damping (γ^{DBA}) derived in the previous section. In analogy with γ^{DBA}, γ_{opt} describes the energy flux from the molecular vibration to the cavity (first term) and from the cavity to the vibration (second term). For blue detuning ($\Delta < 0$) the optomechanical coupling is negative and the incoherent phonon population increases. The energy is then lost by the plasmon field and gained by the vibrational mode, leading to an enhancement of the Raman scattering. It must be noticed here that the second term is eq. (5.64) is not derived for the solution in the classical limit. The presence of this term makes the dependence of the Stokes emission $S(\omega_S)$ on the *detuning factor* and on the plasmon damping factor more complicated that it was found for the solution in the previous section. Following from this non trivial dependence, it is not strictly true, that the best enhancement condition for the Raman response is given by the matching between vibrational frequency and *detuning factor*, $\Delta = -\omega_v$. This point is further discussed in the following of this section.

As can be seen from eq. (5.65) the scattered power diverges for $\gamma_{opt} = -\gamma_m$. For the Raman scattering intensity to diverge it is then necessary that the optomechanical damping factor becomes negative. This is possible only in the case of *blue-detuning*, when the *detuning parameter* Δ is negative. In terms of the *pumping parameter* the divergence is found for the condition:

$$\Omega_{threshold}^2 = -\gamma_m \left[\frac{\Delta^2 + \frac{\kappa^2}{4}}{\kappa g_v^2}\right] \frac{\left[(\Delta - \omega_m)^2 + \frac{\kappa^2}{4}\right] \left[(\Delta + \omega_m)^2 + \frac{\kappa^2}{4}\right]}{4\Delta\omega_m} \tag{5.67}$$

giving for the electric field [5]:

$$|E|_{threshold}^2 = -\frac{8}{\kappa^2} \frac{\hbar\omega_P}{\epsilon V} \gamma_m \left[\frac{\Delta^2 + \frac{\kappa^2}{4}}{\kappa g_v^2}\right] \frac{\left[(\Delta - \omega_m)^2 + \frac{\kappa^2}{4}\right] \left[(\Delta + \omega_m)^2 + \frac{\kappa^2}{4}\right]}{4\Delta\omega_m} \tag{5.68}$$

[5] again, the field is expressed as $|E| = f\,|E_L|$ where f is the enhancement factor.

The minus sing in eq. (5.67) and (5.68) is compensated by the fact that Δ is negative. As already explained, if Δ is positive, the divergence cannot be reached and eq, (5.67) and (5.68) are not valid anyways. For *zero-detuning* ($\Delta = 0$) the optomechanical damping factor as defined in eq. (5.63) vanishes. In this limit, the incoherent population becomes:

$$\lim_{\Delta=0} n_b^{incoherent} = n_b^{th} \frac{\kappa}{\gamma_m} \frac{4g_v}{\kappa^2 + 4\omega_m} |\alpha_S|^2 \tag{5.69}$$

From the comparison with eq. (5.49), valid in the limit $\gamma_m << \omega_m, \kappa$, eq. (5.69) is equal to:

$$\lim_{\Delta=0} n_b^{incoherent} = n_b^{thermal} + s_2 \Omega^2 \frac{\kappa}{\gamma_m} \tag{5.70}$$

The two analytical results are then fully consistent: the expression for the scattered Raman intensity found in the *zero-detuning* case, is a limit of the expression found through the *Quantum Noise Approach*.

As already mentioned, the dependence of $S(\omega_S)$ on the plasmon damping factor and on the *detuning factor* is not as easy as it was found according to the solution in the classical limit. The behavior of $S(\omega_S)$ is therefore investigated in the following for different *detuning* conditions and for different values of the plasmon damping. The description is focused on the Stokes Raman scattering for comparison with the experiment presented in Chapter 7. For small plasmon damping ($\kappa \sim 10^{11}$ Hz) the best condition for the enhancement of the Raman scattering is found as for the solution in the classical limit for $\Delta = -\omega_m$. In this case, the *detuning* plays indeed an extremely critical role, changing the Raman response about orders of magnitude. This can be understood by inspection of eq. from (5.63) to (5.65): for the condition $\kappa << \Delta, \omega_m$ the denominators in eq. (5.63) are dominated by the difference $\Delta - \omega_m$. In the case of *blue-detuning*, γ_{opt} can assume very large negative values, and can consequently lead to a large increase of the incoherent vibrational population $n_b^{incoherent}$ (below threshold, before the Raman signal diverges, the optomechanical damping factor is always smaller than the vibrational damping factor, $\gamma_{opt} < \gamma_v$). Also, for small plasmonic damping, the prefactor in eq. (5.65) is larger. This situation is represented in Figure 5.4. Note that, besides the strong dependence on the detuning factor, also in the best enhancement condition the Raman response due to the *dynamical back-action* is always linear.

In the real case, the plasmon damping is on the other hand of the same order of magnitude of the *detuning factor* and the vibrational frequency, that is $\kappa \sim \Delta \sim \omega_m \sim 10^{13}$ Hz. In such a situation the difference $(\Delta - \omega_m)$ is less crucial, because the plasmonic damping factor becomes more relevant at the denominator in eq. (5.63). The Raman scattering intensity changes in this case less critically together with the *detuning factor*. Remarkably, when the plasmonic damping factor becomes comparable with the *detuning factor*, the best *detuning* condition for the Raman enhancement changes compared to the previous case. The signal enhancement is in this case not maximum when the difference between the *detuning factor* and the vibrational frequency is zero, as it is found for smaller damping factors, but the best condition for the signal enhancement is found for $\Delta \approx 0,6\omega_m$ assuming for instance $\kappa = 7 \cdot 10^{13}$Hz (see Figure 5.5 and caption for further details). As explained before, this is due to a more complicated dependence of $S(\omega_S)$ on the *detuning factor* and the plasmonic damping, than it is found for the solution in the classical limit. It should also be noticed that for higher plasmonic damping factor, and having all others parameters unchanged compared to the previous example, the response due to the *dynamical back-action* deviates from

linearity. This is because of the increase of the *driving parameter* Ω with the plasmonic damping factor (see eq. 5.34). Anyhow, the palsmonic damping factor appears as already pointed out, also at the denominator of the expression for the Stokes emission intensty $S(\omega_s)$ and the optomechamical damping γ_{opt} (eq. 5.63 and 5.65). For this reason, $S(\omega_S)$ cannot increase arbitrarily with the plasmon damping factor. In Figure 5.5 the Raman scattering intensity is calculated for different values of the plasmonic damping factor κ. Consistently with the previous explanation, a behavior at maximum is found: the Raman scattering intensity first increases with the plasmonic damping factor but the decreases when it is further increased (see Figure 5.5 and caption for further details).

A big advantage of eq. (5.65) is that it can be used for arbitrary *detuning*. In Figure 5.6 the Raman intensity in dependence on the laser power is calculated for a positive Δ. In this case the dependence on the power becomes weaker. This is because, in consistence with the previous description, some energy is lost from the vibrational mode to the cavity, which leads to a decrease of the phonon population and consequently to a decrease of the scattered intensity. Interestingly, for high plasmon damping factor, deviation from the linearity is present also for small positive *detuning factor*. The signal then decreases for higher positive *detuning factors* Δ as explained before.

Before concluding, it should be pointed out that this description (regardless if the solution is found in the classical limit or if it is purely quantum-mechanical), the polarizability α has been considered to be independent on the frequency. This approximation is valid for non-resonant Raman. In Chapter 7, the theoretical prediction presented here is compared with experimental results on graphene. Strictly speaking, Raman scattering in solids is a resonant process, in the sense that it involves real electronic levels, as explained in Chapter 1. This point is further taken into account when comparing the experimental results with the theoretical prediction.

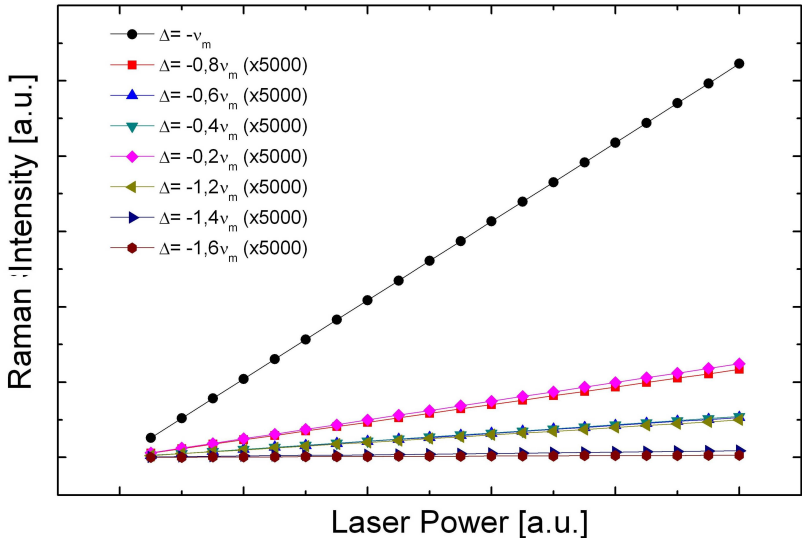

Figure 5.3: Raman Scattering Intensity as a function of the laser power calculated for different detuning condition and for $\kappa = 10^{11}$ Hz. For the condition $\Delta = -\omega_m$ the intensity of the Raman scattering is maximum and roughly three orders of magnitude higher than for other detuning condition. The vibrational frequency is that of the graphene G band, $\omega_m = 4.71 \cdot 10^{13}$ Hz.

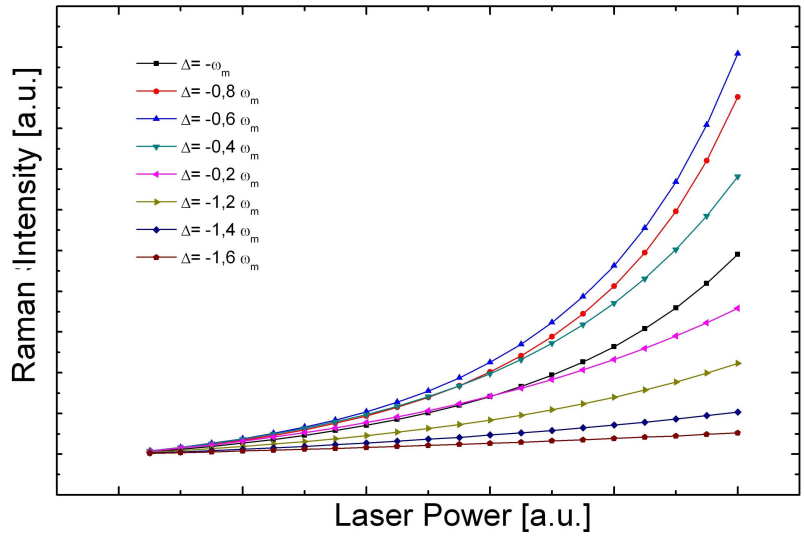

Figure 5.4: Raman scattering intensity calculated according to eq. (5.65) as a function of the laser power calculated for different detuning condition and for $\kappa = 7 \cdot 10^{13}$ Hz. All other parameters are the same as in Figure 5.3. The increase of the plasmon damping factor leads to the non-linearity through the increase of the *driving parameter* Ω. Also a larger plasmon damping factor modifies the best condition for the detuning, which is found in this case to be $\Delta \approx -0,6\omega_m$.

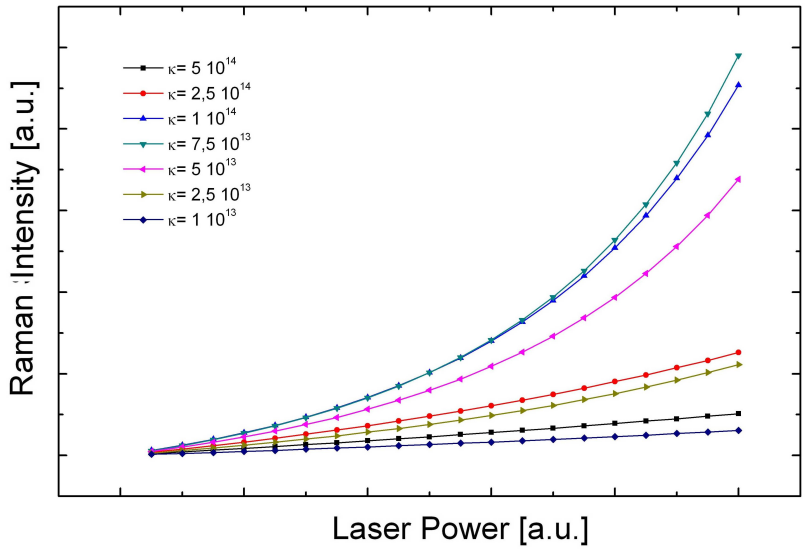

Figure 5.5: Raman scattering intensity as a function of the laser power calculated according to eq. (5.65) for different plasmon damping factors. The Raman scattering intensity has a maximum behavior in dependence on the plasmon damping factor (see text for explanation).

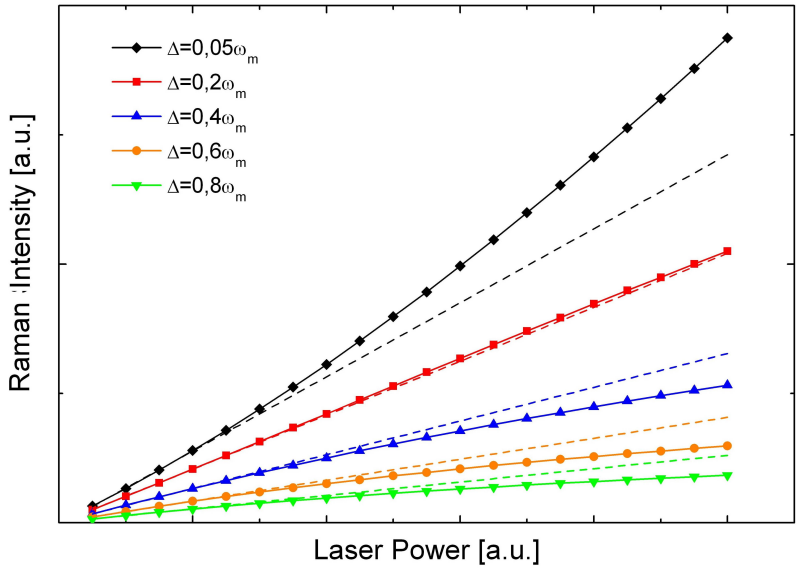

Figure 5.6: Raman scattering intensity calculated according to eq. (5.65)as a function of the laser power for different positive *detuning factor*. The *detuning factor* Δ is given in units of the vibrational frequency ω_v. Besides the *detuning factor*, all parameters are the same as in Figure 5.4 and 5.3. The dashed lines are a guide for the eye. Interestingly, an enhancement of the signal is still present also for small positive detuning.

Chapter 6

Materials and Methods

In this chapter, the synthesis of the materials used throughout this work and the relative sample preparation are described. Also, the methods used for their characterization are presented.

Graphene

CVD-grown graphene samples on glass were fabricated by **Jürgen Krauss** of **Prof. S. Günther**'s group (TU Munich, Germany). For graphene growth, ca. $1\,cm^2$ pieces were cut from as received Cu-foil ($25\,\mu m$, Alfa Aesar 46986, 99.8%) and loaded into a quartz tube reactor. After evacuating the reactor system to $\sim 10^{-3}$ mbar the Cu-foils were heated up from room temperature to 950°C in a hydrogen flow ($p(H_2)$=1 mbar) within 40 min. For oxidative carbon removal the Cu-foil was exposed to a highly diluted oxygen flow in argon carriers gas $p(O_2)=1.105\cdot10^{-3}$ mbar in p(Ar)=1 mbar. After 60 min the temperature was increased to 1075 °C and the gas flow was changed, to ($p(H_2)$=20 mbar, $p(CH_4)$=0.02 mbar)with addition of CH_4 to start the graphene growth, followed by a 2.5 h growth period. Graphene growth was stopped by quickly pulling the Cu-foils out of the hot zone of the reactor. For the transfer of the as grown graphene films the Cu-samples were spincoated with Polymethilmethacrylate (PMMA) solution (6 wt.% in Anisole). After drying the PMMA-protected graphene film was released from the Cu-support by bubbling transfer. This was done by gradually dipping the PMMA-graphene-Cu sandwich vertically into NaOH-solution (7 g/L) with a platinum counterelectrode. During this dipping a current of 20 mA is applied with the Cu-sample as cathode. The detached graphene PMMA film is cleaned with deionized water and then transfered onto glass substrates. Finally the PMMA protection layer is removed with hot acetone.

Carbon Nanotubes

Besides Graphene, also single-walled carbon nanotubes (SWCNT) are used in this thesis as Raman emitter. The structure of a SWCNT can be conceptualized by wrapping the single layer of graphene called graphene into a seamless cylinder. The way the graphene sheet is wrapped is represented by a pair of indices (n,m). The integers n and m denote the number of unit vectors along two directions in the honeycomb crystal lattice of graphene. If m = 0, the nanotubes are called zigzag nanotubes, and if n = m, the nanotubes are called armchair nanotubes. Otherwise, they are called chiral. The

SWCNT raw material, used for this work, was fabricated by the chemical vapor deposition (CVD) method involving a cobalt-molybdenum catalyst (CoMoCat). Thereby, CoMoCat SWCNTs are enriched with the (6,5) chirality but also contain smaller fractions of (6,4), (8,3) and (9,1) chiralities. Before the SWCNTs can be deposited on the glass substrate, the raw material needs to be dispersed. Because of its hydrophobic nature, SWCNTs are not soluble in aqueous solutions. In addition, strong van-der-Waals forces between the SWCNT's unpolar sidewalls lead to the clustering of SWCNTs. Single dispersed SWCNT can be obtained through a treatment with surfactants (surface active agents) and sonication in an aqueous solution. During the dispersion process the surfactant molecules enclose the SWCNT in a micelle structure. Thereby their hydrophobic hydrocarbon chain is oriented towards the SWCNT, while their hydrophilic head group associates with the aqueous solute. Sonication leads to the crushing of SWCNT agglomerates into smaller bundles and isolated SWCNTs. The aqueous solution containing the SWCNT can be deposited on glass substrate by spin-coating or drop-casting. One always has to keep in mind that the surfactant is deposited on the glass surface together with the SWCNT. This can lead to an inhomogeneity of the photoluminescence or Raman signal along the SWCNT itself in a TERS measurement [27]. In the last decades the optical and structural properties of SWCNT have been widely investigated and discussed, further information can be found in literature [8, 9, 21].

Gold Nanorods

Gold nanorods were synthesized in the group of **Prof. Sebastian Mackowski** with the contribution of **Dr. Dawid Piatkowski** (Nikolaus Copernikus University, Torun, Poland), where also the absorbance spectra in water have been measured. For the synthesis of the precursor, $HAuCl_4$ (25 mL, 0.05 M), Cetyltrimethylammonium bromide (CTAB) solution (4.7 mL, 0.1 M) and $NaBH_4$ (0.3 mL, 0.01 M) are stirred for 3 min. $NaBH_4$ thereby acts as a reduction agent for $HauCl_4$ while CTAB stabilizes the resulting Au seeds as a ligand in solution. Slightly different synthesis conditions (temperature, surfactant concentration) allows to tune the aspect ratio of the rods. In this way, two kinds of nanorods have been prepared, having different aspect ratios and correspondingly different resonances in the visible range. The nanorods are deposited on the glass substrate on top of the graphene though drop casting. Doing so, both the rods and the CTAB are present on the sample surface. The nanorods were characterized though transmission electron microscopy (TEM) operated by **Dr. Sophia Betzler** and **Dr. Andreas Winset** at the Chemistry Department of the LMU Munich. The statistical analysis on the aspect ratio and length distribution was done by **Dr. Harald Budde** and **Dr. Richard Ciesielski** at the Chemistry Department of the LMU Munich. The dark field measurements were performed by **Francesca Nicoli** from **Prof. Tim Liedl** group at the Physic Faculty of the LMU Munich.

The discussion is first focused on the "long nanorods", having aspect ratio around 3. They present one plasmonic resonance in the green ($\sim$ 540 nm) and one in the near-infrared ($\sim$ 770 nm), see also Figure 6.1. The two resonances correspond to the electron density oscillation on the direction of the two different axis, as explained in Chapter 3. These two resonances can be observed from the absorption spectrum (Figure 5.6a). The dimension of the rods has been investigated through TEM. The length of the rods is not homogeneous, but a certain length distribution is present. Also, a fraction of very short nanorods (aspect ratio between 1 and 1.5) is present as subproduct from the synthesis (see Figure 6.2). The presence of this subproduct can explain the broadness of the absorption peak in the green part of the spectrum presented in Figure 5.6a: small aspect ratio

nanorods are indeed expected to have the resonance related to the long axis close to that related to the short one. On the other hand, the width of the absorption peak in the near-infrared region, related to the electron density oscillation on the long axis, reflects the length distribution of the long axis itself. The absorption spectrum presented in Figure 5.6a was measured in water after the preparation of the nanorods.

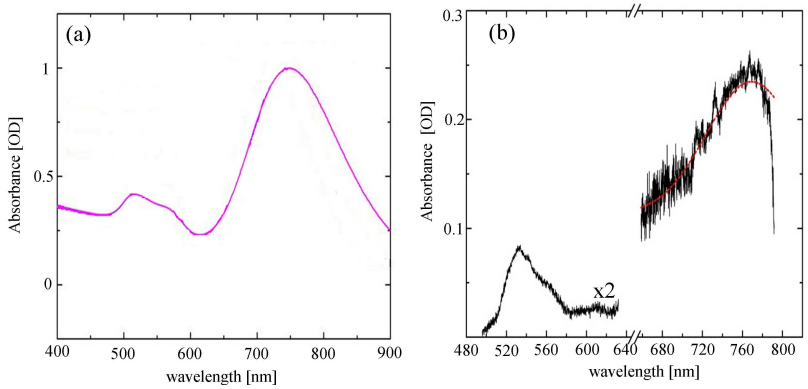

	ω_P (Hz)	λ_P (nm)	κ (Hz)
Green Resonance	$5.55 \cdot 10^{14}$	540	$3.70 \cdot 10^{13}$
Infrared Resonance	$3.893 \cdot 10^{14}$	770	$5.7839 \cdot 10^{13}$

Figure 6.1: (a) absorbance spectrum of the 3 aspect ratio nanorods in water solution; (b) absorption spectrum measured with with light after deposition on the glass substrate, having a single layer graphene on top. The resonance in the green region is multiplied by two for better comparison. In the table the plasmonic parameters extracted from the white light spectrum are shown: ω_P is the plasmonic resonance frequency (given also as a wavelength, labeled as λ_P) and κ is the plasmon damping factor. The red line shows the fitting curve for the infrared resonance, from which the plasmon parameters are extracted. At 800 nm the spectrum is cut by the laser filter (see Chapter 2).

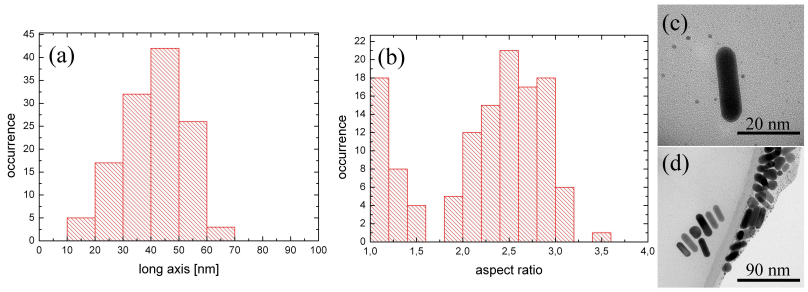

Figure 6.2: TEM analysis of the "long nanorods". (a) long axis length distribution; (b) aspect ratio distribution; (c) and (d) TEM images of representative nanorods. In (d) some small aspect ratio particles are observed; they are a subproduct of the chemical synthesis also appearing in (b).

As appears from eq. (3.1), the position of the plasmonic resonance depends on the refractive index of the surrounding medium. Ideally the nanorods are always surrounded by a single layer of CTAB. Such a single layer should be very thin, around 1-2 nm. The near-field related to the plasmon extends in space also beyond the CTAB single layer and the resonance frequency should then be dependent also on the refrective index of the external environment. Once the rods are deposited on glass, the external medium is composed partly by glass and partly by air. The effective reflective index might then change enough to sensibly shift the plasmonic resonance, with respect to that measured in water solution. Moreover, the plasmonic resonance can change drastically in the case of nanorods aggregation, because of coupling effects between plasmonic nanostructures. A precise determination of the plasmonic parameters, such as plasmonic resonance frequency and plasmonic damping factor is fundamental for a correct comparison between theory and experimental results. For these reasons, the plasmonic resonance needs to be estimated directly on the sample, in order to reveal any possible difference between the plasmonic parameters in dependence on the different environmental conditions.

In the case of the sample prepared with the long nanorods, the plasmonic resonance has been estimated with white light produced sending a broad-band laser pulse though a fiber (see Chapter 2). The spectrum has been measured first on a sample position where no gold nanorods where located, and then on a position where the nanorods are present. The nanorods are located on the sample through confocal scans (see Chapter 2). The spectrum given by the nanorods absorption is found as [128]:

$$S = \frac{I - I_{background}}{I_{background}} \tag{6.1}$$

where I is the spectrum measured where the nanorods are present, and $I_{background}$ is the spectrum measured at a position where no nanorods had been located. It should be pointed out that, in this case, spectra measured on different position on the sample where gold nanorods had been located, gave the same spectral response. A typical spectrum is shown in Figure 6.1b. This spectrum resembles the one obtained in water solution. The peak in the green region has a maximum around 530 nm, where the resonance related to the short axis polarizability is expected. Also a shoulder on the red side of the peak is present. This shoulder can be attributed to the nanorods present as subproduct of the chemical synthesis. The main peak due to plasmon resonance related to the long axis is centered around 770 nm, slightly shifted from that in water solution where the maximum is around 750 nm. The plasmon resonance frequency and the plasmon damping factor are extracted from this spectrum, and are used in the following of this thesis to compare the experimental results with theory. Even if the two measurements are performed in very different experimental conditions, for the same refractive index of the surrounding medium the two spectra should be the same. Indeed, also in the case in which the spectrum is measured on glass, a particle much smaller than the excitation wavelength should not render a pure scattering response, but its spectrum is dominated by the extinction properties of the particle [128]. In Figure 6.3, numerical method calculations for nanorods are presented, where both extinction and scattering cross section have been simulated for different surrounding media. The spectrum of the plasmonic resonance should change drastically changing the effective refractive index, as can be seen from Figure 6.3. The effective refractive index must then be very similar for the measurement in water and on the glass slide. This could not be the case, if a single nanorod surrounded by a single layer of CTAB would lay on glass. On the other hand, the refractive index of CTAB (~ 1.4) is similar to that of glass. One possibility is then that the nanorods are embedded in a thicker layer of CTAB. This could also explain the small shift ob-

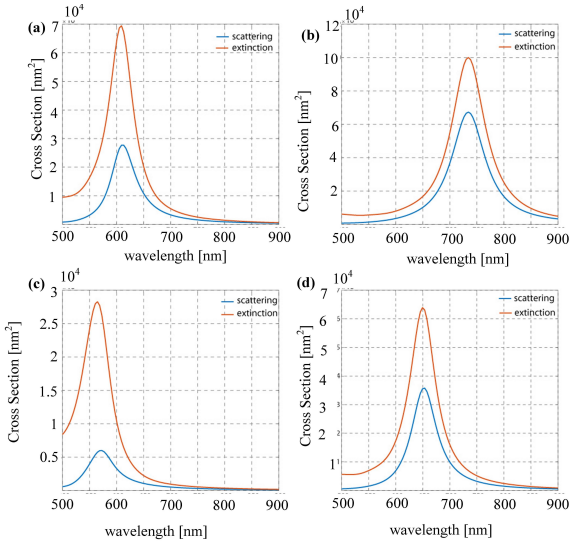

Figure 6.3: Extinction and scattering cross section simulation for 3 gold aspect ratio nanorods in air (a) and water (b). Extinction and scattering cross section simulation for 2 gold aspect ratio nanorods in air (c) and water (d). The simulation was carried out according to [68, 69, 70] with the help of **Dr. Alberto Comin**, Chemistry Department of LMU Munich.

served for the resonance curve measured with white light. If the nanorods are embedded is CTAB, it is hard to imagine that the nanorods can be single. Further hints that the deposited nanorods are not single, are given by the shape of the absorption spectrum. First, a shoulder appears, similar to that observed in the absorbance spectrum in water, which can correspondingly be attributed to the small aspect ratio nanorods. Second, and more importantly, the scattering spectrum does not change when measured on different sample positions. If the nanorods were single, every nanorod would give a slightly different spectrum, in dependence on its length. For all this reasons, it can be concluded that the nanorods are not isolated on the sample, but at every position a sufficiently high number of rods is present, to allow for the statistic ensemble measurement in water solution to be reproduced. On the other hand, the resonance appears always to be that of an ensemble of single separated nanorods. No change in the resonance which could be attributed to the coupling between two nanorods has been observed. This means that even if clustered, the nanorods are separated enough for every nanorod to behave as a single one. This is likely given by the presence of CTAB, which acts as a spacer between the nanorods. Concerning the plamonic properties then, it is still fair to treat every nanorod as single and consider only the coupling between each nanorod and graphene, in the framework described in Chapter 5.

The "short nanorods" have aspect ratio around 2. The abosorption spectrum in water shows two resonances in the visible range, the first is around 530 nm (the rods have the same diameter as the long ones, only the aspect ratio is different) and the second around 630 nm. As before, the absorption spectrum was measured in water (Figure 6.6) and the distribution of the dimension is analyzed though TEM. From the absorption spectrum, both plasmonic resonances are observable.

Also, no satellite peak appears. Correspondingly, no subproduct from the chemical synthesis is found in the TEM analysis. For this sample, it was possible to perform a dark field microscope analysis. The dark field images revealed a very inhomogeneous distribution of the nanorods on the sample surface, which are extremely concentrated at some positions on the sample while totally absent in others. Nonetheless the sample position where the nanorods concentration is reasonably good to perform a measurement, are easily recognizable both at the dark field and the confocal microscope (see Figure 6.7). Concerning this sample, two observation are important to be made. First, the plasmonic resonance measured for different sample positions is different. The sum of all the measured spectra gives a curve having very similar width compared to that of the peak measured in absorbance (see Figure 6.5). Second, compared to the spectrum measured in water, the maximum of the plasmonic resonance is shifted (see Figure 6.5 and 6.6 for further details). This means that the plasmon experiences an effective refractive index which is significantly smaller that that of water. This fact fits good to the picture described before, in which a single nanorod surrounded by a single layer of CTAB lays on the glass surface. Following from both observations, it is fair to assume that is this case the nanorods under observation are possibly single. It should also be pointed out, that in this case, the resonance in the green region of the spectrum was not observed for any of the nanorods, although it is well observable in the absorption spectrum. This resonance is weaker than the one in the red region of the spectrum. If the measured rods are single, it is likely that the scattering due to this plasmonic resonance is too weak to be detected.

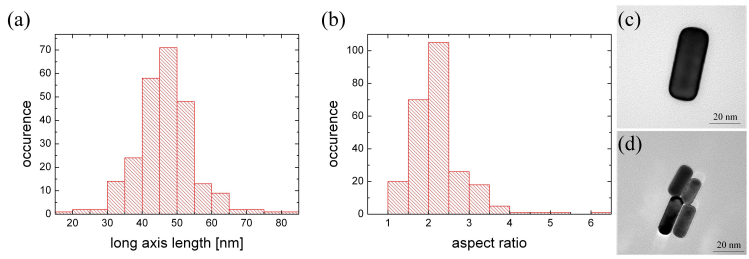

Figure 6.4: TEM analysis of the "short nanorods". (a) long axis length distribution; (b) aspect ratio distribution; (c) and (d) TEM images of representative nanorods.

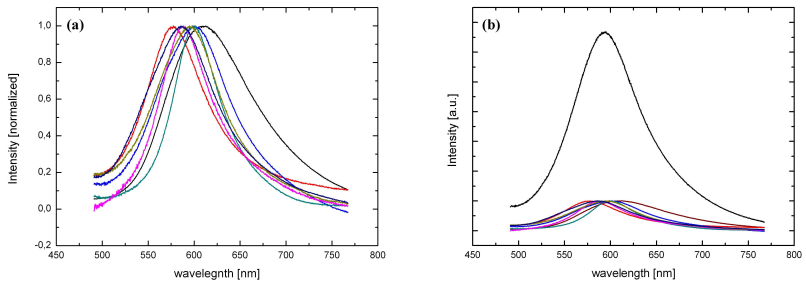

Figure 6.5: Dark field analysis of the "short nanorods". (a) resonance spectra measured for different positions on the sample; (b) sum of all the spectra. The resulting curve is centered at ~ 594nm and is $\sim 8 \cdot 10^{13}$Hz broad.

Although the presence a single rod removes the uncertainty about the number of hot-spots which are being observed within the same measurement, a difficulty rises, related to the inhomogeneity of the palsmonic resonance. Indeed, there is unfortunately no easy way to find the same sample position on the two different setups. When measuring the power dependence then, it is difficult to guess which are the exact plasmonic properties of the nanorod under observation. This point is further discussed in the next chapter.

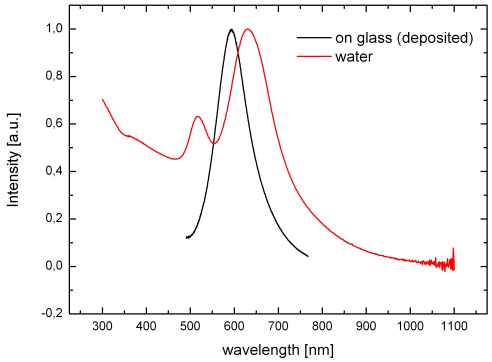

ω_P (Hz)	$5,04 \cdot 10^{14}$
λ_P (nm)	594
κ (Hz)	$8 \cdot 10^{13}$

Figure 6.6: comparison of the spectrum of the plasmon resonance in water (red line) and after the deposition of the nanorods on the graphene sample on glass substrate (black line). The main resonance appearing in the spectrum in water is centered at 630 nm and has a width of $\sim 10^{14}$ Hz. The black curve is the same as in Fugure 6.3, obtained by the sum of the plasmonic resonances measured at different positions. It shows a width of $\sim 8 \cdot 10^{13}$ Hz. In the table the plasmonic parameters extracted from the sum of different resonances measured at the dark field microscope (black line in the figure): ω_P is the plasmonic resonance frequency (given also as a wavelength, labeled as λ_P) and κ is the plasmon damping factor.

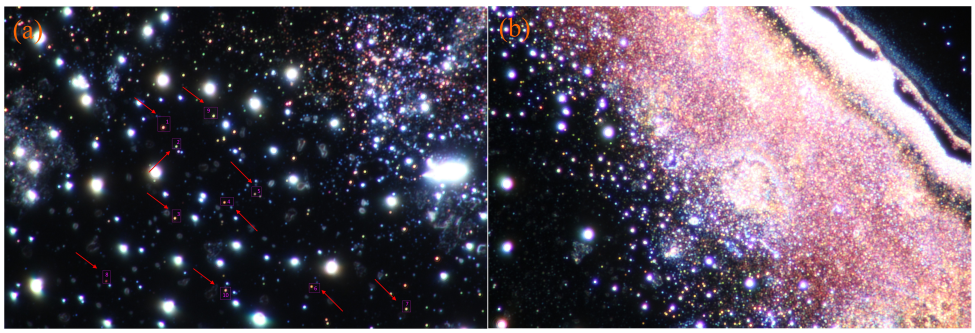

Figure 6.7: Dark-field image of a large area on the sample. The colored points correspond to nanorods, the white ones are residual CTAB crystals or PMMA. In panel (a) the positions are labeled, where the spectra have been measured. In (b) a region is shown where a high density of rods is present, probably corresponding to the edge of the drop.

Chapter 7

Results and Discussion

In this chapter the experimental results are presented and compared with the theory developed in Chapter 4 and 5. First, the results obtained with a Tip Enhanced Raman Spectroscopy (TERS) experiment are presented: in this experiment, the Raman response in dependence on the laser power was measured for single-walled carbon nanotubes and graphene deposited on glass, in the presence and in the absence of a gold nanotip. Second, the Raman response of graphene on a glass substrate measured in the presence of gold nanorods deposited on top, is presented. Both kinds of nanorods described in Chapter 6 are used, in order to investigate how the Raman response depends on the plasmonic properties of the nanostructure.

Tip Assisted Measurements

Carbon Nanotubes

The first experiment presented in this thesis has been performed on single-walled carbon nanotubes (labeled in the following simply as CNT) deposited on a glass substrate by drop casting. The Raman response in dependence on the laser power is measured in the presence and in the absence of a gold nanotip. The aim of the experiment is to detect the Raman signal stemming from the near-field volume and investigate its dependence on the laser power. For this experiment, a 633 nm laser is used for excitation; correspondingly the G and 2D band will appear at 703 and 760 nm respectively (compare with Chapter 1).

As a first experimental approach, the Raman signal is detected on an Avalanche Photodiode (APD) with appropriate filtering, while a gold nanotip and laser focus are scanned on the sample (see Chapter 2). Despite the light filtering, also the confocal signal and the background from the laser and from the inelastic scattering coming from the gold nanotip, are inevitably detected. As already pointed out in Chapter 2, this measurement has the advantage that also the topography of the surface is obtained. From the correlation between topography and optically detected signal, and extracting the near-field peak from the spatial profile of the optical image [67], it is possible to distinguish the near-field signal from the confocal signal and the background. To investigate the power dependence, the scans are repeated for different powers. For every scan the near-field signal is extracted from the spatial profile as explained before. The Raman near-field signal can in this

way be plotted in dependence on the laser power.

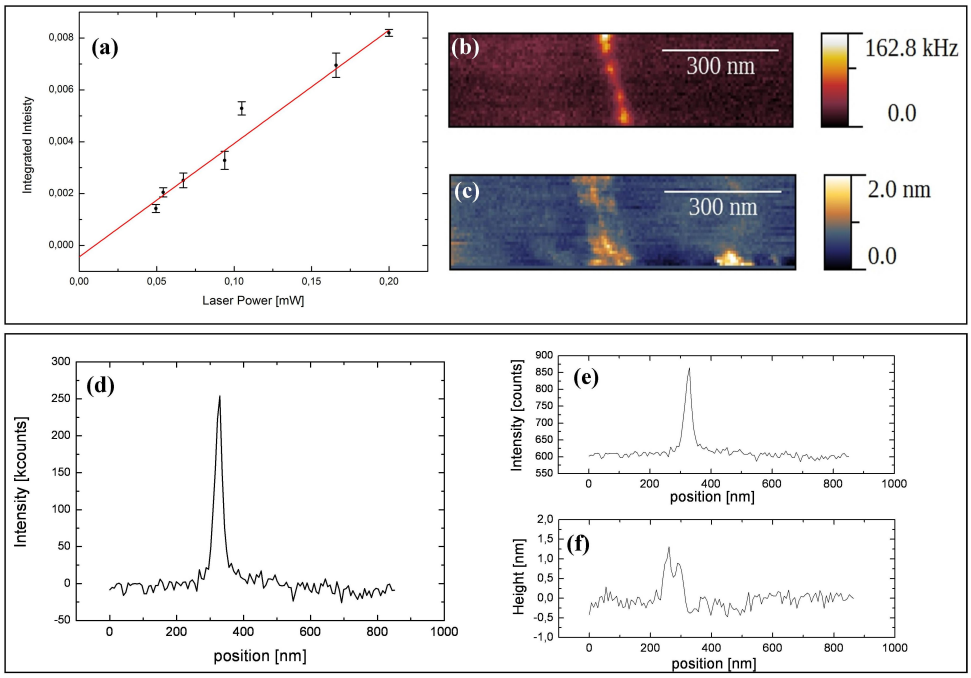

Figure 7.1: (a) power dependence of the Raman response; the signal is integrated under the near-field peak taken by the spatial profiles as that shown in (d), after repeating the scan for different laser powers. The average is taken over the different profiles coming from the same scan. (b) near-field optical and (c) topography image. In (d) the spatial profile of the near-field signal is shown after backgorund subtraction. The intensity is calculated as the integral under this kind of profiles. In (e) the special profile of the near-field signal before background subtraction is shown; the background contains the inelastic scattering backgrouns coming from the nanotip and the confocal background. In (f) a spacial profile of the topography is shown. In this measurement the G band signal was detected at 703 nm with appropriate laser filtering, under 633 nm laser excitation.

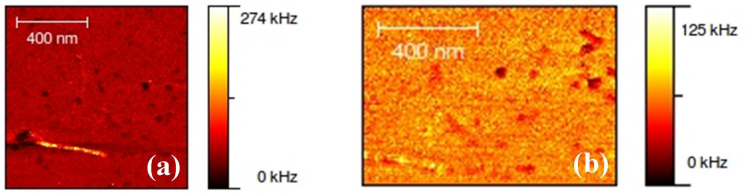

Figure 7.2: Two scans with the nanotip measured consecutively. The 633 nm laser is used for excitation. The G band scattering is detected at 703 nm with appropriate filtering. In the fist (a) the laser power is set at 1 mW, in the second (b) at 2 mW. At the second scan, the CNT signal is almost completely lost.

This plot is shown in Figure 7.1. Every point of the power series corresponds to the mean value of ca. 15 profiles extracted from one scan performed with a certain laser intensity. The Raman signal in dependence on the laser power shows here a linear trend. As can be noticed from Figure 7.1, the laser power was in the measurement considerably attenuated. It is necessary in this experiment to explore the widest possible power range, in order to possibly reach the incident intensity needed to observe a non-linear increase. It is challenging, in this experimental configuration, to come close to the full power of the laser, because of photo-bleaching of the CNT. The measurement in this experimental configuration is very long, because the scanning speed needs to be slow when measuring with the nanotip and the nanotip and laser need to be scanned on the CNT repetitively for several times. The overall amount of power deposited on the single CNT is then considerably high. The bleaching of the CNTs then occurs before high intensities can possibly be reached. The occurrence of bleaching is shown in Figure 7.2.

An alternative experimental configuration, consists of measuring the signal having landed the nanotip, without scanning the nanotip itself. Avoiding scanning, considerably reduces the time needed to perform the measurement. It allows then to reach a higher power regime, making the photobleaching less critical. On the other hand, without scanning, the information about the spatial distribution of the signal is lost. It is then impossible to distinguish the signal from the background, when detecting with the APD. This difficulty can be overcome detecting the signal with the spectrometer instead of with the APD. From the spectrum, the Raman peak can be distinguished from the background. Also, using the spectrometer, within the same measurement both Raman bands of the CNTs can be detected. Nonetheless, it is impossible from the spectrum to discriminate between the near-field and the confocal signal. When analyzing the trend of the Raman signal then, a linear contribution coming from the confocal volume always needs to be taken into consideration. The results obtained in this configuration are presented in Figure 7.3. A deviation from the linear behavior appears in this case for both the G and 2D band. A control experiment at the same position made in the absence of the nanotip, gives a linear trend as expected for spontaneous Raman scattering. It can therefore be concluded that the non-linearity is effectively given by the presence of the nanotip and the related localized plasmon. This measurements then show, that it is effectively possible to observe in the Raman response a deviation from the linear behavior in presence of a localized plasmon. It should also be pointed out here, that this experiment is not performed in the presence of a nano-cavity as that reported in literature [30], but in presence of a localized plasmon only.

On the other hand, even if a deviation from linearity appears, the trend of the Raman response is not fully clear in this measurement. A difficulty related to this experimental configuration and to the absence of the topographic information, is that the position of the tip with respect to the CNT is not determinable. During the experiment, the nanotip probably drifts and the tip-sample distance changes. This is what very likely makes the trend so unclear. Generally speaking, the increase in the signal could simply be given by the approaching of the tip to the CNT. This scenario is nonetheless unlikely, because the centering of the tip is optimized before starting the measurement. But in principle, being the centering procedure anyhow not perfect, nothing prevents the tip to come even closer to the sample after the measurement has been stared. As explained in Chapter 2, the drifting happens most likely for the xy-piezo of the AFM head. The tip-sample distance is indeed controlled in the z-direction because the feedback-loop is switched on during all the measurement. On the contrary, being the topographic signature absent in this case, there is no possibility to control the

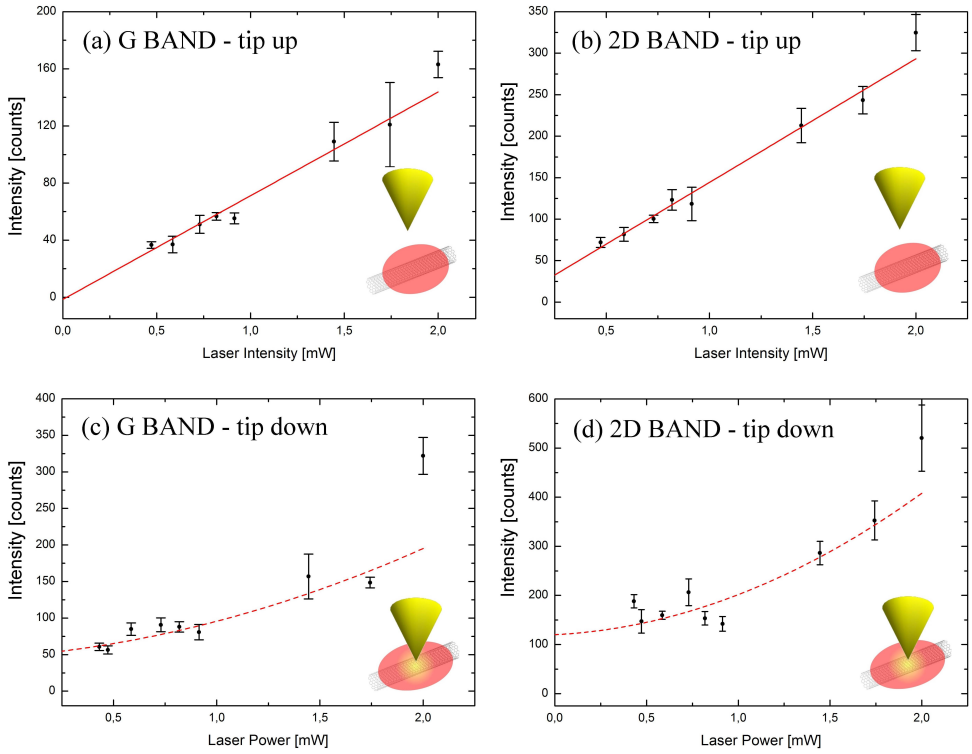

Figure 7.3: Power dependent Raman response for a single CNT in the absence of the nanotip for the G (a) and 2D (b) band, and for a single CNT in the presence of the nanotip for the G (c) and 2D (d) band. The red line in (a) and (b) is a linear fit through the experimental points, the red dashed line in (c) and (d) is a guide to the eye (the experimental points are hard to fit unambiguously). The presence of a single CNT is verified through a scan similar to that presented in Figure 7.1.

tip position in the x-y direction. For this reason, the tip-sample distance is likely to change only within the sample plane, but not in the normal direction. In this sense, the drifting is critical for a zero- or one-dimensional sample, but it would be less critical for an extended two-dimensional one: as long as the tip is inside the laser focus (which is realistic within the time needed for the measurement even in presence of drifting), there will always be a "hot-spot" delivering a near-field signal. In this perspective, it is convenient to switch to a two-dimensional sample, like graphene.

Graphene

Graphene is a two-dimensional material. In this sense, it would not render a characteristic topographic signature in an AFM scan. Such a sample is then suited for the second experimental configuration of the two used in the experiment on CNT, described in the previous section. The same measurements as described for the second CNT experiment are then performed also on single-layer graphene deposited on glass (see Chapter 6 for the sample preparation). Again, a 633 nm laser is used for excitation. The G and 2D band appear then at 703 and 760 nm respectively. For comparison with the measurement performed with nanordods presented in the following section, a spectrum recorded after landing the nanotip on the sample and one having retracted the nanotip are presented in Figure 7.4. When the tip is landed, the typical inelastic scattering background related to metallic nanostructures appears [58].

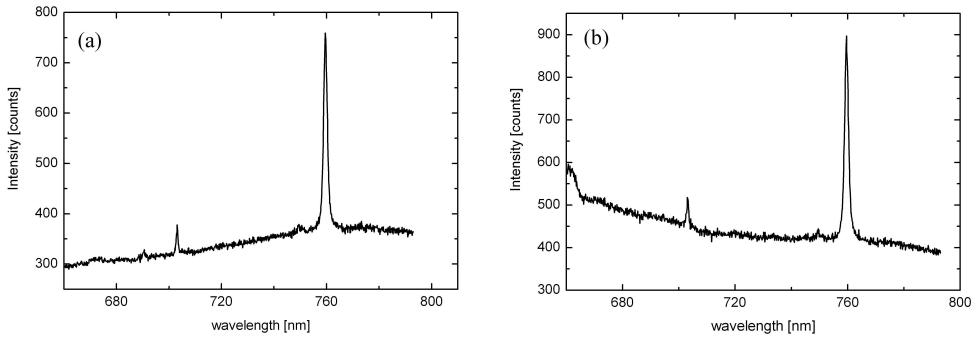

Figure 7.4: graphene spectrum recorded with tip retracted (a) and tip landed (b). When the nanotip is landed, the inelastic scattering background from the nanotip is present.

	vibrational frequency ω_v	vibrational damping factor γ_v
G BAND	$4.71 \cdot 10^{13}$ Hz	$5.4814 \cdot 10^{11}$ Hz
2D BAND	$7.91 \cdot 10^{13}$ Hz	$9.9245 \cdot 10^{11}$ Hz

Table 7.1: Vibrational frequency and damping factor for the G and 2D band of graphene, estimated from confocal spectra.

The power series recorded in the presence and in the absence of the nanotip are shown in Figure 7.5. For every spectrum the background is subtracted and the intensity is taken as the integral underneath the Raman peak (the intensity measured in counts is integrated on the wavelength interval corresponding to the Raman peak). For every laser power, 10 spectra are measured. Every point of a power series as that shown in Figure 7.5 corresponds to the mean value of the intensity obtained averaging the values coming from the 10 spectra measured with the same laser power.

In this experiment, in the presence of the nanotip a deviation from linearity can clearly be observed for the G band. The deviation from the linearity is very weak but not totally absent also for the 2D band (see Figure 7.5 and Figure 7.6 for further details). As expected from the discussion in

Chapter 4, in the absence of the nanotip the Raman response is linear with the laser power. Like in the experiment with the CNT, it can be seen that the non-linearity is given by the presence of a nanotip and the related localized plasmon. As pointed out for the experiment on the CNTs, this measurement is not done using a nano-cavity as reported in the literature [30] but in the presence of a single plasmonic nanostructure (the nanotip), giving a weaker field enhancement compared to the nano-cavity. A big advantage of the nanotip measurement is that exactly the same position can be measured in the presence and in the absence of the nanotip. This allows to use the trend of the Raman signal in dependence on the laser power obtained from the confocal measurement, for the quantitative evaluation of the near-field measurements. As explained for the CNTs experiment, the spectrum measured in the presence of the nanotip contains both the near-field and the confocal signal, which cannot be spectrally resolved. Compared to the situation of the CNT, the confocal signal is even stronger for graphene, which is an extended material. For the evaluation of the near-field signal, the confocal signal needs, in principle, to be subtracted. The advantage of the measurement with the tip consists then of the fact, that the confocal signal measured previously at the same position, can be assumed to be of the same entity of the confocal signal measured in the near-field measurement. Unfortunately the number of points experimentally obtained is not sufficient to directly subtract the confocal experimental points from the near-field ones.
The points obtained by this direct subtraction simply show no trend. On the other hand, one can include in the fit for the near-field measurement the linear function extrapolated for the trend of the confocal measurement. Doing so, the confocal background can be equivalently taken into account. In the following, the experimental data are compared with the different models presented in Chapter 4 and 5. The comparison between theory and experiment must always take the linear confocal background into account.

In literature [30] the power dependence of the Raman response has been investigated for single molecules or for CNT, generally speaking not for two-dimensional extended samples. For this reason, the experimental data have been fit with a power function without taking into account the confocal background which was, in those cases, absent or negligible. In this work, for fitting the experimental data, a power function must be summed to a line, to consider the signal coming from the extended two-dimensional material. The following formula is used for fitting the experimental data:

$$S_{Raman}(P_L) = A + B \cdot P_L + C \cdot P_L^N \tag{7.1}$$

The signal is labeled as $S_{Raman}(P_L)$, where P_L is the laser power. The slope (B) in eq. (7.1) is a fixed parameter taken from the linear fit, obtained from the confocal power series measurement. The results from this fit are presented in Figure 7.7. In general, the error on the exponent of the power function is very high, probably due to the small number of points deviating from the linearity. Anyhow, the exponent of the power function appears to be higher than two. In a stimulated Raman picture like that described in Chapter 4, an exponent of three could be explained following from the fact that the plasmonic field is linearly proportional to the laser field, as explained in Chapter 4. Besides the uncertainty about the exponent of the power function, in this picture is hard to explain the origin of the stimulating field, as already pointed out in Chapter 4.

For these reasons, the experimental data are compared with the quantum-electrodynamic (QED) description developed though Chapter 5. In particular, the comparison is made with the result obtained for the *Quantum Noise Approach*, which allows for an analysis for arbitrary detuning. A general difficulty related to the interpretation of the results with the nanotip according to this

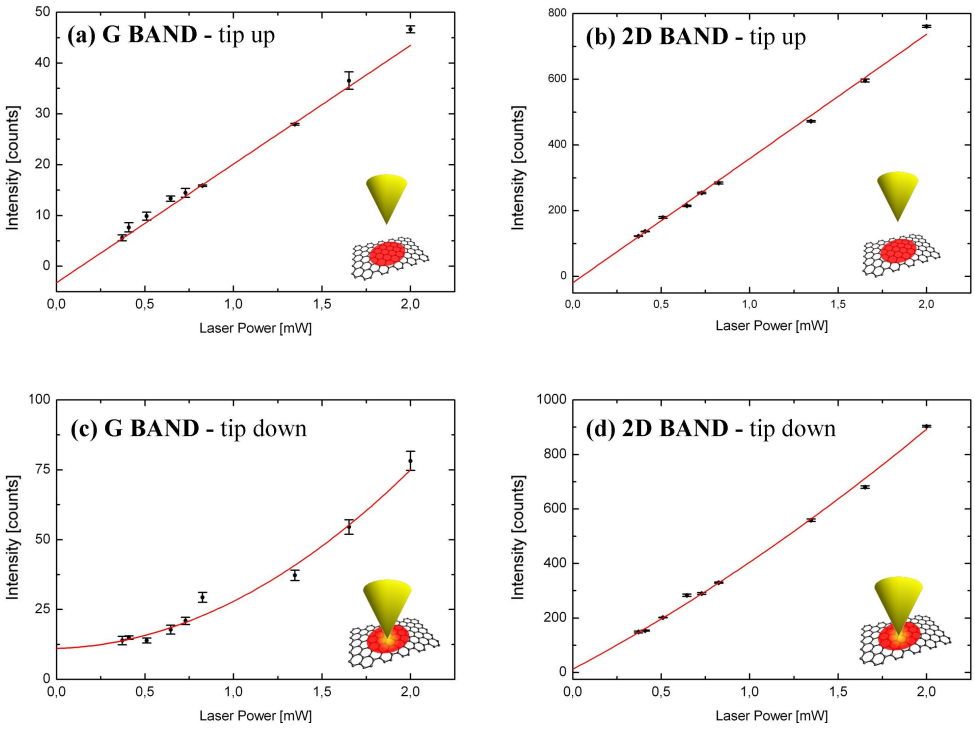

CONFOCAL	G band	2D band
intercept	$-3,2 \pm 0,8$	-18 ± 4
slope	$23,4 \pm 0,7$	377 ± 9
NEAR-FIELD	G band	2D band
intercept	11 ± 4	12 ± 20
linear coefficient	2 ± 20	345 ± 47
quadratic coefficient	15 ± 6	47 ± 20

Figure 7.5: **FIRST NANOTIP: LINEAR-QUADRATIC FIT.** Power dependent Raman response for graphene only on glass substrate for the G (a) and 2D (b) band, and for graphene in the presence of the nanotip for the G (c) and 2D (d) band. The red line in (a) and (b) is a linear fit through the experimental points, the red line in (c) and (d) is a fit with a linear and quadratic contribution. The fit parameters are presented in the table. For a correct background subtraction the intercept should be zero within the experimental error. The intensity is obtained as the integral under the Raman peak in the spectrum and is here given in counts (see Chapter 2).

model, is that the plasmonic parameters of the nanotip are unknown. In general, the resonance of the tip is spectrally broad in the visible range [48], possibly extending also to the infrared. As discussed in Chapter 5, a correct estimation of the plasmonic parameters is crucial, because the occurrence of the non-linearity depends not only on the plasmon resonance frequency, but also

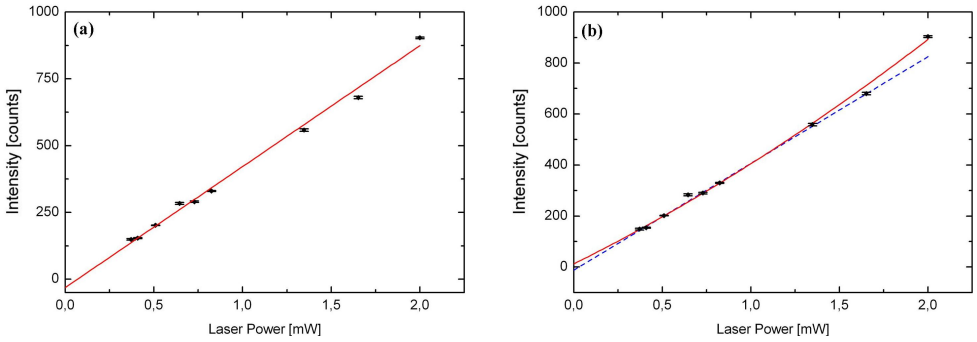

Figure 7.6: Comparison between a linear and a linear-quadratic fit for the 2D band of graphene in presence of the nanotip. The fitting parameters for the quadratic fit are the same as those presented in Figure 7.5. For the linear fit, the intercept and the slope are -31 ± 9 and 453 ± 12, respectively. Note, that the fitting line should have zero intercept within the experimental error. This is verified if the background has been subtracted correctly. Between the two fits, the quadratic one is slightly better, a zero intercept within the experimental error. The blue dashed line is a linear fit though the first five points, to show the deviation from the linear trend.

on the plasmonic damping. Nonetheless a comparison between the experimental results and the theoretical prediction is given in the following, trying to make a reasonable guess for the plasmonic parameters.
As noted before, the experimentally measured intensity contains two contributions, resulting one from near-field the and the other from the confocal signal (the near-field is in the following considered to stem from the *dynamical back-action*). Because eq. (5.65) does not provide a quantitative prediction of the signal intensity, the relative weight of the two contributions cannot be predicted as well. For this reason a weighting coefficient (C) is introduced in eq. (7.2), in order to scale the *dynamical back-action* response to the confocal one (which weight is given by the slope B). The trend of the Raman response in dependence on the laser power, is then simulated with the formula:

$$S_{Raman}(P_L) = A + B \cdot P_L + C \cdot S(\omega_S, P_L) \tag{7.2}$$

P_L is the laser power, $S(\omega_S, P_L)$ is the emission intensity as defined in eq. (5.65), which depends on the laser power P_L though the *driving coefficient* Ω. As before, the parameter B is the slope determined from the linear fit for the confocal measurement. C is the weighting coefficient to be determined. For simplicity in determining the weighting coefficient, the constants in eq. (5.65) are dropped, and the noise spectrum intensity is taken as: $S(\omega_S, P_L) \sim \frac{n_b^{incoherent}}{\gamma_{opt}+\gamma_m}$. Consistently with the previous discussion, the plasmonic resonance frequency of the nanotip is set to be around 780 nm. Considering that the laser wavelength is at 633 nm, the resulting detuning factor is $\Delta = -8.9254 \cdot 10^{13}$ Hz. The plasmonic damping factor is taken to be $2,5 \cdot 10^{14}$ Hz. The near-field volume is usually taken as half a sphere having the nanotip radius, estimated to be 10 nm [67]. The field enhancement factor, contained in the optomechanical damping γ_{opt} and the incoherent phonon population $n_b^{incoherent}$, through the driving parameter Ω (see eq. 5.34 5.63 and 5.64) is left as free parameter.

The simulation is made first for the G band. For the estimation of the coupling factor g_v, it is

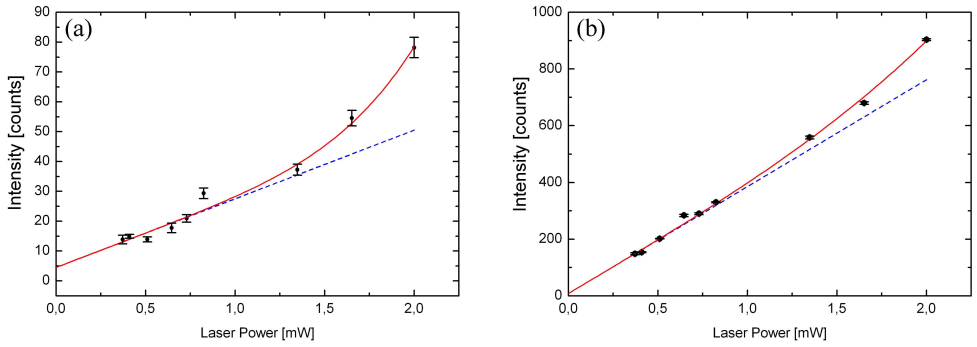

	G band	2D band
intercept (A)	$4,5 \pm 0,8$	8 ± 5
slope (fixed, B)	$23,4$	377
power coefficient (C)	1 ± 1	13 ± 9
exponent (N)	5 ± 2	3 ± 1

Figure 7.7: **FIRST NANOTIP: POWER FUNCTION.** Experimental data for the G (a) and 2D band (b) fit through eq. (7.1). The fitting parameters are presented in the table, the letters in parenthesis correspond to the variables as defined in 7.1. The slope is taken as fixed parameter and set according to that obtained for the fit of the data from the confocal measurement (compare with Table 7.5).

necessary to know the value of the polarizability change $\frac{\partial \alpha}{\partial x_v}$. In literature [10], it is referred to this quantity as the absolute value for the Raman tensor, consistently with eq. (1.5). On the other hand, the two definitions are equivalent, as it can be seen from eq. (1.4). For consistency with the terminology used in Chapter 4 and 5, the quantity $\frac{\partial \alpha}{\partial x_v}$ is used in the following discussion, and named polarizability change. For the G band, the value for the polarizability change has recently be estimated to be $\left(\frac{\partial \alpha}{\partial x_v}\right) = 92\,\text{Å}^2$ [10]. [1] It is important to note, that this value has been obtained per unit cell and normalized by the phonon effective mass (taken as the carbon mass for simplicity), which then needs to be considered explicitly. In this way, the *coupling factor* g_v is calculated to be, for a single unit cell, $g_v = 3.9842 \cdot 10^{10}\,\text{Hz}$. From the simulation of the experimental data, a weighting factor of $2.5 \cdot 10^{14}$ and an enhancement factor of 6.8 are found. This value for the field enhancement factor is absolutely reasonable for the experimental configuration used in this experiment [67, 48]. The absolute value of the Raman tensor for the 2D band, has not been experimentally determined in the literature. For an estimate of entity of the *dynamical back-action* for G band Raman vibrational mode with respect to the 2D band, the polarizability change of the 2D band is calculated here from that of the G band. From eq. (4.2), the ratio between the Stokes

[1] The absolute value of the Raman tensor in A^2 can be converted to its value in SI units, according to $\left(\frac{\partial \alpha}{\partial x_v}\right)[SI] = 4\pi\epsilon_0 \cdot 10^{-20}\left(\frac{\partial \alpha}{\partial x_v}\right)[\mathring{A}^2]$.

scattering fields corresponding to the G and the 2D bands is:

$$\frac{E(\omega_G)}{E(\omega_{2D})} = \frac{\omega_G^2}{\omega_{2D}^2} \frac{x_{v,G}\left(\frac{\partial\alpha}{\partial x_v}\right)_G}{x_{v,2D}\left(\frac{\partial\alpha}{\partial x_v}\right)_{2D}} \tag{7.3}$$

The vibrational amplitude can be taken to be the *zero-point motion* amplitude as before. Doing so eq. (7.3) becomes:

$$\frac{E(\omega_G)}{E(\omega_{2D})} = \frac{\omega_G^{3/2}}{\omega_{2D}^{3/2}} \frac{\left(\frac{\partial\alpha}{\partial x_v}\right)_G}{\left(\frac{\partial\alpha}{\partial x_v}\right)_{2D}} \tag{7.4}$$

Using the ratio of the field intensities, instead of the ratio between the field amplitudes, one finds:

$$\left(\frac{\partial\alpha}{\partial x_v}\right)_{2D} = \left(\frac{\partial\alpha}{\partial x_v}\right)_G \sqrt{\frac{\omega_G^3}{\omega_{2D}^3}\frac{I_{2D}}{I_G}} \tag{7.5}$$

From the confocal spectra, similar to that shown in Figure 7.4, a ratio of 3.8 is obtained between the intensities of the 2D and G band. In this estimation, the detection efficiency at 703 and 760 nm has been considered (see Chapater 2). Using for the ratio between the 2D and G band intensities the value of 3.8, one finds from eq. (7.5) $\left(\frac{\partial\alpha}{\partial x_v}\right)_{2D} = 2.105\left(\frac{\partial\alpha}{\partial x_v}\right)_G$. The coupling factor for the 2D band is correspondingly calculated to be, $g_v = 6.7391 \cdot 10^{10}$ Hz. For the trend of the experimental data of the 2D band, a field enhancement factor of 6.3 is found. In principle this value should be the same as that found for the G band (6.8), since this enhancement factor is that of the incident field. Nonetheless, considering the limited amount of points in the power series, the values are consistent with each other within the experimental uncertainty. To correctly simulate the experimental data, the weighting coefficient needs for the 2D band to be set to $3.5 \cdot 10^{14}$. The ration between the weighting coefficient for the G and the 2D band is 0.78. This value is very similar to the ratio between the detection sensitivity at the two respective wavelengths 0.81 (see Chapter 2).

In the following it is commented on the weaker deviation from the linearity, which is observed for the 2D band in comparison with the G band. In Figure 7.8 the intensity stemming from the *dynamical back-action* estimated for the two Raman bands, is shown. The curves presented in Figure 7.8 consist of the last term in eq. (7.2), weighted for the coefficient C used to reproduce the spectra (see Figure 7.5). As it can be seen, the intensity related to the 2D band is stronger than that related to the G band. However, because the confocal signal of the 2D band is substantially stronger as well, the resulting deviation from the linear trend is much smaller that that of the G band. A quantitative comparison is given in the table in Figure 7.9: here the signal intensity due to the *dynamical back-action* is calculated in percentage to the total detected signal for different values of the laser power. For the 2D band, besides for the highest laser power, the signal percentage due to the *dynamical back-action* is below 10%. For this reason, it is experimentally hard to observe a deviation from the linearity. For the G band, already for lower powers, the signal percentage due to *dynamical back-action* is sensibly higher (from around 10 up to 34 %). A deviation from the linear trend is for this reason experimentally easier to see for the G band than for the 2D band.

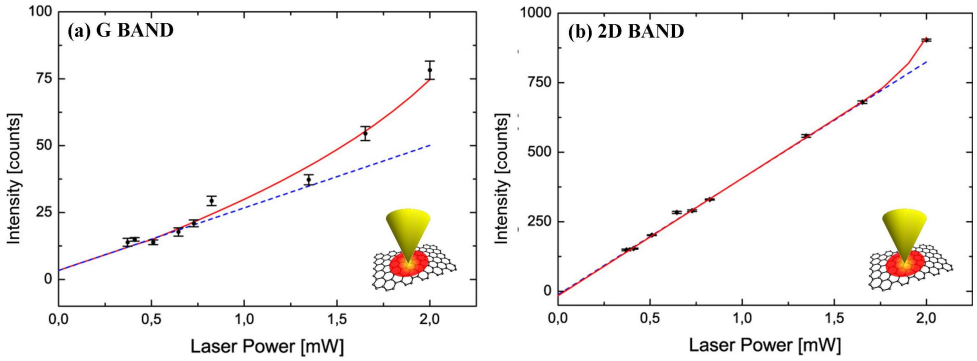

detuning factor (Δ)	$-8.9254 \cdot 10^{13}$ Hz
near-field volume	2.094410^{-24} m^{-3}
plasmon resonance frequency (wavelength)	$3.84 \cdot 10^{14}$ Hz (780 nm)
plasmon damping factor	$2.5 \cdot 10^{14}$ Hz

G band	field enhancement factor (f)	6.8
	coupling factor (g_v)	$3.9842 \cdot 10^{10}$ Hz
	weighting coefficient (C)	$2.75 \cdot 10^{14}$
2D band	field enhancement factor (f)	6.3
	coupling factor (g_v)	$6.7391 \cdot 10^{10}$ Hz
	weighting coefficient (C)	$3.5 \cdot 10^{14}$

Figure 7.8: **FIRST NANOTIP: QUANTUM NOISE APPROACH.** Simulation of the experimental data using eq. (7.2) for the G (a) and 2D band (b). The fitting parameters are reported in the table. For the simulation of the confocal background, see the parameters reported in Figure 7.5.

It is important for a successful and correct comparison between the model and the experimental results, that the smaller deviation from the linearity observed for the 2D band is attributable to the stronger confocal background, and not to the fact that the *dynamical back-action* itself is weaker for the 2D band compared to the G band.

In the comparison of the contribution given by the *dynamical back-action* for the G and the 2D band, it important to discuss also the role of the different parameters involved. The polarizability change for the 2D band, as estimated before, is roughly twice larger than for the G band. A larger polarizability change leads to a larger coupling factor g_v. The coupling factor depends also, on the other hand, on the vibrational frequency ω_v (see eq. 5.10). In particular, it is inversely proportional to the square root of ω_v, which is for the 2D band roughly twice larger than for the G band. In Figure 7.9b the Raman response is simulated using the polarizability change estimated for the 2D band and a smaller vibrational frequency. For a smaller frequency, the increase of the coupling factor, would lead to a substantial increase of the Raman response. Another parameter limiting the increase of the Raman response of the 2D band, with respect the the G band, is the phonon damping factor. As discussed in Chapter 5, the divergence of the Raman response is expected for

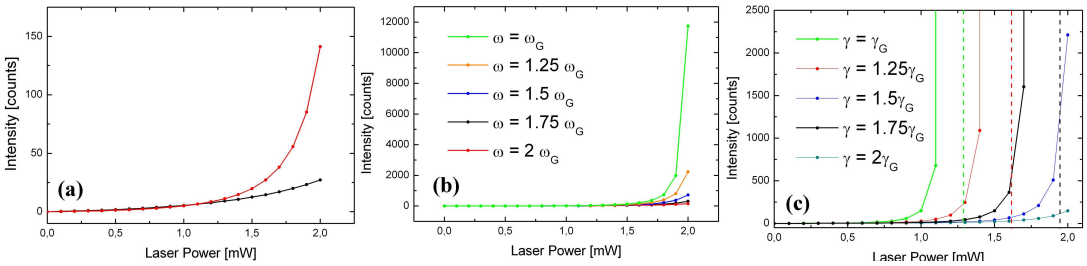

Laser Power [mW]	0.4	0.5	0.64	0.73	0.82	1.3	1.66	2
G BAND (%)	9.189	13.305	13.460	14.371	12.671	24.429	26.847	34.706
2D BAND (%)	0.57	0.600	0.615	0.790	0.900	1.992	5.603	15.641

Figure 7.9: (a) emission intensity due to dynamical back-action for the G (black line) and the 2D band (red line). Both curves are scaled by the respective weighting coefficient as in Figure 7.5. The two curves represent then the last term in eq. (7.2). In (b) the trend is simulated using the Raman tensor and the vibrational frequency intrinsic of the 2D band and different phonon damping factors taken as fraction of the G band phonon damping factor. For $\gamma_v = \gamma_v(G)$ the signal would diverge for smaller input power, the curve for $\gamma_v = 2\gamma_v(G)$ restores the values of panel (a). The divergence appears sooner, because it is given by the condition $\gamma_v = -\gamma_{opt}$ (see Chapter 5). In panel (c) the Raman tensor and the phonon damping of the 2D band are used to simulate the trend for different vibrational frequencies, as before given in fraction of the G band vibrational frequency. In this case no divergence is reached, but the signal increases for smaller frequencies. This is because the coupling factor g_v is inversely proportional to the square root of the vibrational frequency (see Chapter 5). Again for $\omega = \omega(G)$ the red curve in panel (a) is restored. In the table the contribution of the dynamical back-action signal to the total signal is given in percentage, for increasing power. As it can be seen, this contribution is smaller for the 2D band than for the G band.

the condition $\gamma_{opt} = -\gamma_v$. A higher phonon damping factor then, shifts the divergence to higher laser powers. Consequently, the deviation from the linear trend is going to be observed for higher powers. This can be seen also by inspection of eq. (5.67). In Figure 7.9c the Raman response is simulated for different phonon damping factor using the polarizability change estimated for the 2D band. As expected, a smaller damping factor leads to a deviation from the linearity for smaller laser powers. In conclusion, although a larger absolute value of the Raman tensor could increase drastically the response due to the *dynamical back-action*, for the 2D band this increase is partially compensated by a larger vibrational frequency, which reduces the *coupling factor* g_v, and a larger phonon damping factor, which requires higher laser power to observe a deviation from the linear trend.
Interestingly, quantitatively similar results are found also using another nanotip. The analysis of the experimental data is repeated as for the first nanotip and presented in Figures 7.10, 7.11 and 7.12.

To conclude, in this section the appearance of a non-linear response of the Raman scattering for graphene in presence of a localized plasmon given by a gold nanotip has been shown. The non-linear trend has been compared with the different models that have been developed in the theoretical part.

This measurement configuration based on the use of the gold nanotip, has the advantage of allowing for a direct comparison between the confocal and the near-field response measured at the same position. On the other hand, the plasmonic properties of the gold nanotip, essential for a correct interpretation of the experimental data, are hardly determinable with precision. In the following, the results obtained depositing gold nanorods on graphene are presented. Compared to the experiment with the nanotip, the plasmonic properties of tha nanorods are known, at least on the ensemble level.

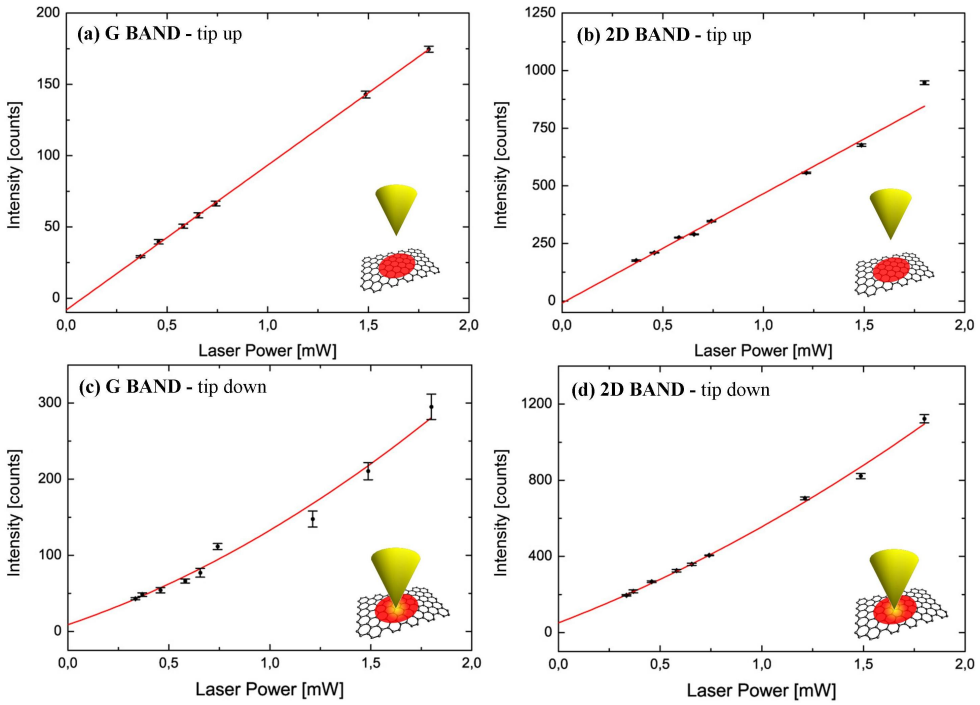

CONFOCAL	G band	2D band
intercept	10 ± 4	-2 ± 15
slope	100 ± 7	559 ± 21
NEAR-FIELD	G band	2D band
intercept	34 ± 25	51 ± 17
linear coefficient	90 ± 40	409 ± 43
quadratic coefficient	9 ± 12	95 ± 26

Figure 7.10: **SECOND NANOTIP: LINEAR-QUADRATIC FIT**. Power dependent Raman response for graphene only on glass substrate for the G (a) and 2D (b) band, and for a graphene in presence of the nanotip for the G (c) and 2D (d) band. The red line in (a) and (b) is a linear fit though the experimental points, the red line in (c) and (d) is a quadratic fit. The fit parameters are presented in the table. For a correct background subtraction the intercept should be zero within the experimental error. The intensity is obtained as the integral under the Raman peak in the spectrum and is correspondingly given is counts per wavelength (see Chapter 2).

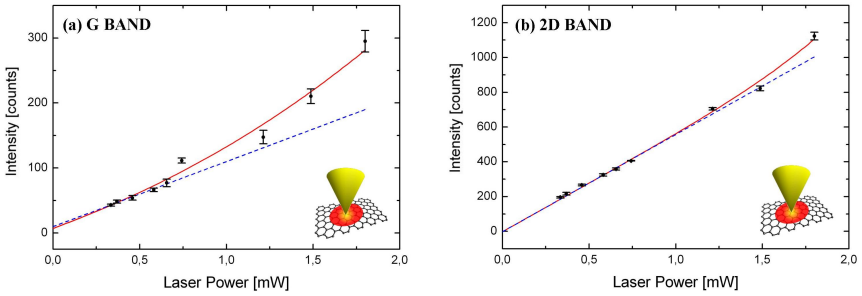

	G band	2D band
intercept (A)	6 ± 5	-2 ± 16
slope (fixed, B)	100	559
power coefficient (C)	26 ± 13	5 ± 4
exponent (N)	2 ± 1	5.1 ± 0.9

Figure 7.11: **SECOND NANOTIP: POWER FUNCTION.** Experimental data for the G (a) and 2D band (b) fit through eq. (7.1). The fitting parameters are presented in the table, the letters in parenthesis correspond to the variables as defined in 7.1. The slope is taken as fix parameter and set according to than obtained for the fit of the data from the confocal measurement (compare with Table 7.10).

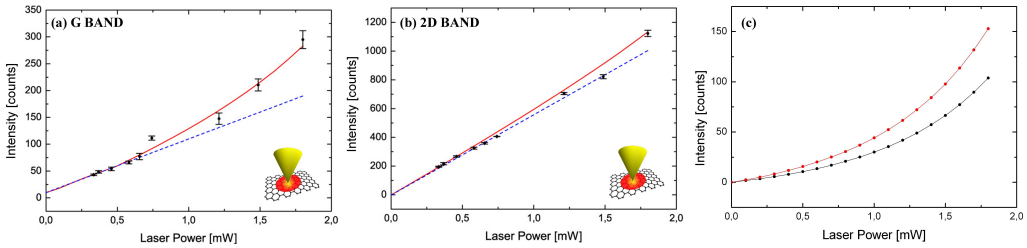

G band	enhancement factor (f)	4.8
	coupling factor (g_v)	$3.9842 \cdot 10^{10}$ Hz
	weighting coefficient (C)	$8.5 \cdot 10^{14}$
2D band	enhancement factor (f)	4.8
	coupling factor (g_v)	$6.7391 \cdot 10^{10}$ Hz
	weighting coefficient (C)	$1.35 \cdot 10^{15}$

Figure 7.12: **SECOND NANOTIP: QUANTUM NOISE APPROACH.** Simulation of the experimental data using eq. (7.2) for the G (a) and 2d band (b). The fitting parameters are reported in the table. The plasomn parameters are the same as in Figure 7.8. For the simulation of the confocal background, see the parameters reported in Figure 7.10. In (c) the emission intensity due to dynamical back-action is shown for the G (black line) and the 2D band (red line). The units are expressed after weighting in counts for wavelength for a comparison with the experimental data (see Figure 7.10 and Chapter 2).

Gold Nanorods Assisted Measurements

In this section, the results obtained after the deposition of gold nanorods on single flake graphene are presented. For the experiment, two sets of nanorods are used: both of them present a resonance around 530 nm in the green, while one set of nanorods presents the second resonance around 770 nm and the other set around 630 nm (measured in water). The resonance frequencies follow from the nanorod aspect ratio as explained in Chapter 6. Compared to the experiment with the nanotip, the advantage of using the nanorods is that the plasmonic properties are now determined, at least on the ensemble level. On the other hand, as will be discussed through the whole section, it is crucial to estimate the properties of the specific nanorod involved in the *dynamical back-action*, which is not trivial. A drawback in comparison with the experiment with the nanotip is that the confocal signal cannot be detected at the position where the nanorods are laying, as has easily been done in a tip-assisted measurement, where the nanotip was simply retracted.

"Long Nanorods" (Aspect Ratio around 3)

The results obtained from the nanorods having aspect ratio around 3 are shown first. For these measurements, similarly to the experiment with the nanotip, a HeNe laser at 633 nm is used as excitation source. The Raman lines will than be as before at 703 (G band) and 770 nm (2D band). This situation is particularly interesting, because the 2D band spectrally corresponds to the maximum of the plasmonic resonance (see extinction spectra in Chapter 6). According to the

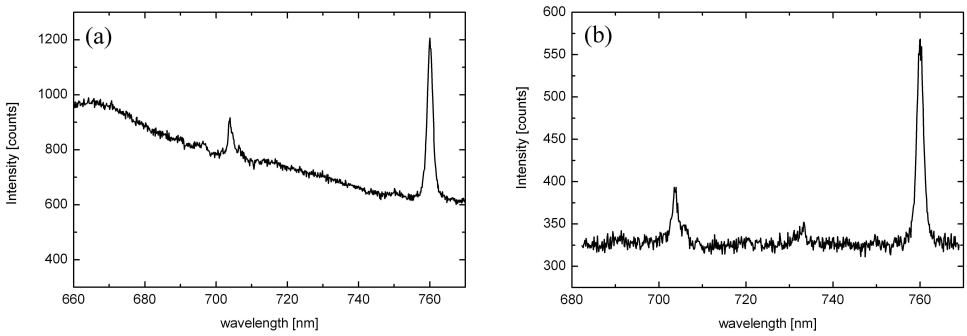

Figure 7.13: (a) graphene Raman spectrum measured in the presence of the nanorods; also the inelastic scattering background stemming from the gold nanostructure is observable. (b) graphene Raman spectrum on the same sample where no nanorods were located; the inelastic background from gold is in this case absent.

stimulated Raman picture, where the second exciting field should be given by the plasmon, this condition should be the most favorable to observe a non-linear response. Indeed for a matching between the laser and plasmonic frequency, the driven amplitude of the Raman mode should be maximum (see Chapter 4). Within the QED description, on the other hand, this frequency matching does not necessarily correspond to the best condition for observing a non-linearity. As discussed in Chapter 5, a sufficiently large damping factor (as that of these nanorods is: $\sim 5.7839 \cdot 10^{13}$ Hz, see Chapter 6), can substantially change the dependence of the *dynamical back-action* efficiency on the detuning factor (see Figure 5.4 in the Chapter 5).

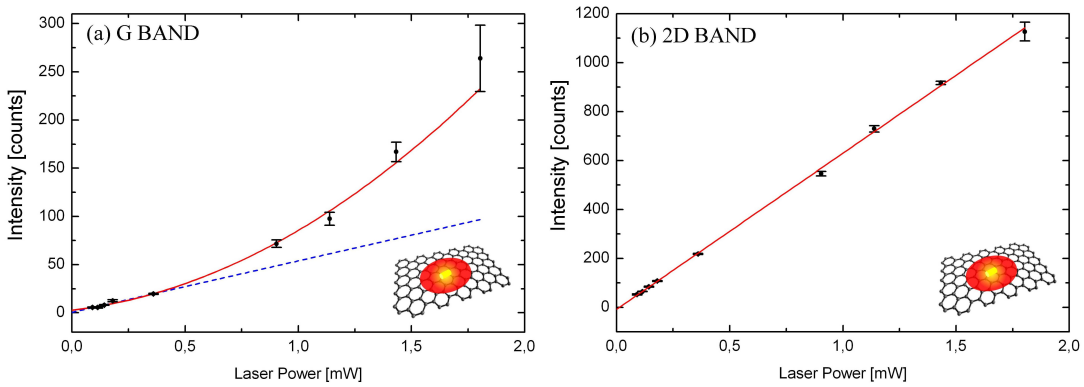

G band	intercept	3 ± 4
	linear coefficient	27 ± 7
	quadratic coefficient	55 ± 8
2D abnd	intercept	-7 ± 1
	slope	637 ± 6

G band	intercept	53 ± 4
	slope	± 1
2D band	intercept	-5 ± 1
	slope	618 ± 8

Figure 7.14: **FIRST NANOROD: LINEAR-QUADRATIC FIT.** (a) experimental data for the G band, presented with a fit through a second order polynomial function (red line), also the fitting linear function through the first five points is shown (blue dashed line). (b) experimental data for the 2D band, with a linear fit. The parameters for the second order fit for the G band and the linear fit for the 2D band are presented in the upper table. The parameters for the linear fit though the first five points are presented in the lower table.

As explained in Chapter 2 and 6, the rods are located on the sample though confocal measurements. The presence of gold is verified by the observation of the typical inelastic gold background (see Figure 7.13), similar to that observed in the nanotip experiment. The power series are obtained by recording the spectra for different laser power, as it was done in the nanotip experiment. As already discussed, the confocal and near-field signal are recorded within the same spectrum and cannot spectrally be distinguished. Differently from the measurement with the nanotip, it is in this case not possible to measure the confocal signal where the near-field one has been measured previously, because the nanorods lay on the graphene. A control measurement (not shown) has been done at a position where only bare graphene was present, showing a linear trend for both bands. Nonetheless two measurement taken at different positions can hardly be quantitatively compared. For this reason, the slope of the linear background is estimated from the first points

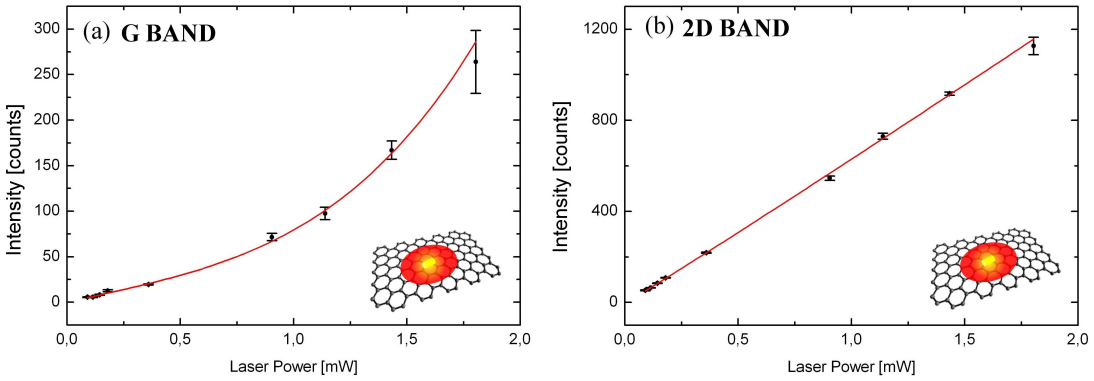

	G band	2D band
intercept (A)	$0,2 \pm 0,4$	-3 ± 3
slope (fixed, B)	54	618
power coefficient (C)	25 ± 4	$2,7 \pm 0,7$
exponent (N)	$3,5 \pm 0,4$	$1,06 \pm 0,04$

Figure 7.15: **FIRST NANOROD: POWER FUNCTION.** Fit with a power function according to eq. (7.1) for the G band (a) and the 2D band (b). The fitting parameters are presented in the table.

of the series. Doing so, it is assumed that the contribution given by the *dynamical back-action* is negligible compared to the confocal background for low laser power (for a verification of this assumption, see Figure 7.9). The experimental results are shown in Figure 7.14. In this case, a strong non-linearity for the G band is observed, while the 2D band shows a linear trend. To extract the contribution of the confocal background, a linear fit through the first five points is done, and also presented in Figure 7.14. For the 2D band, the slope extracted though the first five points is very similar to that extracted for the complete trend.
For a comparison with the stimulated Raman model discussed in Chapter 4, the experimental data are fit with a power function, summed to a linear function according to eq. (7.1). The slope for the linear function is taken from the fit though the first points presented in Figure 7.14. The resulting fits for the G and the 2D bans are presented in Figure 7.15. For the G band the fit is successful and the exponent results to be around three, which would be consistent with the stimulated Raman model. On the contrary, for the 2D band the exponential function resulting from the fit would have exponent equal to one. The fitting function is then the equivalent of the sum of two linear functions. As pointed out before, in the framework of a stimulated Raman process where the second field is provided by the plasmon, it is strange that a non-linearity is observed for the G band while it is not for the 2D band. The matching between the plasmon frequency and the phonon frequency should provide the best condition for the 2D band.

The experimental results are quantitatively compared also with the theoretical result from the QED description, using eq. (7.2). This comparison is presented in Figure 7.16. An advantage in

this case, compared to simulation which was performed for the results obtained with the nanotip, is that the plasmon parameters are known, at least on the ensemble level. This allows for a more precise determination of the *detuning factor* and for the plasmon damping factor, which are crucial for the simulation. On the other hand, it should be kept in mind, as it has been discussed in Chapter 6, that very likely several nanorods are present within the confocal spot during the same measurement. It should also be remembered that the dimension of the nanorods are not uniform among the nanorods batch, and they can significantly change from one rod to the other, such that the plasmonic properties can also correspondingly change. This fact actually does not allow to completely remove the uncertainty about the plasmonic parameters. To completely remove the uncertainty about the plasmonic parameters to be used in the simulation, in the case several nanorods are present inside the laser focus, the information about the specific nanorod giving rise to the *dynamical back-action* should be accessible (it could be, for example, the nanorod closer to the graphene layer, that giving the larger field enhancement or that which orientation on the sample surface matches the laser field polarization direction). This aspect is further discussed in the following.

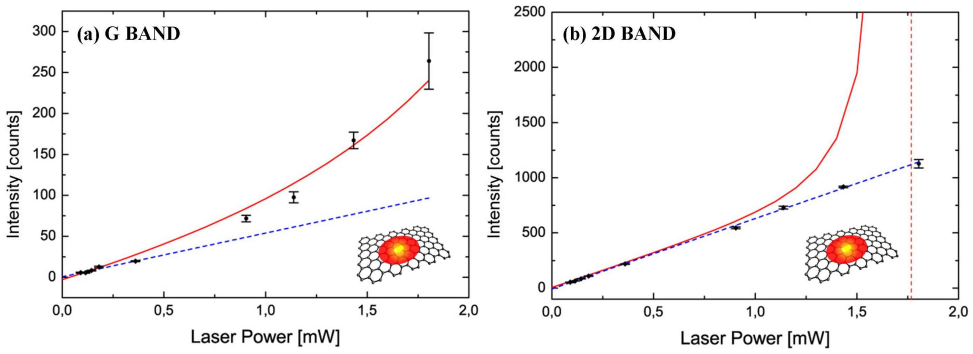

detuning factor (Δ)	$-8.426 \cdot 10^{13}$ Hz
near-field volume	3.238710^{-24} m^{-3}
plasmon resonance frequency (wavelength)	$3.8933 \cdot 10^{14}$ Hz (770 nm)
plasmon damping factor	$5.7839 \cdot 10^{13}$ Hz

G band	enhancement factor (f)	10
	coupling factor (g_v)	$1.635 \cdot 10^{10}$ Hz
	weighting coefficient (C)	$4.1 \cdot 10^{14}$
2D band	enhancement factor (f)	10
	coupling factor (g_v)	$2.3124 \cdot 10^{10}$ Hz
	weighting coefficient (C)	$5.4 \cdot 10^{14}$

Figure 7.16: **FIRST NANOROD: QUANTUM NOISE APPROACH.** (a) simulation of the experimental data according to eq. (7.2) (red line) for the G (a) and the 2D band (b); also the line used to simulate the confocal background is presented (blue dashed line). The red dashed vertical line shows the asymptote for the 2D band. The parameters for the confocal background are taken from Figure 7.14.

To simulate the confocal background, the fitting parameters for the linear function fitting the first five points of the series are taken, as explained before (see Figure 7.14). The near-field volume is taken to be half a sphere around the rod apex. In this case two apexes are present and not only one, so the resulting near-field volume is larger than it was for the nanotip. [2] As for the interpretation of the results with the nanotip, a value for the weighting factor has to be set arbitrary. This value and the field enhancement factor are the free parameters in the simulation. From the experimental data of the G band, an enhancement factor of 10 and a weighting factor of $3.9 \cdot 10^{15}$ are found. When the same parameters are used to try to reproduce the trend of the 2D band, the signal intensity as predicted by the *Quantum Noise Approach*, diverges. Compared with the G band, the divergence is caused by a larger coupling factor for the 2D band and a better match between the detuning factor ($\Delta = -8.426 \cdot 10^{13}\,\mathrm{Hz}$) and the vibrational frequency ($\omega_v = 7.914 \cdot 10^{13}\,\mathrm{Hz}$). Compared with the experiment with the nanotip, the divergence appears for smaller powers because of a smaller plasmon damping factor (compare with eq. 5.67). That the signal diverges for a finite input power is of course unphysical. Despite the moderate field confinement, a *pumping factor* sufficiently high to observe this divergence is reached in this experiment because of the high number of graphene unit cells involved in the process. In this regime, the result obtained by the *Quantum Noise Approach* looses accuracy. To compare the theory with the experimental results in this regime, a numerical calculation as that mentioned in Chapter 5 would bee needed. Indeed, the analytical result overestimate the Raman response for increasing power when the *coupling factor* increases in comparison with the plasmon damping factor [45], which is equivalent to say, when threshold for the *pumping coefficient* is decreased (see Figure 5.2). It is worth to note, however, that even close before divergence, the predicted deviation from the linearity for the 2D band is very weak, when the signal intensity due to *dynamical back-action* is summed to a the confocal signal. Again, this can be attributed to the strong confocal background. Presumably, a numerical calculation would predict a very small deviation from the linear trend on top of the confocal background.

Interestingly, the same situation is found also when the power series are recorded on another sample position, where different nanorods are present. The results are very similar also from a quantitative point of view (see Figure 7.18, 7.19 and 7.20).

The role of the plasmon resonance frequency is briefly discussed in the following, in relation to the experimental data. As already pointed out, the plasmon damping factor is in this case sensibly smaller than that assumed for the nanotip. This makes the matching between the vibrational frequency and the *detuning factor* more critical. In this sense, the signal contribution due to the *dynamical back-action* can change drastically for small changes in the plasmon resonance frequency. This situation is illustrated in Figure 7.17. If the plasmon resonance is shifted to 750 nm ($\Delta = -7.388 \cdot 10^{13}\,\mathrm{Hz}$), the divergence appears even for smaller values of the power (compare with Figure 5.5 and the discussion in Chapter 5). If it is shifted to 790 nm ($\Delta = -9.412 \cdot 10^{13}\,\mathrm{Hz}$) not only the divergence disappears, but even the deviation from the linear behavior is barely observable. All these values for the plasmon resonance are well included within the width of the absorption spectrum, due to the dimension distribution of the nanorods. The predicted deviation from the linearity changes of course also for the G band, when changing the plasmon resonance, but the change is less drastic (no divergence is observed, see Figure 7.17). This is due to the larger difference between the *detuning factor* and the vibrational frequency, in addition a slightly smaller

[2] For and estimate of the near-field volume and the near-field distribution it is referred to [129].

coupling factor for the G band. This is an example of why the plasmonic parameters need to be know with high precision: especially when the *detuning factor* and the vibrational frequency are close to each other, a small change in the plasmon resonance frequency can drastically change the signal contribution due to *dynamical back-action*.

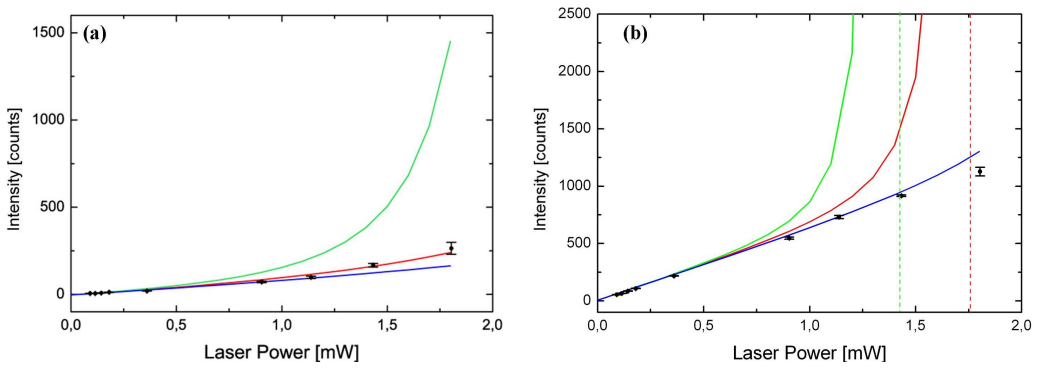

Figure 7.17: **FIRST NANOROD: ROLE OF THE DETUNING.** Raman response calculated according to eq. (7.2) for the G (a) and 2D band (b) for different plasmon resonance frequencies and correspondingly for different *detuning factors*. The blue, red and green line correspond to a *detuning factor* of $-7.388 \cdot 10^{13}$ Hz (corresponding to a plasmon resonance $\lambda_P = 750$ nm), $-7.914 \cdot 10^{13}$ Hz ($\lambda_P = 770$ nm) and $9.412 \cdot 10^{13}$ Hz ($\lambda_P = 790$ nm) respectively. The experimental data are presented as well for comparison. See text for explanation.

In conclusion, a strong non-linearity for G band has been observed after the deposition of gold nanorods on a single layer graphene. The appearance of this non-linearity can be well explained through QED model for the *dynamical back-action*. The signal contribution predicted through the *Quantum Noise Approach* is strong enough to explain the deviation from the linearity, which is experimentally observed. On the other hand, this non-linearity is not experimentally observed for 2D band. According to the stimulated Raman model developed in Chapter 4, the matching between the plasmonic resonance and the phonon frequency (as it is the case in this experiment for the 2D band) should be the best condition for observing non-linearity. Also, the stimulated and spontaneous Raman response depend both strongly on the Raman activity. Consequently, for the same fields amplitude, a stronger spontaneous Raman response should also correspond to a stronger stimulated Raman response. For these reasons, according to this model, the non-linearity should be stronger for the 2D band than for tht G band. This prediction do not correspond to the experimental observation. The appearance of the non-linearity for the G band can be explained through the *Quantum Noise Approach*, within the QED description. For the 2D band, the same model predict a divergence of the Raman response for finite input power. An infinite signal response for a finite input power has no physical meaning. That the *Quantum Noise Approach* predicts a divergence of the Raman response, is due to the fact that the *pumping coefficient* Ω approaches its threshold value (see eq. 5.67), because of a sufficiently high coupling factor g_v with respect to the plasmon damping factor. In this regime the *Quantum Noise Approach* looses accuracy and a simulation based on the numerical solution of eq. (5.54) would be appropriate. It should also be considered that in this regime the dependence of the Raman response on the plasmonic resonance

is extremely critical. In this sense, the plasmonic properties of the specific metallic nanostructure involved in the coupling with the vibrational mode is essential.

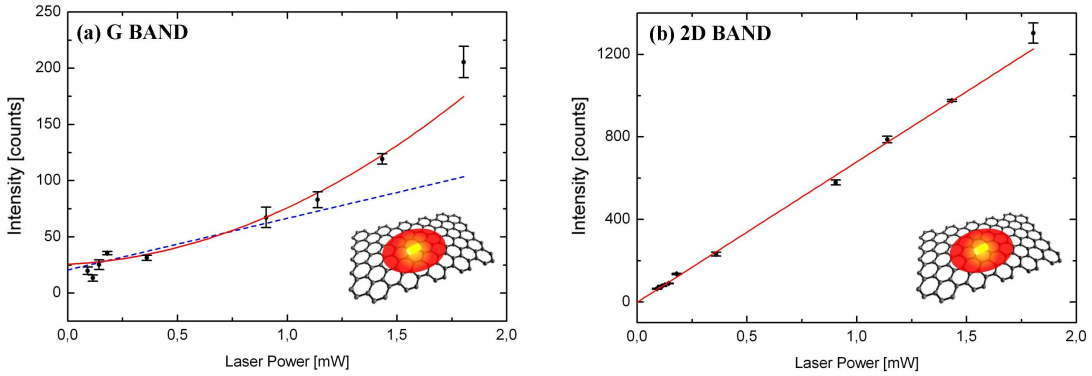

G band	intercept	25 ± 8
	linear coefficient	9 ± 42
	quadratic coefficient	40 ± 27
2D band	intercept	-2 ± 3
	slope	638 ± 10

G band	intercept	46 ± 30
	slope	20 ± 7
2D band	intercept	3 ± 7
	slope	640 ± 43

Figure 7.18: **SECOND NANOROD: QUADRATIC-LINEAR FIT.** (a) experimental data for the G band, presented with a quadratic fit (red line), also the linear function fit through the first five points is shown (blue dashed line). (b) experimental data for the 2D band, with a linear fit function. In the upper table the parameters for the second order polynomial fit are presented: in the lower table the parameters for the linear fit through the first five points are presented.

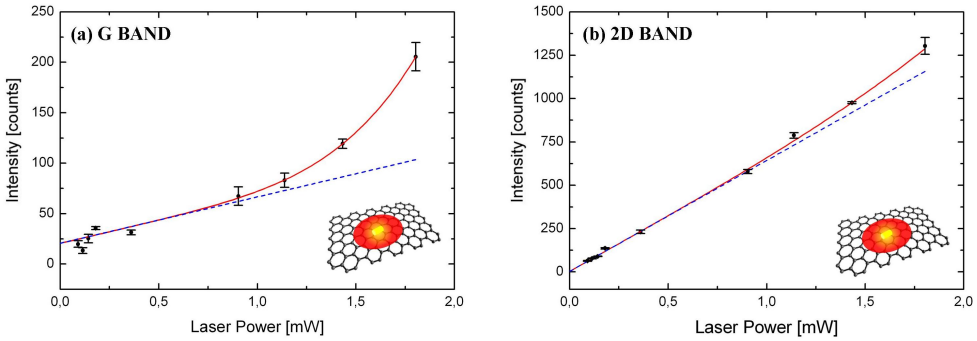

	G band	2D band
intercept (A)	20 ± 3	3 ± 3
slope (fixed, B)	46	640
power coefficient (C)	6 ± 5	15 ± 10
exponent (N)	5 ± 2	4 ± 3

Figure 7.19: **SECOND NANOROD: POWER FUNCTION**. Fit using a power function according to eq. (7.1) for the G band (a) and the 2D band (b). The fitting parameters are presented in the table. The slope is taken from the confocal fit in Figure 7.18.

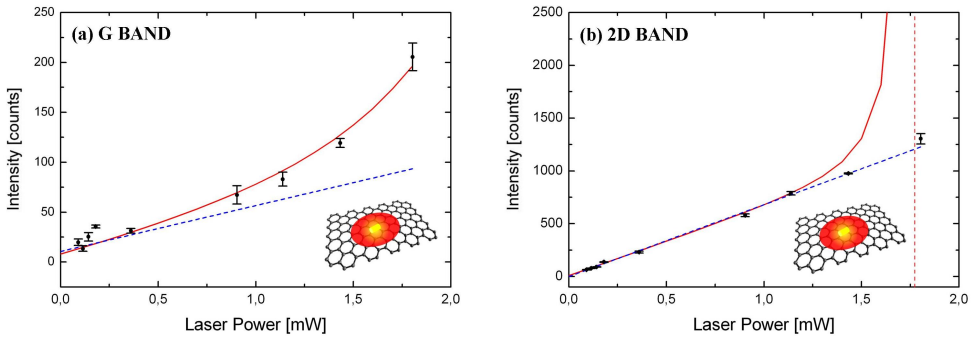

G band	enhancement factor (f)	11
	coupling factor (g_v)	$1.635 \cdot 10^{10}$ Hz
	weighting coefficient (C)	$2.46 \cdot 10^{14}$
2D band	enhancement factor (f)	11
	coupling factor (g_v)	$2.3124 \cdot 10^{10}$ Hz
	weighting coefficient (C)	$2.05 \cdot 10^{14}$

Figure 7.20: **SECOND NANOROD: QUANTUM NOISE APPROACH.** (a) simulation of the experimental data according to eq. (7.2) (red line) for the G (a) and the 2D band (b); also the line used to simulate the confocal background is presented (blue dashed line). The red dashed line shows the asymptote for the 2D band. The parameters for the confocal background are taken from Figure 7.14. The plasmon paramenters are the same as in Figure 7.16.

"Short Nanorods" (Aspect Ratio around 2)

In this section, the measurements done on the nanorods having aspect ratio around two are presented. As for the other nanorods, the gold nanostructures are deposited in single-layer graphene. The plasmon resonance frequency after deposition on the substrate is centered at 594 nm (see Chapter 6 for further details). For these measurements, two laser sources have been used, one at 633 nm and one at 594 nm (both of them provided by HeNe lasers). When using a 594 nm laser, the G and the 2D band of graphene appear at 655 nm and 705 nm respectively.

The aim of these measurements is that of comparing two different *detuning* conditions. This can be done, repeating the measurements using two different laser sources. To make sure that the detuning is the only changing parameter, the measurements need to be repeated on the same sample position and using the same laser polarization. Indeed, since the nanorods orientation on the sample is unknown, moving from one nanorod to another, the orientation of the laser polarization with respect to the nanorod axis could change. Changing the laser polarization relatively to the nanorod axis can in principle change the near-field distribution and consequently the enhancement factor and the near-field volume. A change in the Raman response in dependence on the laser power could the attributed not to a different *detuning* but to a change of these parameters. This ambiguity can be removed repeating the measurement on the same sample position and using the same laser polarization (for more details on the experimental procedure, see Chapter 2). Compared to the measurements presented in the previous section, in this case the laser power must be limited to around 1.1 mW. This power corresponds to the maximum power effectively reaching the sample, which can be achieved with the 594 nm laser. The results obtained after repeating the measurements on a certain sample position are shown in Figure 7.21. In general, a non-linear behavior is observed for all bands for both laser wavelengths. For the G band, there is no substantial difference in the non-linearity when changing laser wavelength, while the non-linearity is sensibly stronger for the 2D band, when the 633 nm laser is used.

The fit with eq. (7.1) gives for both the G and 2D band the same value for the exponent within the experimental uncertainty. The fitting parameters are given in Figure 7.22. The slope is taken as fix parameter from the linear fit shown in Figure 7.21. The values for the exponent for the different bands under different laser excitation are in between 2 and 3. These values are compatible with the power dependence predicted from the stimulated Raman model presented in Chapter 4.

The presence of single nanorods is in principle an advantage because it can potentially simplify the characterization of the system under observation; on the other hand the specific system (in this case, the specific nanorod on this specific sample position) need to be characterized with high precision. As already explained is Chapter 6, it has unfortunately been impossible to recognize the same sample position when switching from the dark-field to the confocal setup. The specific characteristic of the nanorods in correspondence of which the power series is recorded is then unknown and must be estimated, based on ensemble measurements and on measurements on other single nanorods on the same sample. In this sense, the potential advantage of using nanorods, with respect to the nanotip experiment, is partially lost. For these nanorods, the average plasmonic resonance after deposition on the sample is 594 nm. As a starting point, it makes sense to try to fit the experimental results supposing a positive *detuning factor*. It has been shown in Chapter 5 that also a slightly positive detuning factor can lead to a increase of the Raman signal beyond the linearity, if the plasmon damping factor is large enough. Nonetheless, this deviation is less

strong than in the case of *blue-detuning*. For this reason, in order to reproduce the experimentally observed trend, a large field enhancement factor must be assumed. Such a large enhancement factor (besides being unrealistic for single nanorods) would increase the slope of the *dynamical back-action* component very much, which makes it impossible to correctly reproduce the the experimental data. The simulation of the experimental according to eq. (7.2) is presented in Figure 7.23. For the simulation of the confocal background, the fitting parameters shown in Figure 7.21 are used. As already explained, the experimental data must be simulated supposing a negative *detuning factor*.The plasmonic resonance is then supposed to be centered at 635 nm ($4.721 \cdot 10^{13}$ Hz). This value is at the very edge of the distribution shown in Figure 6.6. Such a plasmon frequency which gives, for the red laser, a *detuning factor* equal to $-1.4916 \cdot 10^{12}$ Hz. With this *detuning factor*, the experimental data in Figure 7.23 can be reproduced assuming an *enhancement factor* of 11. The plasmon damping factor is taken as the average of the damping found for the single scattering curves ($3.876 \cdot 10^{13}$). The near-field volume is taken as the same as for the other nanorods (remember that the radius of the apex is the same for both nanorods samples). In Figure 7.23, the same parameters as those used for the simulation of the results obtained with the 633 nm laser, are used to reproduce the results found under excitation with the 594 nm laser. The only parameter which is allowed to change in this simulation is the enhancement factor, which can be different for different wavelengths. Compared to the case under 633 nm laser excitation, the *detuning factor* is now much closer to the phonon frequency of the G band. For this reason, the experimental data are simulated with a smaller *enhancement factor*, equal to 5. Similar parameters successfully reproduce also the non-linearity observed for the 2D band.

These results show that a non-linearity can actually be observed for both the G and the 2D band. They also show that the non-linear response is dependent on the laser wavelength. Indeed, although no big change in the non-linear response is observed for the G band when changing the excitation wavelength, the strength of the non-linear response changes for the 2D band when the 633 nm laser is used, compared to the 594 nm laser. The experimental data can be successfully simulated with power function according to eq. (7.1), the resulting exponent are found to be between 2 and 3. Also the prediction of the *Quantum Noise Approach* can successfully be used to reproduce the experimental data. Given the worse match between the detuning and the vibrational frequency, compared to the situation described for the "long nanorods", the *driving parameter* is far from its threshold value. This makes the simulation according to the *Quantum Noise Approach* more reliable. A conclusive explanation is however hard to be drawn for this experiment, because of the uncertainty about some fundamental parameters and because of a not straightforwardly characterizable sample. In principle, two nanorods having two different plasmonic resonances could be present at this position, causing one a non-linear response under red and the other under orange excitation.

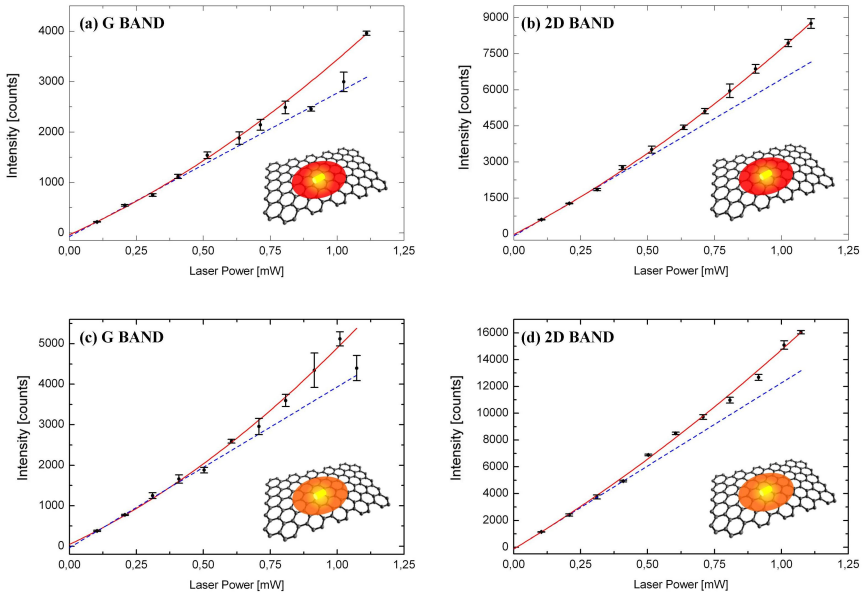

633 nm EXCITATION	intercept	linear coefficient	quadratic coefficient	ratio
G Band	-38 ± 40	2397 ± 184	1073 ± 169	$0,45 \pm 0,08$
2D Band	-16 ± 28	5810 ± 198	1916 ± 222	$0,423 \pm 0,08$
594 nm EXCITATION	intercept	linear coefficient	quadratic coefficient	ratio
G Band	22 ± 43	3330 ± 356	1382 ± 496	$0,33 \pm 0,04$
2D Band	-127 ± 140	11981 ± 724	2870 ± 800	$0,23 \pm 0,07$

633 nm EXCITATION	intercept	slope
G Band	-74 ± 28	2845 ± 187
2D Band	-73 ± 53	6511 ± 297
594 nm EXCITATION	intercept	slope
G Band	-35 ± 27	3967 ± 165
2D Band	-136 ± 7	12399 ± 51

Figure 7.21: **LINEAR-QUADRATIC FIT.** Power series using the 633 laser for the G (a) and 2D (b) band and using the 594 nm laser for the G (c) and 2D band (d). The red lines show the second order polynomial fit, the corresponding parameters are presented in the first table. The blue dashed lines show the linear fit though the first five points, the corresponding parameters are presented in the second table. In the last column of the table, the ration between the linear and quadratic coefficient is given, used to estimate the strength of the non-linearity.

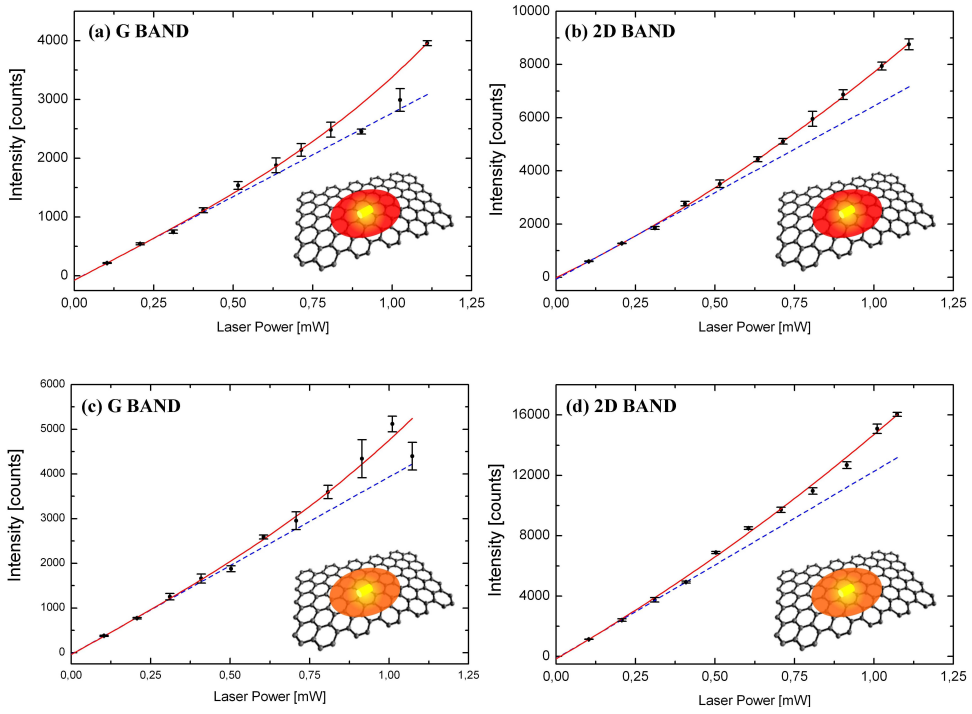

633 nm EXCITATION	intercept (A)	slope (fixed, B)	power coefficient (C)	exponent (N)
G Band	-75 ± 8	2845	612 ± 65	$3,4 \pm 0,9$
2D Band	-17 ± 60	6511	1915 ± 754	$2,0 \pm 0,6$
594 nm EXCITATION	intercept (A)	slope (fixed, B)	power coefficient (C)	exponent (N)
G Band	-40 ± 18	3967	828 ± 198	$3,0 \pm 0,8$
2D Band	-160 ± 40	12399	2463 ± 258	$2,1 \pm 0,4$

Figure 7.22: **POWER FUNCTION.** Fit of the experimental power series presented in Figure 7.21 according to eq. (7.1), (red line). The blue dashed line represents a linear fit through the first five points. The fit parameters are presented in the table.

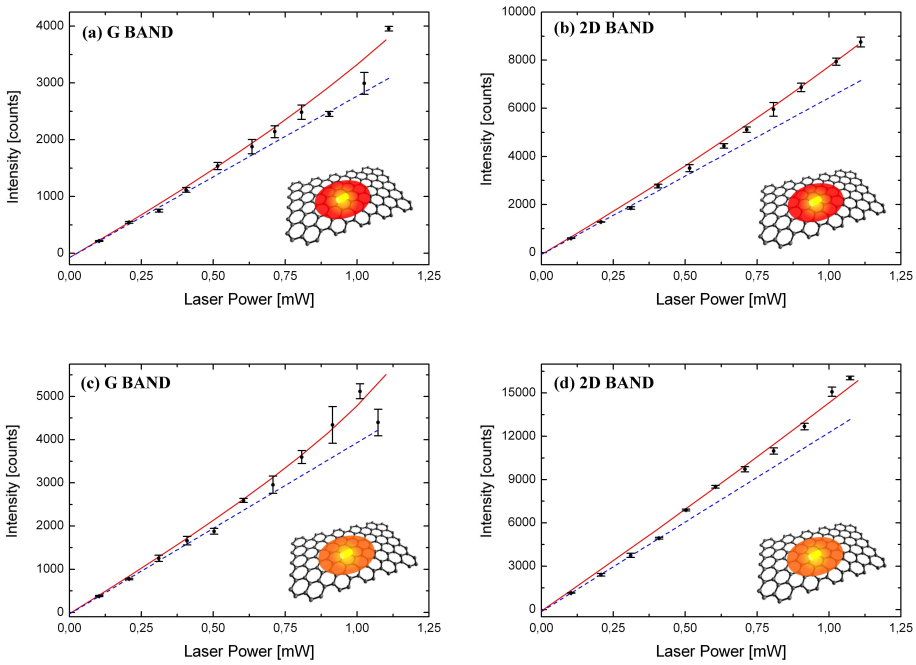

633 nm LASER	detuning factor (Δ)	$-1.4916 \cdot 10^{12}$ Hz
	near-field volume	3.238710^{-24} m^{-3}
	plasmonic damping factor	$3.876 \cdot 10^{13}$ Hz
G band	coupling factor (g_v)	$1.6147e + 10 \cdot 10^{10}$ Hz
	weighting coefficient (C)	$61.05 \cdot 10^{15}$
	enhancement factor (f)	11
2D band	coupling factor (g_v)	$2.7312 \cdot 10^{10}$ Hz
	weighting coefficient (C)	$1.05 \cdot 10^{16}$
	enhancement factor (f)	11
594 nm LASER	detuning factor (Δ)	$-3.2586 \cdot 10^{13}$ Hz
	near-field volume	3.238710^{-24} m^{-3}
G band	coupling factor (g_v)	$1.2465 \cdot 10^{10}$ Hz
	enhancement factor (f)	5
	weighting coefficient (C)	$4.05 \cdot 10^{16}$
2D band	coupling factor (g_v)	$2.7088 \cdot 10^{10}$ Hz
	enhancement factor (f)	5
	weighting coefficient (C)	$6.05 \cdot 10^{17}$

Figure 7.23: **QUANTUM NOISE APPROACH.** The experimental data presented in Figure 7.21 and 7.22 are simulated according to 7.2, (red line). The blue dashed line represents a linear fit through the first five points, see Figure 7.21. The parameters are presented in the table. The plasmonic damping factor is taken in this case to be the average of the plasmonic damping factor for the single scattering curves in Figure 6.5.

Heating Effect

In general, a metallic nanostructure under laser excitation can lead to a local strong increase of the temperature in its surrounding, due to the high ohmic losses inside the nanostructure itself. The Raman scattering, depending on the thermal occupation of the vibronic level, can become stronger for increasing temperature. In principle, the non-linearity observed for the Raman signal could be simply due to the increase of the temperature given by the nanostructure itself. This effect is less likely for the experiment with the nanotip, because the tip is not in contact with the sample, but it could in principle contribute to the non-linearity in the experiment for the nanorods: a higher incident intensity leads to a larger temperature increase and so to a stronger Raman scattering efficiency. In the following, the increase in the Raman signal is modeled though a pure increase of the temperature to answer the question, if the increase in the Raman scattering could be explained with an increase of the temperature. As example, the results shown in Figure 7.14 are considered. To this aim, the Stokes Raman scattering cross-section is expressed as (the complete expression can by found, fo instance in [7]):

$$\sigma_S \sim \left(1 + n^{th}\right) \tag{7.6}$$

where n^{th} is the temperature dependent Bose-Einstein population:

$$n^{th} = \left[e^{\frac{\hbar\omega_m}{k_B T}} - 1\right]^{-1} \tag{7.7}$$

The Raman scattering power is modeled as:

$$P_S \sim \sigma_S \cdot P_L = k \cdot \left(1 + n^{th}\right) P_L + q \tag{7.8}$$

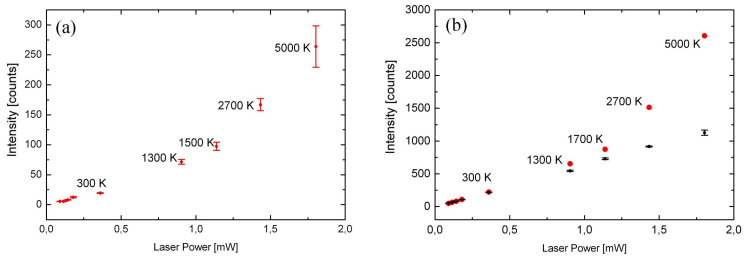

Figure 7.24: (a) the non-linear trend observed for the G band in presence of nanorods deposited on graphene under 633 nm excitation is reproduced according to eq. (7.8), the temperature needed to reproduce the experimental data is labeled correspondingly. The temperature is unrealistic being far above the melting temperature of bulk gold. (b) the intensity for the 2D band is calculated for the same temperature values used for the G band. Such a temperature, would lead to a strong deviation from the linearity also for the 2D band, which is not experimentally observed.

In eq.(7.8) the parameters k and q are taken again from the linear fit in Figure 7.14 and the temperature T is taken as free parameter to reproduce the signal increase. To reproduce the experimental trend, a temperature up to 5000 K needs to be assumed, which is far beyond the melting temperature of bulk gold. Also, an increase in the temperature should also lead to an increase of the scattering from the 2D band, although the higher vibrational frequency makes so that the increase is slower. In any case, the non-linearity observed in the experiments cannot be attributed to an increase in temperature.

Conclusions

The spontaneous Raman scattering intensity is intrinsically linear in dependence on the laser power. In this thesis, however, a non-linear Raman response from graphene and carbon nanotubes has been observed in the presence of different plasmonic nanostructures. This non-linearity has been observed for both the G and 2D band. Its occurrence has been observed to change in dependence on several parameters, such as the difference between the laser and plasmon resonance frequency and the plasmonic damping factor. The results presented in this chapter have been compared with two different models, one based on stimulated Raman scattering (see Chapter 4) and the other developed according to the *Quantum Noise Approach*, within a quantum-electrodynamic (QED) description of a coupled system composed by the plasmon and the Raman emitter (see Chapter 5).

The correspondence between the results and the stimulated Raman scattering model is generally poor. After this model, the non-linear response is expected to be maximum when the difference between the laser and the plasmon frequency is equal to the frequency of the vibrational mode. Interestingly, also the solution in the classical limit for the QED description, leads to a qualitatively similar result. This prediction has not been confirmed, for instance, in the experiment with the 3 aspect ratio nanorods ("long nanorods"), having a plasmonic resonance around 770 nm. Using a 633 nm laser, the 2D band appears at 760 nm, in correspondence of the plasmonic resonance. The difference between the laser and plasmon resonance frequency then matches in this case the vibrational frequency, which should be the best condition to observe the non-linearity according to the stimulated Raman model. Nonetheless, the 2D band showed a linear Raman response also in presence of a strong non-linearity of the G band (see Figure 7.14), for which the best matching condition is not verified. For a quantitative comparison, the trend given by the power series has been fit using the sum between a line and an exponential function. For the G band, this fit gives an exponent of 3.5 ± 0.4, while for the 2D band of 1.06 ± 0.4. For the 2D band then, no non-linear component can be identified: the results from the fit is the sum of two linear functions. It is important to point out that in the stimulated Raman picture the higher confocal background of the 2D band cannot explain the non-observation of a deviation from the linear trend on top of the linear background itself. Indeed the spontaneous and the stimulated Raman scattering have respectively a linear and quadratic dependence on the polarizability change, $\frac{\partial \alpha}{\partial x_v}$. Therefore, the stronger spontaneous Raman response of the 2D band, should be connected to a stronger stimulated response (see Chapter 4). A similar fitting procedure has been used also in literature, although the data can be well fit also with a parabola [30]. Indeed in a conventional stimulated Raman picture the Raman scattering intensity is expected to have a quadratic dependence on the intensity of the pump. On the other hand, if the vibrational mode is supposed to be stimulated by the sum of laser and plasmon fields, the Raman scattering intensity should then depend not on the second but on the third power of the laser intensity (see Chapter 4). More generally, other ambiguities are present in this model. In this last description of the stimulated Raman process, the plasmon field has been assumed to be monochromatic and to oscillate at the plasmon resonance frequency. However, the plasmonic field is usually considered to oscillate at the driving frequency (the frequency of the laser). To overcome this ambiguity, the plasmon field has been described as a broad band field [30], able to stimulate the Raman response similarly to a broad band fs-pulse in Femtosecond Stimulated Raman Spectroscopy (Fs-SRS). This intuition can be justified considering the broad spectral background related to inelastic scattering in plasmonc nanostructures [58]. On the other hand this spectral region is measured in the experiment, and the intensity of this

spectral background is far from being comparable with the laser intensity. It is then hard to think that this background can provide a field component strong enough to stimulated the Raman process.

Because of all these difficulties arising in the stimulated Raman picture, the experimental results have been compared also with a model based on a full quantum-electrodynamic (QED) description. The problem as formulated within the QED description can be solved either in the classical limit [44], taking the expectation values of the operators, or with a pure quantum-mechanical procedure [45]. Although the pure quantum solution is qualitatively similar to the one found in the classical limit, in the pure quantum solution an additional term in the phonon population appears (see eq. 5.64). Related to that, the condition for the best *detuning* changes in this description and results to be dependent not only on the matching between laser and plasmon frequency, but also on the plasmonic damping factor (see Figure 5.5). For this reason, the pure quantum solution has been compared in Chapter 7 with the experimental results, with the aim of correctly taking into account the influence of the plasmonic properties on the *dynamical back-action*. In particular, to be able to compare the results for arbitrary detuning, the solution according to the *Quantum Noise Approach* has been used. This analytical result can successfully describe the experimental data in the regime in which the *coupling factor* is sufficiently smaller in comparison with the plasmon damping factor. For an increasing *coupling factor*, this solution leads to a divergence of the Raman response for a finite input power. In this regime then, this analytical result looses validity and a numerical solution would need to be used. In the case a nanotip is used as plasmonic nanostructure, the plasmon damping factor can be assumed to be high enough, so that the solution in the *Quantum Noise Approach* can be fairly used. In this case this theoretical prediction reproduces well the experimental results: the trend of both bands can be successfully reproduced summing the confocal background to the emission intensity due to the *dynamical back-action*. A weaker or absent deviation from the linearity for the 2D band can be attributed in this case to the stronger confocal background. An advantage of using a nanotip, is that it is relatively easy to discriminate the confocal from the near-field response, in the sense that the same measurement can be repeated at the same position retracting and landing the nanotip. The disadvantage is, on the other hand, that the plasmon parameters of the nanotip are not easily determinable.

Compared to the nanotip, the plasmonic damping is smaller for gold nanorods. For this reason, and because of a good match between the *detuning coefficient* and the vibrational frequency, the regime in which the result from the *Quantum Noise Approach* predicts a divergence of the Raman response, is reached in the case of the "long nanorods" for the 2D band. For a correct reproduction of the experimental results then, a numerical simulation would in this case be appropriate. In the other cases, where this regime is not reached, the analytical solution describes well the experimental trend. A potential advantage of using nanorods (or generally speaking plasmonic nanostructures different from a nanotip) is that the the plasmonic parameters are relatively easily determinable. Anyhow, these parameters depend on the aspect ratio of the nanorod. In a chemically synthesized nanorods batch the dimensions are not exactly the same from one nanorod to the other, but a length distribution is present (see Chapter 6). This requires the characterization of the specific nanorod under observation, which can be experimentally challenging. In this sense, the uncertainty about the plasmonic parameters has not been completely removed in this experiment, even using gold nanorods as plasmonic probes, because it has not been experimentally possible to access the properties of the specific nanorods involved in the coupling with the vibrational mode. Also, the presence of more nanorods at the sample position probed during the optical measurement can make

the interpretation of the results very ambiguous.

Beside a precise determination of the plasmonic parameters, also the vibrational properties of the material under observation need to be precisely known. In the case of graphene, the polarizability change $\frac{\partial \alpha}{\partial x_v}$ (which is also named as the absolute value of the Raman tensor) has been experimentally determined for the G band [10]. This values has been used in this chapter to reproduce the experimental data. The polarizability change for the 2D band has been estimated from that of the G band, using the ratio between the intensities of the two Raman bands. Alternatively, this value could be estimated through a calibration measurement (as it has been done with the G band). Besides the polarizability change $\frac{\partial \alpha}{\partial x_v}$, also other quantities relative to the phonon need to be known. First of all, as already mentioned, the effective mass of the phonon mode must be considered explicitly. In this work, the carbon mass has been taken as the effective mass of both phonon modes, but in principle the effective mass of the two modes can be different because of the different symmetry of the vibrational modes. Another difference between the two phonon modes is that the G band results from a vibration at the center of the Brillouin Zone, having wave-vector close to zero and almost infinite wavelength. The vibration relative to the 2D band is not at the center of the Brillouin Zone, and has consequently shorter wavelength. Also, as already pointed out, the symmetry of the two vibrational mode is different. This could lead to the fact that the coherent length on which the contribution from the different lattice cells can be summed, can be very different for one vibrational mode compared to the other. On the contrary, in the simulation presented here, polarizability change $\frac{\partial \alpha}{\partial x_v}$ has been multiplied by the number of all the primitive cells inside the near-field volume, without taking into consideration the possible different coherence length. It should also be pointed out, that the QED description presented here is valid for non-resonant Raman scattering. The Raman scattering in graphene is resonant in the sense that is involves real electronic states. Related to that, other differences exist between G and 2D band modes: while the first involves three steps (photon-electron, electron-phonon and photon-electron interaction), the second involves four (photon-electron, electron-phonon, electron-phonon and photon-electron interaction; see Chapter 1). Graphene has been taken as sample material for several of its advantages, such that of being a strong Raman scatterer and of having its two main Raman modes spectrally separated enough for allowing to investigate different spectral regions within the typical width of a plasmonic resonance spectrum. On the other hand, a single molecule would probably be easier to compare with the QED description, being most of the issues listed before simpler to handle for a single molecule than for a extended crystalline sample.

Finally, in a future perspective, an improvement in the sample preparation might be necessary, in order to make sure that a single plasmonic nanostructure is present in the confocal region and to allow for the complete characterization of the nanostructure itself. This can be achieved, for example, with a lithographically patterned sample . A further improvement might be given using a zero-dimensional Raman scatterer, which would allow to remove the uncertainty about the linear component in the power series, stemming from the confocal background. Such a probe could consist of a molecule in close proximity of a metallic nanostructure, or at the junction of a dimer [130]. In both cases, the more precise design of the plasmonic nanostructure would also help to achieve a more precise determination of some fundamental parameters, such as near-field volume and field enhancement factor (besides of course plasmonic resonance frequency and damping factor). Furthermore, a precise enough fabrication procedure could allow to tune, for instance, the distance between nanostrucure and molecule, or between the two nanostructures composing the dimer, ex-

ploring different coupling regime and field confinements. With the moderate field enhancement chosen in the experiments described in this thesis, it has been shown that the plasmon itself acting as a resonance system is sufficient to form the coupled system described in Chapter 5 and that no sub-wavelength nanocavity is needed, as that used in [30]. This does not imply, however, that the investigation of strong field enhancement configuration would not be interesting. It actually becomes of high interest to combine the stronger dependence of the Raman scattering on the laser power with a nanostrucure designed to have a high enhancement factor. This might potentially be very useful to improve the sensitivity for single molecule detection achieved with surface enhanced Raman scattering.

Part IV

Raman Scattering in Beryllium-doped Gallium Arsenide Nanowires

Introduction

Semiconducting nanowires (NWs) are promising building blocks for future electronic devices, with potential applications in energy harvesting systems [71, 72, 73, 74]. The successful implementation of the NWs in electronic devices requires efficient control of growth and reliable transport behaviour. Considerable progress has been made in the fabrication of high quality NWs and in understanding their growth mechanisms [75, 76, 77, 78]. On the other hand, the achievable limit for the effective dopant concentration, and the resulting charge-carrier concentration and mobility need to be determined with higher accuracy. Gallium arsenide (GaAs) NWs are of particular interest, because they can be directly grown on Si as well as GaAs substrates and because the band gap of GaAs (1.43 eV) is at the maximum of the single junction Shockley-Queisser limit [79, 80]. Beryllium (Be) is one of the common p-type dopants for III-V semiconductors and particularly known for its high diffusion rates in GaAs [81]. Be-doping has been reported for GaAsN [82], InGaAs [83] and GaN [84]. An efficient and reliable procedure to determine the charge-carrier density and mobility in NWs is important for guiding the development of optimized fabrication techniques. While the product of the charge-carrier concentration and mobility can, in principle, be derived from 4-point electrical measurements [81, 85], the choice of the metal used for the contacts can influence the result[85]. It is therefore of particular interest to develop a reliable contactless measurement technique in order to characterize charge transport. Contactless techniques also have the advantage of requiring comparatively straightforward sample preparation, since no contact deposition step is needed. The charge-carrier concentration and mobility of undoped GaAs NWs have been determined through optical pump terahertz-spectroscopy (OPTS)[86, 87]. OPTS is a contactless technique that is well-suited for the inspection of high mobility charge carriers (for instance electrons, which mobility can be as high as $1000\,\mathrm{cm}^2/\mathrm{Vs}$ in undoped GaAs NWs [86, 87]). On the other hand, Be acts as a p-type dopant in GaAs [88], giving rise to holes with mobility orders of magnitude lower [90]. Alternatively, Raman spectroscopy has been used to prove dopant incorporation [89] and also to estimate the charge-carrier concentration and mobility in Si-doped GaAs NWs [90]. Additionally, resonant Raman spectroscopy has been used to identify the sites occupied by Be when it is incorporated as a dopant in the GaAs lattice [91].

The reliability of semiconducting NWs is strictly related also to characterization and control of their defects. The defects might indeed act as scattering regions and thus influence the electronic properties, possibly leading to a reduction in mobility and localization of the charge carriers [115, 116]. It is crucial to understand the local structure and the nature of the defects in the nanowire to control properties at nanoscales. Stacking faults and twins are the most common defects observed in NWs[110, 112]. Raman spectroscopy can be useful also for the characterization of the surface morphology. In fact, in addition to the bulk transverse optical (TO) and longitudinal optical (LO) modes, a surface optical (SO) phonon mode can exist at the interface between the nanostructure and the medium. The SO mode is dominated by oscillations from the atoms located at the surface of the wire. The appearance of SO phonon modes has been predicted theoretically and then observed in different nanostructure and most extensively in nanowires [102, 117, 118, 119, 120, 121, 122]. These modes can be in general observed for structures having a sufficiently high surface to volume ratio. SO phonons are observable as an additional peak in the Raman spectrum. Interestingly to the purpose of characterizing the surface morphology, the frequency of the SO mode depend on the surface propagation constant of the phonon along the NW axis. Assuming that the amplitude of the lattice vibration is damped in presence of defects, the surface propagation constant gives

information about the average distance between surface defects. In the following, Raman measurements are combined with Transmission Electron Microscopy (TEM) analysis in order to verify the correlation between the SO mode frequency and the mean distance between surface defects in the NWs. Indeed, beside presenting different electronic transport properties, the NWs present also a very different defects concentration, given by the different synthesis conditions needed to achieve the different doping concentrations [80].

The nanowires used in this work have been synthesized in the group of **Prof. Peter Krogstrup** of the University of Copenhagen, Denmark. The TEM measurements and the relative analysis have been done by **Dr. Sriram Venkatesan** of the group of **Prof. Gerhard Dehm** at the Max-Planck-Institut für Eisenforschung in Düsseldorf, Germany. A fundamental contribution to this work was given by **Prof. Christina Scheu** at the Max-Planck-Institut für Eisenforschung in Düsseldorf, Germany and by **Jason Röhr**, at the Imperial College London, United Kingdom.

Chapter 8

Specific Features appearing in the Raman Spectra of polar doped semiconducting Nanowires

In this chapter the basic concepts needed to interpret the features appearing in the Raman spectra of Beryllium-doped Gallium Arsenide nanowires are briefly reviewed. In particular, the coupled plasma-phonon model is presented, according to which the changes in the Raman spectrum due to the interaction between the charge carriers (provided by the dopant) and the local electric field (connected to the longitudinal optical lattice vibration) can be predicted. Additionally, the theory related to the appearance surface optical phonons and phonon confinement is discussed, being those relevant to the correct description of Raman spectra measured in this work.

Coupled-Plasma-Phonon Model

As explained in Chapter 1, the Raman spectrum of GaAs consists of two peaks, one related to the transversal optical phonons (TO) and the second related to the longitudinal optical phonons (LO). For the TO mode, the vibration of the lattice planes is perpendicular to the propagation direction. Related to that, the center of mass is conserved. For the LO phonon mode, the vibration of the atomic planes is parallel to the propagation direction, and the center of mass inside the unit cell is not conserved. Because the lattice sites are not occupied by neutral atoms but by ions, the non-conservation of the center of mass, leads to a locally non-zero local field. This aspect is discussed in the next session in terms of the field and atomic displacement divergence, within the discussion about surface phonons. In a doped polar semiconductor this field interacts with the charge carriers, given by the doping. These charge carriers can be treated like a plasma. Throughout this thesis, the Raman process has been generally formulated as a change in the polarizability α, which relates the polarization and the electric field as $P \sim \alpha E$. Analogously, the polarization can be expressed, in scalar form, as $P = \chi E$, where χ is defined as the susceptibility. Correspondingly the Raman scattering process can then be formulated as a change in the susceptibility. In polar doped semiconducting materials, there are three contributions to the change in the susceptibility [94, 93]. The first is related to the modulation of the periodic crystal potential dy the ions displacement in

the crystal lattice ($\frac{\partial \chi}{\partial u}$); the second contribution is given by the interaction of the charge carriers with the local field related to the LO mode ($\frac{\partial \chi}{\partial \vec{e}_L}$). The third contribution is given by the charge carriers themselves, which contribute to the total polarization of the medium, and is expressed as

$$\frac{\partial \chi}{\partial e} = \frac{e^2}{4\pi\epsilon_0 m^* \omega_S^2} \frac{1}{V} \int e^{i\vec{k}\vec{r}} d^3\vec{r} \tag{8.1}$$

Where e is the elementary charge, V is the crystal volume, ϵ_0 is the vacuum permittivity, ω_S is the scattered frequency and m^* is the effective mass of the charge carriers. The total polarization is expressed in scalar form in the Fourier space as $P(\vec{k}) = P_0 + N_e P_e$, where N_e is the charge-carrier concentration. It consists of one component related to the displacement, (P_0), and one related to polarization due to the charge carriers, (P_e):

$$P_0(\vec{k}) = e^* \frac{1}{V} \int \vec{u}(\vec{r}) e^{i\vec{k}\vec{r}} d^3\vec{r} \tag{8.2a}$$

$$P_e(\vec{k}) = \frac{e}{ik} \frac{1}{V} \int e^{i\vec{k}\vec{r}} d^3\vec{r} \tag{8.2b}$$

where e^* is the partial unbalanced charge related to the displacement $\vec{u}(\vec{r})$. The total polarization produces a longitudinal macroscopic electric field, expressed in Fourier space as:

$$E_L(\vec{k}) = -\frac{P(\vec{k})}{\epsilon_0 \epsilon_\infty} \tag{8.3}$$

where ϵ_∞ is the high frequency limit for the dielectric constant. The total change in the susceptibility can then be expressed as a function of the polarization:

$$\partial\chi = \frac{V}{e^*} \left(\frac{\partial \chi}{\partial u} \right) P_0 - \frac{1}{\epsilon_0 \epsilon_\infty} \left(\frac{\partial \chi}{\partial \vec{e}_L} \right) (P_0 + N_e P_e) + i N_P \frac{\partial \chi}{\partial e} P_e \tag{8.4}$$

The calculation for the Raman cross-section as a function of the susceptibility change can be carried out through the fluctuation-dissipation theorem [94]. Also, the interaction between the phonon and plasma subsystems can be taken into account in the random-phase approximation by linear response to the total effective electrical fields [93, 92]. The following expression can then be derived for the intensity of the Raman peak related to the phonon-plasma coupling [93, 94]:

$$I = I_0(n+1) \cdot (A+B) \cdot Im \left\{ -\frac{1}{\epsilon(\omega)} \right\} \tag{8.5}$$

In eq. (8.5), I_0 is a constant factor independent on the frequency, and n is the Bose-Einstein distribution. The prefactors A and B are given by:

$$A = 1 + 2C\omega_{TO}^2 \frac{\omega_{LO}^2 \Gamma \left(\omega_{TO}^2 - \omega^2\right) - \gamma\omega^2 \left(\omega^2 + \Gamma^2\right)}{\omega_P^2 \Gamma \left[\left(\omega_{TO}^2 - \omega^2\right)^2 + \omega^2\gamma^2 \right] + \gamma\omega^2 \left(\omega_{LO}^2 - \omega_{TO}^2\right) \left(\omega^2 - \Gamma^2\right)} \tag{8.6}$$

$$B = C^2 \frac{\omega_{TO}^4}{\omega_{LO}^2 - \omega_{TO}^2} \frac{\omega_P^2 \left[\Gamma \left(\omega_{LO}^2 - \omega_{TO}^2\right) + \gamma \left(\omega_P^2 - 2\omega^2\right) \right] + \gamma\omega^2 \left(\omega^2 + \Gamma^2\right)}{\omega_P^2 \Gamma \left[\left(\omega_{TO}^2 - \omega^2\right)^2 + \omega^2\gamma^2 \right] + \gamma\omega^2 \left(\omega_{LO}^2 - \omega_{TO}^2\right) \left(\omega^2 - \Gamma^2\right)} \tag{8.7}$$

In eq. (8.6) and (8.7), C is the Faust-Henry coefficient, which determines the ratio of scattering by LO and TO phonons. It is defined as:

$$C = \frac{\left[\frac{\omega_{LO}^2}{\omega_{TO}^2} - 1\right] \frac{\partial \chi}{\partial u}}{\frac{e^* \epsilon_\infty}{V_{cell}} \frac{\partial \chi}{\partial E_L}} \tag{8.8}$$

At 633 nm, it is equal to -0.37 [106]. The dielectric constant $\epsilon(\omega)$ in eq. (8.5) is expressed as the sum of the susceptibilities of the phonon and plasma subsystems:

$$\epsilon(\omega) = \epsilon_\infty + \chi_{phonon} + \chi_{plasma} = \epsilon_\infty \left[1 + \frac{\omega_{LO}^2 - \omega_{TO}^2}{\omega_{TO}^2 - \omega^2 - i\gamma\omega} - \frac{\omega_P^2}{\omega(\omega + i\Gamma)}\right] \tag{8.9}$$

In eq. (8.6), eq. (8.7) and eq. (8.9), ω_P is the plasma frequency, Γ is the plasma damping factor, γ is the phonon damping factor, ϵ_∞ is the high frequency dielectric constant for GaAs and ω_{TO} and ω_{LO} are TO and LO mode frequencies, respectively, for the undoped material. The plasma frequency and the plasma damping factor are correlated to the charge-carrier concentration and mobility, respectively, according to the following expressions:

$$\omega_P = \sqrt{\frac{e^2 N_P}{m^* \epsilon_0 \epsilon_\infty}} \tag{8.10}$$

$$\Gamma = \frac{e}{\mu m^*} \tag{8.11}$$

In eq. (8.10), ϵ_0 is the vacuum permittivity, e is the electron charge, and m^* is the effective hole mass, estimated for GaAs as $0.38 m_0$ (m_0 being the rest electron mass) [93, 90]. N_P is the charge carrier concentration. In eq. (8.11), μ is the hole mobility. The plasma-phonon coupling leads to the appearance of two modes in the case of high mobility charge carriers [94]. In the case of low mobility charge carriers one mode is totally damped and only one mode appears with frequency very close to the LO-frequency for the undoped material [92, 93]. In this specific case, the Be doping gives rise to holes, which are in GaAs low mobility change carriers. In spite of two separated peaks then, a single peak is expected.

In Chapter 9, the appearance of the CPP related peak is experimentally observed and its appearance is discussed in order to extract form its shape and position the charge-carrier concentration and mobility. The CCP model as presented in this section has already been used exactly with the aim of extracting charge carrier concentration and mobility for Si-doped GaAs NWs [90], obtaining quantitatively similar results to that presented in Chapter 9. A more precise determination could in principle by done using not the classical expression for the plasma dielectric function as in eq. (8.9), but using the Lindhard dielectric function. Nonetheless the CPP model as formulated here is valid, since for small values of the wavevector, the Lindhard dielectric constant and the classical result as expressed in eq. (8.9) coincide [7]. Similar experimental data as those presented here have been analyzed using for $\epsilon(\omega)$ the Linhard-Mermin dielectric function [126, 127].

Surface Optical Phonon Modes

In nanostructures an additional phonon mode can exist at the interface between the nanostructure itself and the surrounding medium. The appearance of this mode can be mathematically predicted [117]. In the presence of an electric field, like that correlated to electromagnetic radiation, the ions occupying the lattice sites are going to be displaced. If the displacement is considered to be given by a macroscopic field $\vec{E}$ with local field correction $\frac{4\pi}{3}\vec{P}$, and considering a short-range restoring force, the displacement $\vec{u}(\vec{r},t)$ follows the equation:

$$\tilde{m}\frac{\partial^2}{\partial t^2}\vec{u}(\vec{r},t) = -\tilde{m}\omega_0^2\vec{u}(\vec{r},t) + e\left[\vec{E} + \frac{4\pi}{3}\vec{P}\right] \tag{8.12}$$

where $\tilde{m}$ is the effective mass related to the lattice vibration. Writing the polarization as: $\vec{P}(\vec{r}) = N_{cell}e\vec{u}(\vec{r})$ and assuming a harmonic time dependence for the displacement, one finds:

$$\vec{u}(\vec{r}) = \frac{e\vec{E}(\vec{r})}{\tilde{m}(\omega_0^2 - \omega^2) - e^2\frac{4\pi}{3}N_{cell}} \tag{8.13}$$

Where N_{cell} is the number of unit cells. The electrostatic potential can be written as:

$$\phi(\vec{r}) = -\int \nabla\left[\frac{\vec{P}(\vec{r'})}{\left|\vec{r}-\vec{r'}\right|}d^3\vec{r'}\right] = -eN_{cell}\int \nabla\left[\frac{\vec{u}(\vec{r'})}{\left|\vec{r}-\vec{r'}\right|}d^3\vec{r'}\right] \tag{8.14}$$

Writing the electric field as $\vec{E}(\vec{r}) = -\vec{\nabla}\phi(\vec{r})$ and combining all equations, one finds:

$$\tilde{m}(\omega_0^2 - \omega^2)\vec{u}(\vec{r}) - e^2N_{cell}\frac{4\pi}{3}\vec{u}(\vec{r}) = -eN_{cell}\int \nabla\left[\frac{\vec{u}(\vec{r'})}{\left|\vec{r}-\vec{r'}\right|}d^3\vec{r'}\right] \tag{8.15}$$

Making divergence and curl of this last equation, it is found:

$$\left(\omega^2 - \omega_0^2 - \frac{8\pi}{3}\right)\nabla\vec{u}(\vec{r}) = 0 \tag{8.16a}$$

$$\left(\omega^2 - \omega_0^2 + \frac{4\pi}{3}\right)\nabla\times\vec{u}(\vec{r}) = 0 \tag{8.16b}$$

There are three solutions to this system of equations. The first with $\nabla\vec{u}(\vec{r}) = 0$ and $\omega^2 = \omega_0^2 - \frac{4\pi}{3}$ corresponds to the transversal optical phonon modes. The second with $\nabla\times\vec{u}(\vec{r}) = 0$ and $\omega^2 = \omega_0^2 + \frac{8\pi}{3}$ corresponds to the longitudinal optical phonon modes. The condition $\nabla\vec{u}(\vec{r}) = 0$ is the equivalent of stating that the center of mass does not change. Following from eq. (8.13), the field divergence is also equal to zero. From this, no local charge and consequently no local field are related to the TO vibrational mode. In the case of the LO vibrational mode, the center of mass changes, which is consistent with the condition $\nabla\vec{u}(\vec{r}) \neq 0$. As a consequence also the field divergence is different from zero, and the local charge is consequently non-zero as well (see eq. 8.2a, where the partial unbalanced charge e^* was inserted in relation to the displacement $\vec{u}(\vec{r})$). Consequently there is a

local field associated to the LO mode. With respect to the discussion in the previous section, the susceptibility change with the atomic displacement $\frac{\partial \chi}{\partial u}$ and with the local field $\frac{\partial \chi}{\partial \vec{e}_L}$ are related to the divergence of the displacement and of the local field.

The third solution is found for both displacement divergence and curl equal to zero and corresponds to the surface optical phonon modes. Form eq. (8.13), it follows that the curl and the divergence must be zero for the field as well. The combinations of these two conditions implies: $\nabla^2\phi(\vec{r}) = 0$. The problem reduces then to the solution of Poisson's equation. For simplicity the NW can be approximated to a cylinder, so that Poisson's Equation can be solved in cylindrical coordinates.

Factorizing the potential as: $\phi(r, \theta, z) = R(r)\Theta(\theta)\Omega(z)$, the solutions for the functions are:

$$\frac{\partial^2}{\partial z^2}\Omega(z) = -q^2\Omega(z) \tag{8.17a}$$

$$\frac{\partial^2}{\partial \theta^2}\Theta(\theta) = \pm n^2\Theta(\theta) \tag{8.17b}$$

$$\frac{r}{R(r)}\frac{\partial}{\partial r}\left[r\frac{\partial R(r)}{\partial r}\right] + q^2r^2 \pm n^2 = 0 \tag{8.17c}$$

The equation for $R(r)$ can be written as a function of the variable $x = qr$ as:

$$\frac{1}{x}\frac{\partial}{\partial x}\left[x\frac{\partial R(x)}{\partial x}\right] + R(x)\left(1 \pm \frac{n^2}{x^2}\right) \tag{8.18}$$

This last equation corresponds to Bessel's Equation of the first kind. The potential must be regular at the middle of the NW ($r = 0$) and at infinite ($r = +\infty$). Taking the first order solution for $n = 0$, the potential inside and outside the NW is:

$$\phi_{inside} = I_0(x)\Theta(\theta)\Omega(z) \tag{8.19a}$$

$$\phi_{outside} = K_0(x)\Theta(\theta)\Omega(z) \tag{8.19b}$$

where I and K are Bessel's functions. Setting the boundary conditions for the electric field at the interface between NW and the surrounding medium, fives for the dielectric function of the NW:

$$\epsilon(\omega) = -\epsilon_m\frac{I_0(qr)K_1(qr)}{I_1(qr)K_0(qr)} \tag{8.20}$$

which by comparison with the expression for the frequency dependent dielectric function

$$\epsilon(\omega) = \epsilon_\infty + \frac{\omega_{TO}^2(\epsilon_S - \epsilon_\infty)}{\omega_{TO}^2 - \omega^2} \tag{8.21}$$

gives for the SO phonon frequency:

$$\omega_{SO} = \omega_{TO}\frac{\epsilon_S - \epsilon_m f_q}{\epsilon_\infty - \epsilon_m f_q} \tag{8.22}$$

where:

$$f_q = -\frac{I_0(qr)K_1(qr)}{I_1(qr)K_0(qr)} \tag{8.23}$$

From eq. (8.22) follows that the frequency of the So phonons depends on the product between the radius of the NW r and the quantity q. q is defined from eq. (8.17a) and is the spatial propagation constant, related to the spatial period of the oscillation in the axis direction by $q = \frac{2\pi}{L}$. L gives then the distance between the poles of SO phonon amplitude oscillation along the NW axis. If the defects cause the damping of the amplitude, this period should correspond to the average distance between the surface defects. This intuition is verified though Chapter 9.

Before concluding, it is worth to points out, why this mode is a surface mode. The displacement is, following from eq. 8.13, proportional to the electric field, and consequently proportional to the gradient of the potential. The component of the displacement along the radial direction is the product between the Bessel function $I_1(x)$ and a harmonic function. The displacement is then close to zero in the middle of the wire and maximum at the NW surface. It then decays symmetrically (following the Bessel function $K_1(x)$) from the NW surface into the surrounding medium. The oscillation involves then mostly the surface lattice sited, while it is comparatively negligible for the other lattice sites closer to the NW middle region.

Phonon Confinement

When the dimensions of a nanostructure are comparable with the phonon wavelength, the phonon cannot be approximated to propagate in and infinite space, but it will be spatially confined. The Raman peak position and shape depend in this condition on the confinement dimension itself. The phonon wavefunction for an infinite crystal $\psi(\vec{r})$ is then weighted by a confinement function:

$$\tilde{\psi}(\vec{r}) = w(\vec{r})\psi(\vec{r}) \tag{8.24}$$

If the weighting function is taken to be a Gaussian, and if again the NW is approximated to be a cylinder, the Raman intensity can be calculated as [104]:

$$I = \int_{BZ} e^{\left[\frac{q^2 D^2}{16\pi^2}\right]} \frac{dq^3}{\left[\omega - \omega(q)\right]^2 + \frac{\gamma^2}{4}} \tag{8.25}$$

where the integral is extended to the first Brilluoin Zone. D is the confinement dimension, q is the phonon wavevector, γ is the phonon damping and $\omega(q)$ is the frequency given by the dispersion relation. The dispersion relation is usually taken as that of a bi-atomc chain [102, 107], and is then give by [7]:

$$\omega(q) = C\sqrt{\frac{m_{Ga} + m_{As} + \sqrt{m_{Ga}^2 + m_{As}^2 + 2m_{Ga}m_{As}\cos(qa)}}{m_{Ga}m_{As}}} \tag{8.26}$$

where a is the distance between adjacent planes, m_{Ga} and m_{As} are the Gallium and Arsenide atomic masses and C is the force constant between the lattice atoms. It can be found setting $\omega(q)$ equal to ω_{TO} or ω_{LO} for $q = 0$. It should be pointed out that the choice of a Gaussian shape for the confinement is arbitrary and the expression of the confinement through other functions leads to equivalent results [103].

For a NW the differential dq^3 can be substituted with $2\pi q dq$. Doing so, only the confinement on the radial direction is considered while the wire is taken as infinite on its axis. Using this model the characteristic confinement dimension for GaAs-NW has been recently set to 23 nm [102]. Calculated Raman spectra for different wires diameters are shown in Figure 8.1. For this calculation the central frequency of the TO-mode has been taken. On the other hand, it is possible that the confinement is not on the radial direction but on direction of the axis (this would be the case, for instance, in the confinement were given by two defects along the NW axis, as it was discussed in the previous section for the damping of SO phonons). In this case, eq. (8.25) is simplified to a single integral. Calculated Raman spectra for this confinement situation are shown in Figure 8.2.

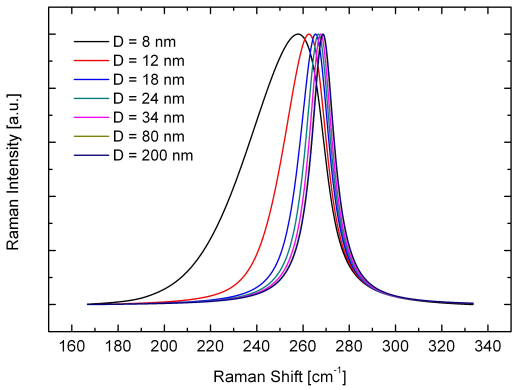

Figure 8.1: Raman spectra from a NW for different confinement dimensions (D)on the wire radius.

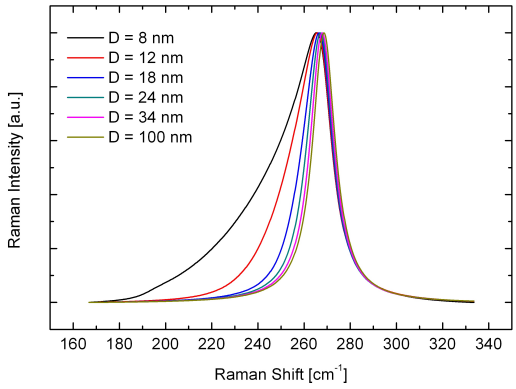

Figure 8.2: Raman spectra from a NW for different confinement dimensions (D) on the wire axis.

Chapter 9

Beryllium-doped GaAs Nanowires

In this chapter experimental results on Beryllium-doped Gallium Arsenide nanowires are presented. First, the structural characterization of the nanowires, done by Transmission Electron Microscopy, is shown. Second, the Raman measurement on the nanowires are presented. Form those, the charge carrier concentration and mobility are extracted, according to the CPP model. Additionally, the appearance of surface phonons is correlated to the structure as derived in the first part from transmission electron microscopy measurement.

Introduction

Au free self-catalyst GaAs nanowires can be grown using molecular beam epitaxy (MBE). This method allows to tailor and control the crystal structure and defect density [108, 109]. In III-V binary semiconductor, the bulk GaAs in cubic zinc blende (ZB) structure is the thermodynamically stable phase with a closed pack ABCABC stacking sequence of along the [111] direction, see [110]. However, when grown as NW, depending on the growth conditions like partial pressures, temperature and catalyst droplet size, segments of hexagonal wurtzite (WZ) arrangement with their ABAB stacking sequence along the [0001] direction can co-exist, see [111]. Reports also show the possibility to grow pure WZ GaAs NW by tuning the growth conditions [112]. The difference in their Gibbs free energies between these two crystallographic structures is small, hence the energetic barrier for nucleation of a crystal is in the same order of magnitude resulting in a polytypism [113]. The NWs are fabricated on (111) Si substrates using a self-catalyzed vapour-liquid-solid (VLS) growth method in a Varian Gen-II molecular beam epitaxy (MBE) system. Details about the synthesis and the diffusion mechanism of the dopant inside the NW can be found in literature [81]. The nominal Be concentrations are $1 \cdot 10^{18}\,\mathrm{cm}^{-3}$ (sample A), $1.5 \cdot 10^{19}\,\mathrm{cm}^{-3}$ (sample B), $3.5 \cdot 10^{19}\,\mathrm{cm}^{-3}$ (sample C), $4.6 \cdot 10^{19}\,\mathrm{cm}^{-3}$ (sample D), as listed in Table 9.1.

TEM observations show that all the wires crystallize in the cubic ZB structure and grow along [111] (see Figure 9.1) with a rare fraction (1 unit) of thin WZ segments found in 1 out of 10 in the NWs of sample B. To have a WZ structure in ZB segments, two consecutive twins planes (i.e a twin plane for every alternating monolayer) or two stacking faults are required to alter the stacking sequence from ABCABC to ABCA|C|A (where CACA forms the WZ structure) along the growth direction.

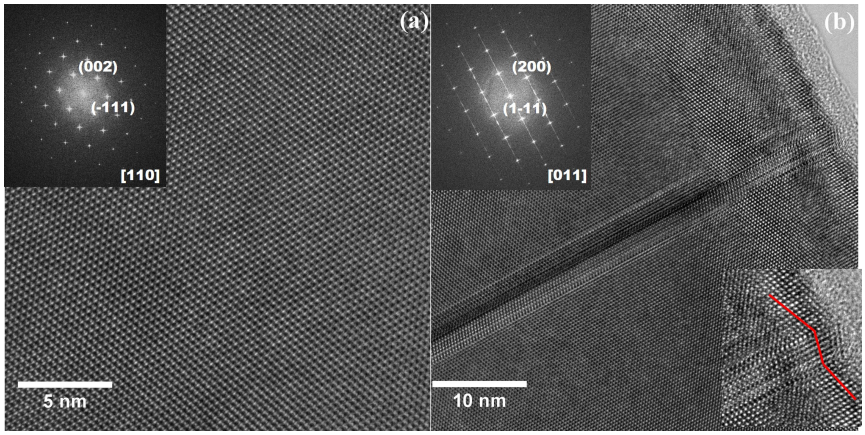

Figure 9.1: High resolution TEM images showing (a) twin free segment and (b) paired twin segment of a wire from sample type B and their corresponding fast Fourier transformation is shown as inset. The inset in the right corner of figure (b) shows the zig zag feature at the surface due to the presence of a paired twin.

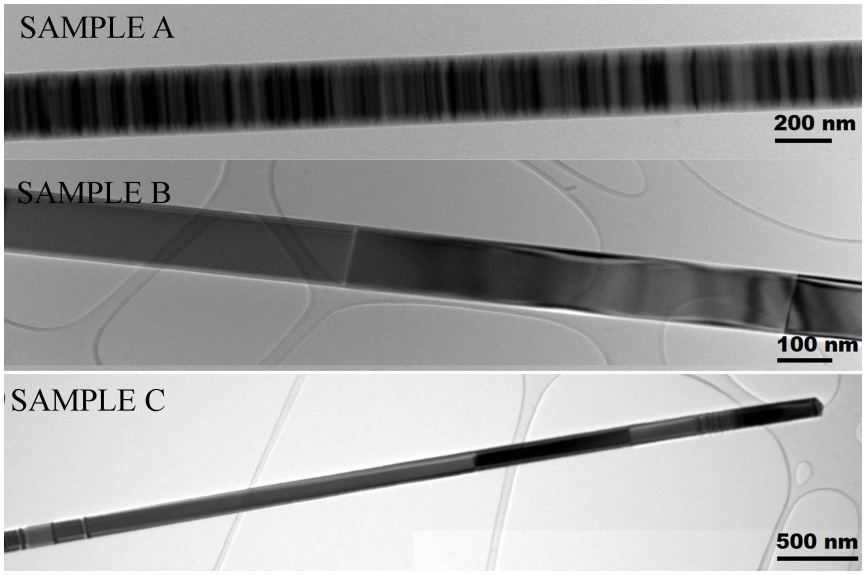

Figure 9.2: Bright field TEM overview images of the sample types A, B and C (correspondingly labeled) showing different twin densities.

However, rotational twins observed in the NWs are entirely of single twin in nature. In addition to single twins, paired twins were most commonly observed. The term paired twin is used, when a twin follows in the vicinity (few monolayers apart) of the random single twin as described in literature [114]. The general feature in sample B and C is that a small region in the beginning and at the end of the NW is more heavily twinned than the major portion of the NW. The NWs belonging to sample A presents a much larger defects concentration, being the spacing between consecutive twins only 10-50 nm. From TEM images the average thickness and length of the nanowires were deduced. The nanowires in sample type A are 200 ± 15 nm thick and $6.5 \pm 0.5\,\mu$m long; for sample B the values are 120 ± 5 nm and $9 \pm 2\,\mu$m and for sample C 135 ± 15 nm and $5.5 \pm 0.4\,\mu$m. All the NWs have constant width with slight or almost no tapering, as it can been seen in Figure 9.2.

Charge Carrier Concentration and Mobility Determination

In this section, the Raman measurements on beryllium-doped gallium arsenide NWs, having different dopant concentration are presented. The experimentally measured peaks are reproduced using eq. (8.5). Doing so, the charge-carrier concentration and mobility can be extracted from the shape and position of the Raman peak. For this estimation, also the peak related to SO phonons needs to be correctly taken into account.

A typical Raman spectrum from a NW belonging to sample B (nominal concentration $1.5{\cdot}10^{19}\,\mathrm{cm}^{-3}$) is presented in Figure 9.6. To model such a spectrum, it is necessary to take the sum of three peaks. The first peak corresponds to the TO phonon mode at $268\,\mathrm{cm}^{-1}$ and can be simulated with a Lorentzian lineshape function. The second peak is centered at an energy close to that of the LO phonon mode at $291\,\mathrm{cm}^{-1}$. This peak, is that related to the CPP. The exact peak position depends on the charge-carrier concentration, as discussed in Chapter 8. The third peak appears in Figure 9.6 around $283\,\mathrm{cm}^{-1}$. This peak can also be modeled by a Lorentzian lineshape function and is related to the surface optical phonon mode (SO), as is explained in detail below. No peak corresponding to the typical WZ Raman mode is observed, which is supported by the lack of observable WZ segments in TEM images on the NWs.

Based on the Raman spectra, the the charge-carrier concentrations and mobilities are determined for four different samples of NWs having different nominal Be concentration (samples A, B, C and D). The experimental results are compared to the theoretical predictions in Figure 9.3 and summarized in Table 9.1.

	N^* $(10^{18}\,\mathrm{cm}^{-3})$	ω_P (cm^{-1})	N $(10^{18}\,\mathrm{cm}^{-3})$	Γ_P (cm^{-1})	μ (cm^2/Vs)
Sample A	1	98 ± 2	0.5 ± 0.2	1970 ± 150	12 ± 1
Sample B	15	315 ± 5	4.55 ± 0.18	1820 ± 120	14 ± 1
Sample C	35	320 ± 3	4.7 ± 0.8	1870 ± 80	13 ± 1
Sample D	46	327 ± 2	4.9 ± 0.8	2200 ± 20	11 ± 1

Table 9.1: nominal dopant concentration N^*, plasma frequency ω_P, effective charge carrier concentration N, plasma damping factor Γ_P, and mobility μ estimated by simulating the Raman Spectra from four samples (A, B, C, D), each with different nominal doping concentration.

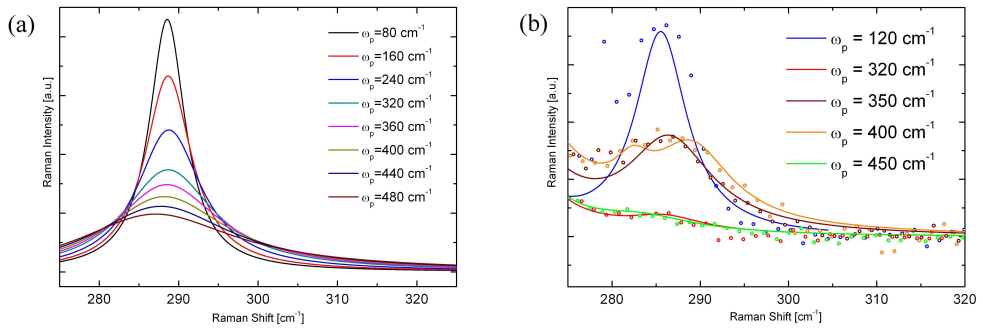

Figure 9.3: (a) simulation of the CPPM peak calculated for different plasma frequencies. (b) experimental spectra (points) are simulated (lines) according to (4) using different values for the plasma frequency. The intensity is normalized for every peak to the intensity of the TO mode. The theoretical trend shown in the right panel is also visible in the experimental spectra: for higher plasma frequency the CPPM peak is broadened and the maximum of the peak is red-shifted. For the simulation of these spectra it is sufficient to change the plasma frequency while the plasma damping factor does not change substantially as explained in the text.

As predicted by the theoretical treatment, the position and shape of the CPPM mode change for different doping concentrations (Figure 9.3a). Therefore, different values for the plasma frequency are needed to correctly reproduce the spectra (Figure 9.3b). The appearance of a single peak is characteristic of low-mobility charge carriers (holes), while for high-mobility charge carriers (electrons), the appearance of two peaks is expected[93, 94]. This experimental observation is consistent with the fact that Be is a p-type dopant in GaAs, as has been determined by Hall electrical measurements [88]. The SO phonon peak appears clearly in some spectra (see, for example, the orange line in Figure 9.3), while it is not evident in others. Whether or not the peak can be observed, depends on the NW surface morphology, as it will be discussed in the next section. The peak from the sample at lower charge-carrier concentration (sample A, blue points in Figure 9.3) is not reproduced by the CPPM as well as for the other samples. Rather than attributing this to shortcomings in the CPP model, this could be best attributed to phonon confinement [102, 103, 104, 105]. As already mentioned, the NWs belonging to this sample have very high twin-defects concentration with typical spacings between consecutive twins from 10 to 50 nm. This distance is small enough to lead to a confinement of the phonon in the axial direction of the NW. To the best author knowledge, there is no model available, that takes into account both phonon confinement and phonon-plasma coupling at the same time.

It should be noticed that all the spectra can be simulated with a plasma damping factor of approximately $1900\,\mathrm{cm}^{-1}$, corresponding to a charge-carrier mobility of around $13\,\mathrm{cm}^2/\mathrm{Vs}$. That the mobility does not change together with the charge-carrier concentration has been reported before [90] and explained as a saturation of the mobility that is expected to be observed at smaller values than for the bulk.

As it can be seen from Table 9.1, the charge-carriers concentration does not increase arbitrary with the nominal dopant concentration, but it saturates around $5 \cdot 10^{18}\,\mathrm{cm}^{-3}$, see Figure 9.4. For

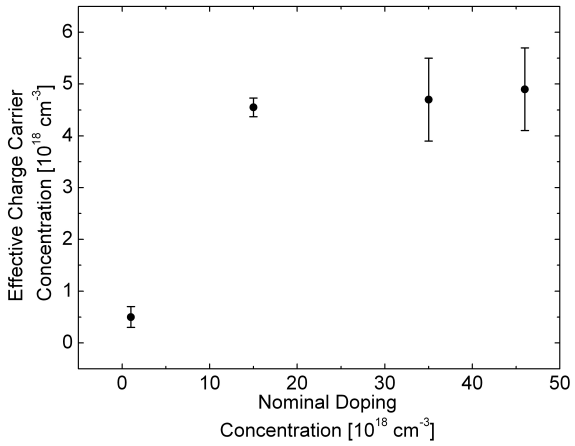

Figure 9.4: estimated charge carrier concentration in dependence of the nominal dopant concentration. The values are the same as those reported in Table 9.1.

sample A (lowest nominal concentration, see Table 9.1), the charge-carrier concentration as determined from the Raman spectra, is around 50% of the nominal dopant concentration, while for sample D (highest nominal concentration, see Table 9.1), the charge-carrier concentration is around only 9% of the nominal dopant concentration. This can be attributed to the different positions occupied by Be atoms within the GaAs lattice at different concentrations. Be diffuses in the GaAs lattice very efficiently [81] , substituting Ga atoms in the lattice (substitutional Be), serving as a p-type dopant [82, 84]. As the concentration of Be increases, the number of available Ga lattice sites decreases. At higher concentrations, Be can either form a Be-Be or Be-Ga complex or occupy the interstitial position inside the As-tetrahedron (interstitial Be) [82]. Be-Be and Be-Ga complexes have been observed in heavily Be-doped GaAs through resonant Raman scattering [91]. In the case of a complex formation, Be does not contribute to hole conduction [82]. When occupying the interstitial position inside the tetrahedron, Be should act as an n-type dopant. Consequently, the formation of both the Be-Be and Be-Ga complexes and of interstitial Be do not contribute to the p-type conductivity of the system. As a result, the effective dopant concentration saturates around $5 \cdot 10^{18}\,\mathrm{cm}^{-3}$.

Surface Phonons and Characterization of the Surface Conformation

In this section, the attention is focused on the appearance of the SO-phonons related peak and to its relation to the surface defects concentration. The surface propagation constant derived from the frequency of the SO mode (eq. 8.22), is compared with the defects distance extracted from TEM analysis. Raman spectra were measured for samples A, B and C (see Table 9.1), having different characteristic defects concentration. The aim of this comparison is to study the appearance of the SO-phonon modes for different defect density.

For a comparison between the analysis on the Raman and the TEM data, the dominating con-

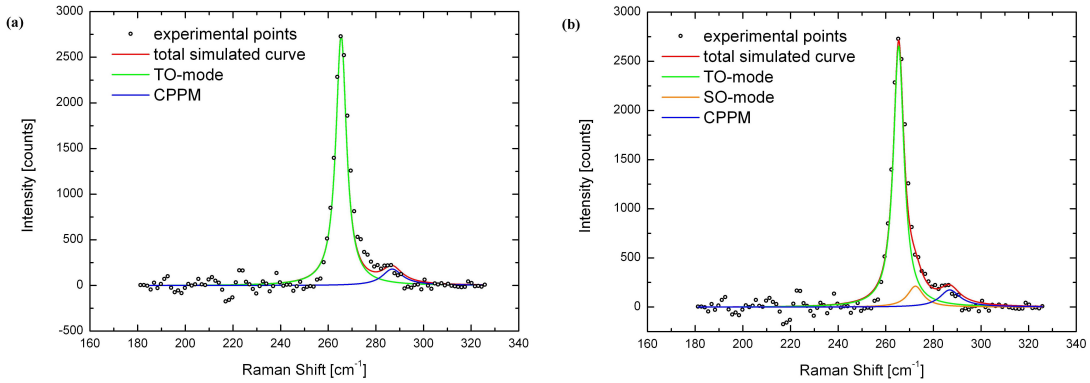

Figure 9.5: Typical Raman spectrum of the sample type A showing the TO mode and CPP related peak. (a) The experimental spectrum was simulated without including a SO phonon peak. (b) Shows a spectrum with a SO phonon peak included in the simulation centred at 273.5 cm^{-1}.

tribution to the Raman signal stems is consider to stem from the mid-section of the NW. First because it represents the largest part of the wire itself. Second, and more importantly, because the terminating parts have much higher defect concentrations, which prevents the observation of SO phonons (see the discussion below). For these reasons the attention is focus on the structure of the middle section of the NW. The length of the twin free segments (as seen in Figure 9.1) were measured. The paired twin forms a zig-zag pattern which causes a perturbation on the surface of the NW (see inset of Figure 9.1b). For statistical purposes the paired twin (i.e a twin lamella) was considered as a single defect. Single twins and paired twins are equivalently considered. The distance used to estimate the average distance between defects can be then measured as the distance between single-single, double-double or single-double twins. The twin distances were measured using the line intercept method from the TEM images.

In this section the samples A, B and C are taken into consideration, because they present a different and exemplar defect concentrations. In the following discussion, the samples are ordered from the less defective (sample C) to the more defective (sample A). For sample C, small fractions of twin defects were observed and the average distance between them were measured to be $1.6 \pm 0.5\,\mu$m. NWs belonging to sample B reveal the presence of higher number of twins compared to the wires in sample type C. The average distance between them were measured to be 600 ± 100 nm. The NWs belonging to sample A, are heavily twinned and substantially smaller average twin spacing of 10-50 nm can be observed.

A typical Raman spectrum for the NWs of sample C with a low defect density is given in Figure 9.5. The peaks at a frequency of 268 cm^{-1} and at a frequency of 288 cm^{-1} correspond to the TO phonon mode and CPP model respectively. The spectra have been simulated with and without including the SO phonon peak as shown in Figure 9.5. As it can be seen from Figure 9.5, including the SO phonon peak centered at 273.5 cm^{-1} allows for a better simulation of the middle part of the spectrum where the SO peak is visible as a shoulder of the CPP peak. According to eq. (8.22), such a frequency would correspond to a spatial period of 1620 nm. The spatial period L is calculated from the surface propagation constant q, as $L = \frac{2\pi}{q}$. The surface propagation constant

is estimated from the SO frequency extracted from the Raman spectrum, according to eq. (8.22). For this etimation, a radius of 67.5 nm is considered, corresponding to the half of the lateral dimension of these NWs. In estimating the SO frequency it is critical to correctly consider the dielectric constant of the surrounding medium. In backscattering geometry an angle of 138° can be collected (corresponding to a numerical aperture of 1.4). The lateral section of the NW is hexagonal and it can be imagined that just one surface lays on the glass, corresponding to an angle of 60°. So a fraction of 0.565 of the collected light comes from the air-wire interface while a fraction of 0.435 comes from the glass-wire interface. For the calculation therefore an effective dielectric constant is used, estimated as: $\epsilon_{eff} = 0.565\epsilon_{air} + 0.435\epsilon_{glass}$. Repeated optical measurements on different wires belonging to this sample gave an average SO frequency of $274.1 \pm 0.9\,\mathrm{cm}^{-1}$, corresponding to a decay length of $1.47 \pm 0.47\,\mu$m which is in close agreement to the average distance of $1.6 \pm 0.5\,\mu$m measured between consecutive twins from TEM images.

A typical experimental Raman spectrum for the sample type B is given in the Figure 9.6. In Figure 9.6a the spectrum where no SO phonon peak is included in the simulation to fit the experimental data shows that the CPP peak reproduces the slope on the right but does not reproduce the middle part of the spectrum. In Figure 9.6b the CPP parameters are modified in order to shift the CPP peak to a lower frequency. It is evident that, shifting the maximum of the peak to smaller energies, the slope of the peak cannot be reproduced anymore. In order to correctly simulate the spectrum as shown in Figure 9.6c, one needs to include a third peak that is attributable to SO phonons, being the CPP related peaks alone not sufficient to correctly reproduce the shape of the second peak. From the simulation of several spectra similar to that in Figure 9.6, the SO-frequency was extracted for different NWs as done for sample type C. A mean value of $284.3 \pm 0.4\,\mathrm{cm}^{-1}$ is found for the SO frequency, which corresponds to a mean value of $446 \pm 35\,$nm for the spatial period. The spatial period is obtained in this case using a radius of 60 nm, estimating the dielectric constant ϵ as before. As in the case of low twin density NWs, the phonon decay length measured from the Raman spectra agrees well with the range of the average distance of $600 \pm 100\,$nm between twins observed from our TEM data.

The NWs belonging to sample A on the other hand have a high concentration of twins (about 10-50 nm twin spacing). For this sample, the SO phonon peak is not observable. The absence of the SO phonon peak in this sample can be attributed to the high density of defects and their SO phonon propagation translates to a very small decay length. In this case, the SO phonon frequency shifts to the CPP mode frequency (see Figure 9.7) and thus cannot be distinguished.

The calculated SO phonon frequency as a function of the spatial period of the surface oscillation is derived from eq. (8.22) is shown in Figure 9.7. The SO phonon frequency varies from the LO phonon frequency to the TO phonon frequency (upper and lower dashed line respectively). The circles indicate the values for the SO phonon frequency corresponding to the estimated propagation constants in the different sample types. The three lines are calculated taking into account for the different lateral dimension of the NWs. The blue circle corresponds to the sample A where spatial period for the oscillation in the axis direction of around 20 nm was estimated, the related SO phonon frequency would be around 288 cm^{-1}, too close to the CPPM frequency to be observed as independent peak. The green circle corresponds to the sample B, where a spatial period of $446 \pm 35\,$nm nm leads to an observable SO phonon peak around 283 cm^{-1}. The magenta circle corresponds to the sample type C, where a spatial period of $1.47 \pm 0.47\,\mu$m was estimated. In this

case the SO phonon frequency observed around 273.5 cm^{-1} is very close to the TO phonon peak. Nonetheless, a SO phonon related peak is still observable as a shoulder of the TO phonon peak.

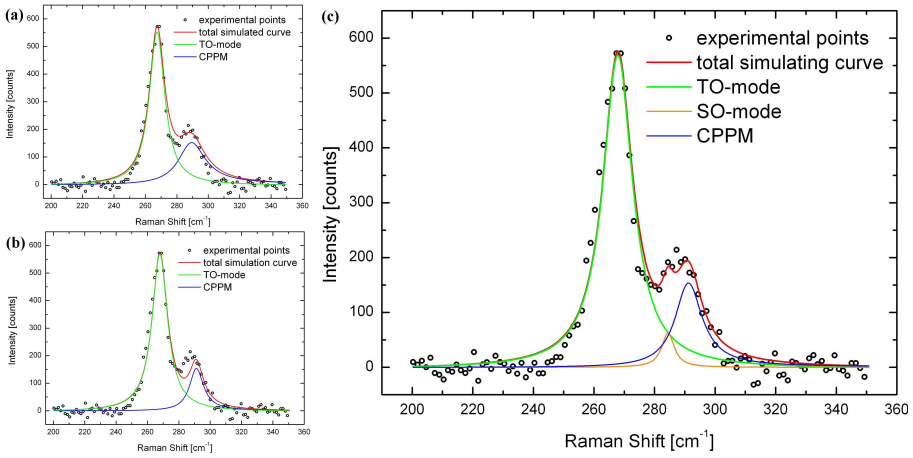

Figure 9.6: Raman spectrum showing TO, SO and CPPM peaks obtained from the sample type B. (a) and (b) show, besides the experimental data the simulated spectra obtained without including the SO phonon peak. (c) shows the simulated spectrum where the third peak is attributed to the SO phonons is included, in order to correctly reproduce the experimental spectrum. See text for further explanation.

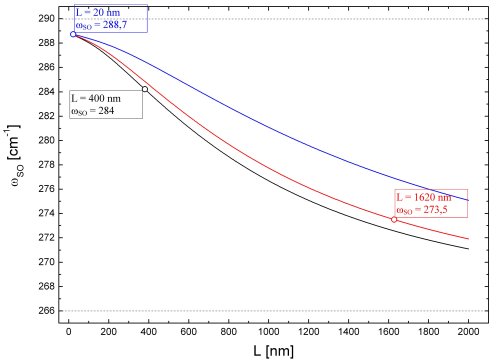

Figure 9.7: SO frequency calculated in dependence on the spatial period of the surface oscillation along the axis direction. The calculation is repeated considering the different diameters for the different NWs. The circles represent a characteristic value for the SO-frequency. The lower and upper dashed black line represents the TO and LO frequency, respectively

Conclusions

For doped NWs, the effective dopant concentration and the resulting charge-carrier concentration are key quantities for possible technological applications. However these quantities are difficult to be accurately determined. In this work, we investigated the structural and electrical transport properties of Be-doped GaAs NWs. To determine the charge-carrier concentration, Raman spectroscopy was applied as a contactless technique, which also allows for an independent estimation of the charge-carrier mobility. By repeating the experiment for four different NWs samples, having different nominal Be concentration, it was found that the resulting charge-carrier density does not scale linearly with the nominal dopant concentration but rather saturates around $5 \cdot 10^{18}\,\mathrm{cm}^{-3}$. This behaviour can be attributed to the filling of free Ga sites and the formation of Be-Be and Be-Ga complexes at higher Be concentration.

Also the characterization of the surfacestructure can be performed by Raman spectroscopy. The spatial period of the SO phonons oscillation along the NW axis was correlated with the distance between the twin defects measured by TEM. The SO surface propagation constant for the NWs from the sample with lower defect density and moderate defect density were found to be $1.47 \pm 0.47\,\mu$m and $446 \pm 35\,$nm, respectively. These values are in good agreement with the average distance between the tein defects of about $1.6 \pm 0.5\,\mu$m and $600 \pm 100\,$nm as revealed by TEM. On the other hand, for the sample where no SO-phonon peak was measured in the Raman spectra, a defect spacing of 10-50 nm was found by TEM analysis. Such a short surface propagation constant prevents the observation of a separate SO-phonon peak, consistently with the theory.

SUMMARY

In this thesis, Raman spectroscopy has been used to characterize the interaction between a charge density and the lattice vibration of a solid state material. Two systems have been analyzed: the first composed of a metallic nanostructure and a carbon material (carbon nanotubes and graphene); the second consisting of beryllium-doped gallium arsenide nanowires, where the charge-carriers provided by the dopant act as a plasma, interacting with the local field related to the longitudinal phonon mode of the crystal lattice.

For the first system it has been experimentally shown that the interaction between the localized surface plasmon-polariton related to the metallic nanostructure and the lattice vibration, leads to a non-linearity of the Raman response in dependence on the laser power. The occurrence of this non-linearity has been compared with a theoretical model, developed within a quantum-electrodynamic description of the coupled system. This theoretical prediction and the experimental results are in good agreement. It has been shown, that the appearance of the non-linearity depends on several parameters, like the matching between the laser and plasmon resonance frequency, the plasmon damping factor and the vibrational properties of the Raman scatterer. The comparison between the experimental results and the prediction deriving from a stimulated Raman picture is less successful. For a fully satisfying comparison between theory and experiment however, the plasmonic properties related to the metallic nanostructure need to be determined with high precision.

For the second system, the interaction between the charge carriers and the local field related to the lattice vibration of the longitudinal optical phonon mode leads to a change in width and position of the corresponding peak in the Raman spectrum. Thank to this change, the charge-carrier concentration and mobility can be estimated. This estimation follows from the coupled-plasma-phonon model. Together with the coupling of plasma and longitudinal phonons, also the appearance of surface phonons has been observed. The frequency of the surface optical phonons has been correlated with the mean defect distance along the nanowire radius, extracted from electron transmission microscopy measurements.

Bibliography

[1] Raman, C.V. "A new radiation". *Indian J. Phys.* 2, 387398 (1928).

[2] A. Zoubir "Raman Imaging" Springer Series in Optical Sience 168 (2012).

[3] E.O. Potman and S. Mukamel "Theory of Coherent Raman Spectroscopy" in "Coherent Raman Scattering Microscopy" CRC Press (2013).

[4] Robert W. Boyde "Non-linear Optics" Elsevier (R) (2007).

[5] "Nanoimaging with Optical Antennas" in "Optical Antennas" Cambridge University Press (2013).

[6] J.-C. Valmalette "Tip-Enhanced Raman Spectroscpy: Principle and Instrumentation" in "Handbook of Enhanced Spectroscopy" Pan Stanford Publishing (2016).

[7] C. Kittel "Introduction to Solid State Physics" Wiley (2006).

[8] J.-C. Charlier, P.C. Eklund, J. Zhu, A.C. Ferrari "Electron and Phonon Properties of Graphene: Their Relationship with Carbon Nanotubes" in "Carbon Nanotubes" Topics in Applied Physics 111, Spinger (2008)

[9] S. Reich, C. Thomsen, J. Mautzsch "Carbon Nanotubes" Wiley (2008).

[10] S. Reich and R. Narula "Double resonant Raman spectra in graphene and graphite: A two-dimensional explanation of the Raman amplitude" *Phys. Rev. B* 78 165422 (2008)

[11] J.S. Parka, A.R. Reinab, R.J. Saito, J. Kongc, G.M.S. Dresselhaus and M.S. Dresselhaus "G' band Raman spectra of single, double and triple layer graphene" . *Carbon* 47 13031310 (2009).

[12] P. Venezuela, M. Lazzeri and F. Mauri "Theory of double-resonant Raman spectra in graphene: Intensity and line shape of defect-induced and two-phonon bands" *Phys. Rev. B* 84 035433 (2011).

[13] P. Klar, E. Lidorikis, A. Eckmann, I.A. Verzhbitskiy, A.C. Ferrari and C. Casiraghi "Raman scattering efficiency of graphene" *Phys. Rev. B* 87 205435 (2013)

[14] H. Budde, N. Coca-López, X. Shi, R. Ciesielski, A. Lombardo, D. Duhee Yoon, A.C. Ferrari and A. Hartschuh, *ACS Nano*, 10 2 17561763 (2016)

[15] I. Zardo, S. Conesa-Boj, F. Peiro, J.R. Morante, J. Arbiol, E. Uccelli, G. Abstreiter and A. Fontcuberta i Morral "Raman spectroscopy of wurtzite and zinc-blende GaAs nanowires: Polarization dependence, selection rules, and strain effects" *Phys. Rev. B* 80 245324 (2009).

[16] N.V. Petrova and I.N. Yakovkin "DFT calculations of phonons in GaAs with zinc blende and wurtzite structures" *Phys. Status Solidi B* 250 10, 21412144 (2013).

[17] R. Beams, R.L. Cancado and L. Novotny "Raman characterization of defects and dopants in graphene" *J. Phys. Condens. Matter* 27 083002 (2015)

[18] A.C. Ferrari and D.M. Basko "Raman spectroscopy as a versatile tool for studying the properties of graphene" *Nature Nanotec.* 8 235 (2013)

[19] http://www.optoscience.com/maker/nkt/crystalfiber/

[20] S.D. Costa, A. Righi, C. Fantini, Y. Hao, C. Magnuson, L. Colombo, R.S. Ruoff, M.A.Pimenta "Resonant Raman spectroscopy of graphene grown on copper substrates" Solid State Comm. 152 13171320 (2012)

[21] R. Saito, C. Fantini, J. Jiang "Excitonic States and Resonance Raman Spectroscopy of Single-Walled Carbon Nanotubes" in "Carbon Nanotubes" Topics in Applied Physics 111, Spinger (2008).

[22] N. Mauser and A. Hartschuh "Tip-enhanced near-field optical microscopy" *Chem. Soc. Rev.* 42, 1248 (2014).

[23] N. Mauser and A. Hartschuh "Tip-Enhanced Raman Spectroscopy: Application to Carbon Materials" in "Handbook of Enhanced Spectroscopy" Pan Stanford Publishing (2016).

[24] C. Georgi, PhD Thesis at LMU "Exciton Mobility and Localized Defects in Single Carbon Nanotubes Studied with Tip-Enhanced Near-Field Optical Microscopy" (2010).

[25] K. Karrai and I. Tiemann "Interfacial Shear Force Microscopy" Phys. Rev. B 62 19 (2000).

[26] B.C. Stipe H.J. Mamin T.D. Stowe T.W. Kenny and D. Rugar "Non-contact Friction and Force Fluctuations between closely Spaced Bodies".

[27] C. Georgi, A. Hartschuh, "Tip-enhanced Raman spectroscopic imaging of localized defects in carbon nanotubes", *Appl. Phys. Lett.* 97, 143117 (2010). C. Georgi, A.A. Green, M.C. Hersam, A. Hartschuh, "Probing Exciton Localization in Single-Walled Carbon Nanotubes Using High-resolution Near-field Microscopy", *ACS Nano*, 4, 5914 (2010).

[28] N. Rauhut, M. Engel, M. Steiner, R. Krupke, P. Avouris, and A. Hartschuh, "Antenna-Enhanced Photocurrent Microscopy on Single-Walled Carbon Nanotubes at 30 nm Resolution", *ACS Nano* 6, 6416 (2012).

[29] N. Mauser, N. Hartmann, M.S. Hofmann, J.Janik, A. Hogele and A. Hartschuh, "Antenna-Enhanced Optoelectronic Probing of Carbon Nanotubes", *Nano Lett.* 14, 3773 (2014)

[30] R. Zhang, Y. Zhang, Z.C. Dong, S. Jiang, C. Zhang, L.G. Chen, L. Zhang, Y. Liao, J. Aizpurua, Y. Luo, J.L. Yang and J.G. Hou "Chemical mapping of a single molecule by plasmon-enhanced Raman scattering" Nature 498 6 82 (2013).

[31] S. Jiang, Y. Zhang, R. Zhang, C. Hu, M. Liao, Y. Luo, J. Yang, Z. Dong and J.G. Hou Distinguishing adjacent molecules on a surface using a plasmon-enhanced Raman scattering, *Nature Nanotech.* 10, 865-869 (2015).

[32] M. Liao, S. Jiang, C. Hu, R. Zhang, Y. Kuang, J. Zhu, Y. Zhang, and Z. Dong "Tip-Enhanced Raman Spectroscopy Imaging on Individual Carbon Nanotubes with Subnanometer Resolution" *Nano Lett.* ASAP (2016).

[33] J.M. Atkin M.B. and Raschke Optical spectroscopy goes molecular, *Nature* 498, 44 (2013).

[34] W. Zhu and K.B. Crozier, "Quantum mechanical limit to plasmonic enhancement as observed by surface enhanced Raman scattering", *Naure Comm.* 5, 5228 (2014).

[35] R.C. Monreal, T.J. Antosiewicz, S. Apell "Surface scattering contribution to the plasmon width in embedded Ag nanospheres" *New J. Phys.* 15, 083044 (2013).

[36] C.F.A. Negre, E.M. Perassi, E.A. Coronado, C.G. Sánchez "Quantum dynamical simulations of local field enhancement in metal nanoparticles " *Phys. Condens. Mater* 25 125304 (2013).

[37] P.J. Feibelman "Microscopic calculation of electromagnetic fields in refraction at a jellium-vacuum interface" *Phys. Rev. B* 12 1319-1336 (1975).

[38] A. Leibisch and W.L. Schaich "Influence of a polarizable medium on the nonlocal optical response of a metal surface" *Phys. Rev. B* 52, 14219-14234 (1995).

[39] D.C. Marinica, A.K. Kazansky, P. Nordlander, J. Aizpurua, and A.G. Borisov "Quantum Plasmonics: Nonlinear Effects in the Field Enhancement of a Plasmonic Nanoparticle Dimer", *Nano Lett.* 12 1333 (2012).

[40] M. Barby, P. Koval, F. Marchesin. R. Esteban, A.G. Borisov, J. Aizpurua, and D. Sànchez-Portal "Atomistic Near-Field Nanoplasmonics: Reaching Atomic-Scale Resolution in Nanooptics", *Nano Lett.* 15 3410 (2015).

[41] T.V. Teperik, P. Nordlander, J. Aizpurua and A.G. Borisov "Quantum Effects and Nonlocality in strongly coupled plasmonic Nanowires Dimers", *Opt. Expr.* 21 22 27306 (2013).

[42] K.J. Savage, M. Hawkeye, R. Esteban, A.G. Borisov, J. Aizpurua and J.J. Baumberg "Revealing the Quantum Regime in tunneling Plasmonics", *Nature* 491 574 (2012).

[43] R. Estaban, A.G. Borisov, P. Nordlander and J. Aizpurua "Bridging quantum and classical plasmonics with a quantum-correlated model", *Nature Comm.* 10 1038 (2012).

[44] P. Reolli, C. Galland, N. Piro, T.J. Kippenberg "Molecular Cavity Optomechanics as a Theory of Plasmon-Enhanced Raman Scattering" *Nature Nanotech.* 11 164169 (2016).

[45] M.K. Schmidt, R. Esteban, A. Gonzalez-Tudela, G. Giedke and J. Aizpurua "Quantum Mechanical Description of Raman Scattering from Molecules in Plasmonic Cavities" *ACS Nano* ASAP (2016).

[46] A.D. McFarland, M.A. Young, J.A. Dieringer and R.P. Van Duyne "Wavelength Scanned Surface Enhanced Raman Excitation Spectroscopy", *J. Phys. Chem.* 109, 11279 (2005).

[47] L. Novotny and B. Hecht "Priciples of Nanooptics" Cambridge University Press (2006).

[48] L.Novotny and N. van Hulst, "Antennas for Light" *Nature Photonics* 5, 8390 (2011).

[49] R. Esteban and J. Aizpurua "Optical antennas for Field-Enhanced Spectroscopy" in "Optical Antennas" Cambridge University Press (2013).

[50] L. Novotny and C. Hafner "Light propagation in a cylindrical waveguide with a complex, metallic, dielectric function" *Phys. Rev. E* 50 4094-4106 (1994).

[51] J.P. Camden, J.A. Dieringer, Y. Wang, D.J. MAsiello, L.D. Marks, G.C.Scahtz and R.P. van Duyne "Probing the structure of Single-Molecule Surface Anhanced Raman Scattering Hot Spots" *J. Am. CHem. Soc.* 130 12616-12617 (2008).

[52] K. KNeipp, Y. Wang, H. Kneipp, L.T. Perrelmann, I. Itzkan, R.R. Dasari and M.S. Feld "Single Molecule Detection using Surface Enhanced Raman Scattering" *Phys. Rev. Lett.* 78 9 (1997).

[53] A. Owyoung "Sensitivity Limitation for CW Stimulated Raman Sectroscopy" *Opt. Commun.* 22 323-328 (1977).

[54] P. Kukura D.W. McCamant, R.A. Mathies, "Femtosecond stimulated Raman spectroscopy" *Annu. Rev. Phys. Chem.* 58 461 (2007).

[55] C.W. Freudiger, W. Min, B.G. Saar, S. Lu, G.R. Holtom, C. He, J.C. Tsai, J.X. Kang, X.S. Xie "Label-Free Biomedical Imaging with High Sensitivity by Stimulated Raman Scattering Microscopy" *Science* 322 (2008).

[56] T.J. Kippenberg, H. Rokhsari, T. Carmon, A. Scherer and K.J. Vahala "Analysis of Radiation Pressure Induced Mechanical Oscillation of an Optical Microcavity" *Phys. Rev. Lett.* 95 033901 (2005).

[57] S.-Y. Lee, D. Zhang, D.W. McCamant, P. Kukura, R.A. Matheis "Theory of femtosecond stimulated Raman spectroscopy" *J. of Chem. Phys.* 121 8 (2004).

[58] J.T. Hugall and J.J. Baumberg "Demonstrating Photoluminescence from Au is Electronic Inelastic Scattering of a Plasmonic Metal: The Origin of SERS Backgruonds" *Nano Lett.* 15 2600-2604 (2015)

[59] C. Francau and S. Astilean "Surface Enhanced Raman Scattering: Fundamental and Biosensing Application" in "Handbook of Plasmon Enhanced Spectroscopies" (2015).

[60] I. Wilson-Rae, N. Nooshi, W. Zwerger and T.J. Kippenberg "Theory of Ground State Cooling of a Mechanical Oscillator Using Dynamical Backaction" *Phys. Rev. Lett.* 99 093901 (2007).

[61] T.J. Kippenberg and K.J. Vahala "Cavity Optomechanics" *Opt. Express* 15 25 17172 (2007).

[62] C.K. Law "Interaction between a moving mirror and a radiation pressure: a Hamiltonian Formulation." *Phys. Rev. A* 51 2537-2541 (1995).

[63] T.J. Kippenberg, H. Rokhsari, T. Carmon, A. Scherer, and K.J. Vahala "Analysis of Radiation-Pressure Induced Mechanical Oscillation of an Optical Microcavity" *Phys. Rev. Lett.* 95 033901 (2005)

[64] M. Asplemmeyer, T.J. Kippenberg, F. Marquardt "Cavity Optomechanics" , *Rev. of Modern Physics* 86 (2014)

[65] A.A. Clerk, M.H. Devoret, S.M. Girvin and F. Marquardt "Introdduction to Quantum Noise Measurement an Amplification" *Rev. of Modern Physics* 82 (2010)

[66] F. Marquardt, J.P. Chen, A.A. Clerk and S.M. Girvin "Quantum Theory of Cavity Assisted Sideband Cooling of Mechanical Motion" *Phys. Rev. Lett.* 99 093902 (2007)

[67] N. Mauser, D. Piatkowski, T. Mancabelli, M. Nyk, S. Mackowski, and A. Hartschuh "Tip-Enhancement of Up-Conversion Photoluminescence from Rare-Earth Ion Doped Nanocrystals", *ACS Nano* 9, 3617 (2015)

[68] U. Hohenester and A. Trügler, "MNPBEM - A Matlab toolbox for the simulation of plasmonic nanoparticles; " *Comp. Phys. Commun.* 183 370 (2012).

[69] U. Hohenester, "OCTBEC - A Matlab toolbox for optimal quantum control of Bose-Einstein condensates" *Comp. Phys. Commun.* 185, 1177 (2014).

[70] J. Waxenegger, A. Trügler and U. Hohenester, "Plasmonics simulations with the MNPBEM toolbox: Consideration of substrates and layer structures" *Comp. Phys. Commun.* 193, 138 (2015).

[71] P. Krogstrup, H. I. Jorgensen, M. Heiss, O. Demichel, J.V. Holm, M. Aagesen, J. Nygard and A. Fontcuberta i Morral, "Single-nanowire solar cells beyond the ShockleyQueisser limit" *Nat. Photonics* 7, 306-310 (2013). J. Svensson, A.W. Dey, D. Jacobsson, and L.- E. Wernersson, "IIIV Nanowire Complementary MetalOxide Semiconductor Transistors Monolithically Integrated on Si" *Nano Lett.* 15 12, 78987904 (2015).

[72] P.K. Mohseni, A. Behnam, J.D. Wood, C.D. English, J.W. Lyding, E. Pop, X. Li "In_xGa_1xAs Nanowire Growth on Graphene: van der Waals Epitaxy Induced Phase Segregation" *Nano Lett.* 13 3 1153-1161 (2013).

[73] Y. Wang, Y. Zhang, D. Zhang, S. He and X. Li "Design High-Efficiency IIIV Nanowire/Si Two-Junction Solar Cell " *Nanoscale Research Letters* 269 10 (2015).

[74] J. Wallentin, N. Anttu, D. Asoli, M. Huffman, I. Aberg, M. H. Magnusson, G. Siefer, P. Fuss-Kailuweit "InP nanowire array solar cells achieving 13.8% efficiency by exceeding the ray optics limit" *Science* 339 1057-1060 (2013).

[75] Y.-C. Chou, K- Hillerich, J. Tersoff, M.C. Reuter, K.A. Dick and F.M. Ross "Atomic-Scale Variability and Control of III-V Nanowire Growth Kinetics" *Science* 343 281 284 (2014).

[76] A.C. Farrell, W.-J. Lee, P. Senanayake, M.A. Haddad, S.V. Prikhodko and D.L. Huffaker "High-Quality InAsSb Nanowires Grown by Catalyst-Free Selective-Area MetalOrganic Chemical Vapor Deposition" *Nano Lett.* 15 10 66146619 (2015)

[77] D. Pan, M. Fu, X. Yu, X. Wang, L. Zhu, S. Nie, S.Wang, Q. Chen, P. Xiong, S. von Molnr and J. Zhao "Controlled Synthesis of Phase-Pure InAs Nanowires on Si(111) by Diminishing the Diameter to 10 nm" *Nano Lett.*, 14 3 1214-1220 (2014).

[78] E. Gil, V.G. Dubrovskii, G. Avit, Y. Andr, C. Leroux, K. Lekhal, J. Grecenkov, A. Trassoudaine, D. Castelluci, G. Monier, R.M. Ramdani, C. Robert-Goumet, L. Bideux, J.C. Harmand and F. Glas "Record Pure Zincblende Phase in GaAs Nanowires down to 5 nm in Radius" *Nano Lett.* 14 7 39383944 (2014).

[79] V.G. Dubrovskii, T. Xu, A. Daz lvarez, S.R. Plissard, P. Caroff, F. Glas, B. Grandidier "Self-Equilibration of the Diameter of Ga-Catalyzed GaAs Nanowires" *Nano Lett.* 15 5580 (2015).

[80] P. Krogstrup, R. Popovitz-Biro, E. Johnson, M. H. Madsen, J. Nygrd, and H. Shtrikman, "Structural Phase Control in Self-Catalyzed Growth of GaAs Nanowires on Silicon (111)" *Nano Lett.* 10, 4475 (2010).

[81] A. Casadei, P. Krogstrup, M. Heiss, J.A. Rohr, C. Colombo, T. Ruelle, S. Upadhyay, C.B. Sorensen, J. Nygard and A. Fontcuberta i Morral, "Doping incorporation paths in catalyst-free Be-doped GaAs nanowires" *Appl. Phys. Lett.* 102, 013117 (2013).

[82] H.-P. Komsa, E. Arola, J. Pakarinen, C.S. Peng and T. Rantala, "Beryllium doping of GaAs and GaAsN studied from first principles" *Phys. Rev. B* 79 115208 (2009).

[83] N. Ohtsuka, K. Kodama, M. Ozeki and Y. Sakuma, "Extremely high Be doping of InGaAs by low-temperature atomic layer epitaxy" *J. Crystal Growth* 115 460 (1991).

[84] C.G. Van de Walle, S. Limpijumnong and J. Neugebauer "First-principles studies of beryllium doping of GaN" *Phys. Rev. B* 63 245205 (2001).

[85] D. L. Dheeraj, A. M. Munshi, O. M. Christoffersen, D. C. Kim, G. Signorello, H. Riel, A. T. J. van Helvoort, H. Weman, B. O. Fimland "Comparison of Be-doped GaAs nanowires grown by Au- and Ga-assisted molecular beam epitaxy" *J. of Crystal Growth* 378 532-536 (2013).

[86] J.L. Boland, S. Conesa-Boj, P. Parkinson, G. Tütüncüoglu, F. Matteini, D. Rffer, A. Casadei, F. Amaduzzi, F. Jabeen, C.L. Davies, H.J. Joyce, L.M. Herz, A. Fontcuberta i Morral, and M.B. Johnston "Modulation Doping of GaAs/AlGaAs CoreShell Nanowires With Effective Defect Passivation and High Electron Mobility" *Nano Lett.* 15, 13361342, (2015).

[87] H.J. Joyce, P. Parkinson, N. Jiang, C.J. Docherty, Q. Gao, H.H. Tan, C. Jagadish, L.M. Herz, and M.B. Johnston "Electron Mobilities Approaching Bulk Limits in Surface-Free" GaAs Nanowires" *Nano Lett.*, 14, 59895994, (2014).

[88] M.J. Tejwan, H. Kanber, B.M. Paine, and J.M. Whelen "Growth and diffusion of abrupt berylliumdoped profiles in gallium arsenide by organometallic vapor phase epitaxy " *Appl. Phys. Lett.* 53 2411 (1988).

[89] S.K. Ojha, P.K. Kasanaboina, C.L. Reynolds Jr., T.A. Rawdanowicz, Y. Liu, R-.M. White and S. Iyer "Incorporation of Be dopant in GaAs core and coreshell nanowires by molecular beam epitaxy" *J. Vac. Sci. Technol. B* 34, 02L114 (2016).

[90] B. Ketterer, E. Uccelli and A. Fontcuberta i Morral, "Mobility and carrier density in p-type GaAs nanowires measured by transmission Raman spectroscopy" *Nanoscale*, 4 1789 (2012).

[91] M. Hilse, M. Ramsteiner, S. Breuer, L. Geelhaar, and H. Riechert "Incorporation of the dopants Si and Be into GaAs nanowires" *Appl. Phys. Lett.* 96 193104 (2010).

[92] M.V. Klein and B. Ganguly "Theoretical and expermental Study of Raman Scattering from coupled LO-Phonon-Plasmon Modes in Silicon Carbide" *Phys. Rev. B* 6 2380 (1972).

[93] G. Irmer, V.V. Toporov, B.H. Bairamov and J. Monecke "Determination of the Charge Carrier Concentration and Mobility in n-GaP by Raman Spectroscopy" Phys. Stat. Sol. B 119, 595 (1983).

[94] G. Irmer, M. Wenzel and J. Moneke "Light Scattering by a Multicomponent Plasma coupled with longitudinal-ooptical Phonons: Raman Spectra of p-type GaAs:Zn" *Phys. Rev. B* 56 15 9524 (1997).

[95] D. Isheim, J. Kaszpurenko, D. Yu, Z. Mao, D. Seidman and I. Arslan "3D Atomic-Scale Mapping of Manganese Dopants in Lead Sulfide Nanowires" *Journal of Phys. Chem. C* 116, 6595-6600, (2012).

[96] T. Dennenwaldt, J. Ciston, U. Dahmen, W.- Y.Ching, F.J. Pucher, W. Schnick, and C. Scheu, "High-resolution spectroscopy of bonding in a novel BeP_2N_2 compound." *Microsc. Microanal.* 20 3 664670 (2014).

[97] K.G. Pradeep, G. Herzer, P. Choi and D. Raabe "Atom probe tomography study of ultrahigh nanocrystallization rates in FeSiNbBCu soft magnetic amorphous alloys on rapid annealing" *Acta Mater.*, 68 295-309 (2014).

[98] O. Moutanabbir, D. Isheim, H. Blumtritt, S. Senz, E. Pippel, and D. N. Seidman "Colossal injection of catalyst atoms into silicon nanowires" *Nature* 496, 78 (2013).

[99] S.P.S. Porto, J.A. Giordmaine and T.C. Damen "Depolarization of Raman Scattering in Calcite" *Phys. Rev.* 2 147 (1966).

[100] N.V. Petrova and I.N. Yakovnik "DFT calculations of phonons in GaAs with zinc blende and wurtzite structures" *Phys. Status Sol. B* 250 10 2141 (2013).

[101] S.V. Karpov, B.V. Novikov, M.B. Smirnov, V. Yu, A. Davydov, N. Smirnov, I.V. Shtrom, G.E. Cirlin, A.D. Bouravleuv, B. Samsonenko "Specific features of Raman spectra of IIIV nanowhiskers" *Physics of the Solid State* 53 7 1431 (2011).

[102] C.G. Núñez, A.F. Braña, J. L. Pau, D. Ghita, B. J. García, G. Shen, D. S. Wilbert, S. M. Kim, and P. Kung "Surface optical phonons in GaAs nanowires grown by Ga-assisted chemical beam epitaxy" *J. of Appl. Phys.* 115 034307 (2014).

[103] I.H. Campbell and P.M. Fauchet "The effects of microcrystal size and shape on the one phonon Raman spectra of crystalline semiconductors" *Solid State Comm.* 58 10 739 (1986).

[104] H. Richter Z.P. Wang and L. Ley "The one phonon Raman spectrum in microcrystalline silicon" *Solid State Comm.* 39 625 (1981).

[105] S. Piscanec, M. Cantoro, A.C. Ferrari, J.A. Zapien, Y. Lifshitz, S.T. Lee, S. Hofmann and J. Robertson "Raman spectroscopy of silicon nanowires" *Phys. Rev. B* 68 241312 (2003).

[106] J. Biellmann, B. Prevot and C. Schwab "First-order Raman line intensity ratio in GaAs: A potential lattice perfection scale" J. Phys. C: Solid State Phys., 16 1135 (1983).

[107] L.Z. Liu, J. Wang, X.L. Wu, T.H. Li and P.K. Chu "Longitudinal optical phononplasmon coupling in luminescent 3CSiC nanocrystal films" *Opt. Lett.* 35 23 4024 (2010).

[108] P. Krogstrup, R. Popovitz-Biro, E. Johnson, M. H. Madsen, J. Nygard, and H. Shtrikman "Structural Phase Control in Self-Catalyzed Growth of GaAs Nanowires on Silicon (111)" *Nano Lett.* 10, 4475 (2010).

[109] F. Matteini, V.G. Dubrovskii, D.Rüffer, G. Tütüncügolu, Y. Fontana and A.F.I. Morral "Tailoring the diameter and density of self-catalyzed GaAs nanowires on silicon" *Nanotechnology* 26, 105603 (2015).

[110] M. Koguchi, H. Kakibayashi, M. Yazawa, K. Hiruma, and T. Katsuyama "Crystal Structure Change of GaAs and InAs Whiskers from Zinc-Blende to Wurtzite Type" *Japanese Journal of Applied Physics* 31, 2061 (1992).

[111] D. Jacobsson, F. Panciera, J. Terso. M.C. Reuter, S. Lehmann, S. Hofmann, K.A. Dick and F.M. Ross "Interface dynamics and crystal phase switching in GaAs nanowires" *Nature* 532 317 (2016).

[112] P. Caroff, K.A. Dick, J. Johansson, M.E.Messing, K. Deppert and L. Samuelson "Controlled polytypic and twin-plane superlattices in iiiv nanowires" *Nat. Nanotech.* 4 50 (2009).

[113] C.-Y. Yeh, Z.W. Lu, S. Froyen and A. Zunger, "Zinc-blendewurtzite polytypism in semiconductors" *Phys. Rev. B* 46, 10086 (1992).

[114] R.E. Algra, M.A. Verheijen, L.-F. Feiner, G.G.W. Immink, R. Theissmann, W.J.P. van Enckevort, E.Vlieg and E.P.A.M. Bakkers "Paired Twins and 112 Morphology in GaP Nanowires" *Nano Letters* 10, 2349 (2010).

[115] M.D. Stiles and D.R. Hamann "Electron transmission through silicon stacking faults" *Phys. Rev. B* 41 5280 (1990).

[116] J. Wallentin, M. Ek, L.R. Wallenberg, L. Samuelson and M.T. Borgström "Electron Trapping in InP Nanowire FETs with Stacking Faults" *Nano Lett.* 12 151 (2012).

[117] R. Ruppin and R. Englman "Optical Phonons of Small Crystals" *Reports on Progress in Physics* 33 149 (1970)

[118] S. Sahoo, M.S. Hu, C.W. Hsu, C.T. Wu, K.H. Chen, L.C. Chen, A.K. Arora and S. Dhara "Surface optical Raman modes in InN nanostructures " *Appl. Phys. Lett.* 93 233116 (2008).

[119] R. Gupta, Q. Xiong, G.D. Mahan and P.C. Eklund "Surface Optical Phonons in Gallium Phosphide Nanowires" *Nano Lett.* 3 1745 (2003).

[120] D. Spirkoska, G. Abstreiter, and A.F. i Morral, "Size and environment dependence of surface phonon modes of gallium arsenide nanowires as measured by Raman spectroscopy" *Nanotechnology* 19 435704 (2008).

[121] N. Begum, A.S. Bhatti, F. Jabeen, S. Rubini, and F. Martelli "Lineshape analysis of Raman scattering from LO and SO phonons in III-V nanowires" *J. of Appl. Phys.* 106 114317 (2009).

[122] P. Sahoo, S. Dhara, S. Dash, A. Tyagi, B. Raj, C. Das, P. Chandramohan and M. Srinivasan "Surface optical modes in GaN nanowires" *International Journal of Nanotechnology* 7 823-832 (2010).

[123] A. Mllayah, R. Carles and G. Landa "Raman Study of Longitudinal Optical Phonon-Plasmon Coupling and Disorder Effects in Be-doped GaAs" *J. Appl. Phys.* 69 7 4064-4070 (1991).

[124] R. Fukasawa and S. Perkovitz "Raman-scattering spectra of coupled LO-Phonon hole-plasmon modes in p-type GaAs" *Phys. Rev. B* 50 19 (1994).

[125] S. Ernst, A.R. Goñi, K. Syassen, and M. Cardona "LO-phonon-plasmon Modes in n-GaAs and n-InP under pressure" *J. PHys. Chem. Solids* 56 3/4 567-570 (1995).

[126] N.D. Mermin "Linhard Dielectric Function in the Relaxation-Time Approximation" *Phys. Rev. B* 1 5 2362 (1970).

[127] S. Ernst, A.R. Goñi, K. Syassen, and M. Cardona "Plasmon Raman scattering and photoluminescence of heavily doped n-type InP near the Γ-X cross-over" *Phys. Rev. B* 53 3 1287-1293 (1996).

[128] T. Gokus PhD at LMU "Time-Resolved Photoluminescence and Elastic White Light Scattering Studies on individual CArbon Nanotubes"; "Optical Characterization of Oxygen Plasma Treated Graphene" (2011).

[129] R.K. Harrison and A. Ben-Yakar "Role of near-field enhancement in a plasmonic laser nanoablation using gold nanorods on a silicon substrate" *Opt. Expr.* 18 21 22556-22572 (2010).

[130] P. Kühler, E.-M. Roller, R. Schreiber, T. Liedl, T. Lohmüller, and J. Feldmann "Plasmonic DNA-Origami Nanoantennas for Surface-Enhanced Raman Spectroscopy" *Nano Lett.* 14 5 29142919 (2014).

[131] M.K. Schmidt, R. Esteban, A. Gonzalez-Tudela, G. Giedke and J. Aizpurua "QED Description of Raman Scattering from Molecules in Plasmonic Cavities" arXiv:1509.03851v1.

THANKS

In first place, I would like to thank Prof. Hartschuh for having given me the opportunity to spend over four years in his research group, first for my master thesis as Erasmus exchange student and second for the PhD.

I am sincerely grateful to all co-workers and collaborators who accompanied me in the different steps of my experience, first of all to all past and present members of the "AK Hartschuh" who I worked with during my master thesis and PhD.

I would also like to mention Prof. Scheu, Dr. Venkatesan, J. Röhr and Prof. Krogstrup for the great work we made together on the Be-doped GaAs nanowires. Without their support I would have not achieved many of the results I presented in this thesis.

For the same reason I also want to thank Prof. Aizpurua and Dr. Schmidt, who gave me during my visit in San Sebastian a fundamental input for the interpretation of the results on the plasmon assisted non-linear Raman scattering. This input was essential to my work.

I would also like to mention Dr. Piatkowski, who followed the early steps of my research. What I learned from him helped throughout all these years.

I am very much grateful to my colleagues and friends who shared with me the most part of my daily research activity, with all its good an bad. Alberto, for the fruitful discussions about theoretical physics and for the help in the Matlab simulations and programming in general. Harald, Xian, Nico, Richard, for their constant support and motivation. Without them, I would have probably not made it through all the difficulties I met.

This thesis is dedicated to my wife Rachele. When it was dark, she was the light leading me out from the shadow.